# THERMOCHEMICAL NANOLITHOGRAPHY FABRICATION AND ATOMIC FORCE MICROSCOPY CHARACTERIZATION OF FUNCTIONAL NANOSTRUCTURES

A Thesis
Presented to
The Academic Faculty

by

Debin Wang

In Partial Fulfillment
of the Requirements for the Degree
Doctor of Philosophy in the
School of Physics

Georgia Institute of Technology
August 2010

# THERMOCHEMICAL NANOLITHOGRAPHY FABRICATION AND ATOMIC FORCE MICROSCOPY CHARACTERIZATION OF FUNCTIONAL NANOSTRUCTURES

Approved by:

Dr. Elisa Riedo, Advisor
School of Physics

Dr. Seth R. Marder
School of Chemistry and Biochemistry

Dr. Jennifer E. Curtis
School of Physics

Dr. Walter A. de Heer
School of Physics

Dr. Dragomir Davidovic
School of Physics

Date Approved: April 30, 2010

*To my beloved families.*

# ACKNOWLEDGEMENTS

I would like to take this opportunity to express my thankfulness to many people who have made this thesis possible.

First and foremost, I would like to thank my thesis advisor Prof. Elisa Riedo for giving me a wonderful opportunity to conduct this exciting interdisciplinary research. My sincere gratitude goes to Prof. Riedo for her invaluable guidance, sparking inspiration, and perpetual encouragement throughout the entire course of this research. She has been and will continue to be my motivation for being persistent, patient and perfect in my career, and in my life.

I would like to graciously thank my thesis committee Prof. Seth Marder, Prof. Jennifer Curtis, Prof. Walter de Heer, and Prof. Dragomir Davidovic for their precious time and valuable guidance.

I would like to extend my gratitude to all my past and present group members who have turned to be my good friends and role models. Special thanks go to Robert for putting me on track to exploring this fantastic research project. Thanks to Tai-De, Marcel, Soo-Young, Suenne, Douglas, and Deborah for always being helpful.

I am extremely grateful to have many remarkable collaborators. I give my thanks to Prof. Marder and his group: Simon, Will, Anthony, Jonas, and Cristina for their support on polymer synthesis and charaterization. Thanks to Prof. King and his group: Jungchul and Zhenting who have been providing constant support for the thermal cantilevers. I am grateful to Prof. Curtis and her group: Vamsi, Keith, Louis, Jan, and Mauricio who have provided me with tremendous knowledge and experience with bioconjugation and fluorescence microscopy. I would like to thank Prof. de Heer and his group: Claire, Yike, Xiaosong, and Mike for their support

on the graphene oxide project. Thanks go to Dr. Sheehan and his group at Naval Research Laboratory: Zhongqing, Arnaldo, and Mike for their assistance on electrical transport measurement and exchange of ideas about thermochemical nanolithography. I would also like to thank Dr. Ogletree and his group at Lawrence Berkeley National Laboratory: Jim, Adam, and Alex for their assistance with micro-Raman measurement.

In addition, I would like to give my thanks to our staff at Physics department: Kevin, Felicia, Samantha, Judy, Stephen, Diego, Debbie, Vicki, Velera, Scott, and Lori for their assistance in many ways.

My close friends at Georgia Tech have provided immense support throughout my graduate studies, so I am grateful to them as well: Kun, Fan, Jung-Cheng, Ran, Yang, Chen, Yifan, Yamato, Ekapop, Abhinav, Gabriel, Meng, Changshi, Tao, and Honggang.

Finally, I must acknowledge that I am thankful for my families and friends on the other side of the planet without whose unwavering support I would not be where I am today. I would like to express my deepest gratitude to my parents, and my parents-in-law for their continual caring, support and encouragement. Last but not least, I would like to give my sincere thanks to my wife, Ying, for her eternal understanding, love, sacrifice, and, above all, for moving half way around the world just to stay with me.

Thanks to each and every one of you!

# TABLE OF CONTENTS

DEDICATION . . . . . . . . . . v

ACKNOWLEDGEMENTS . . . . . . . . . . vii

LIST OF TABLES . . . . . . . . . . xiii

LIST OF FIGURES . . . . . . . . . . xv

SUMMARY . . . . . . . . . . xxi

I INTRODUCTION . . . . . . . . . . 1

- 1.1 Nanofabrication Overview . . . . . . . . . . 1
  - 1.1.1 Photolithography . . . . . . . . . . 2
  - 1.1.2 Particle beam lithography . . . . . . . . . . 3
  - 1.1.3 Soft lithography . . . . . . . . . . 3
  - 1.1.4 Self assembly . . . . . . . . . . 4
  - 1.1.5 Edge lithography . . . . . . . . . . 4
- 1.2 Scanning Probe Nanolithography Review . . . . . . . . . . 5
  - 1.2.1 Force lithography . . . . . . . . . . 6
  - 1.2.2 Electrochemical lithography . . . . . . . . . . 7
  - 1.2.3 Photochemical nanolithography . . . . . . . . . . 7
  - 1.2.4 Dip-pen nanolithography . . . . . . . . . . 8
- 1.3 Nanolithography with Thermal Cantilevers . . . . . . . . . . 9
  - 1.3.1 Thermal cantilevers for data storage Application . . . . . . 9
  - 1.3.2 Parallel patterning with probe arrays . . . . . . . . . . 10

II MATERIALS AND CHARACTERIZATIONS . . . . . . . . . . 13

- 2.1 Materials . . . . . . . . . . 13
  - 2.1.1 Cinnamate-ester copolymer . . . . . . . . . . 13
  - 2.1.2 Cinnamate-carbamate copolymer . . . . . . . . . . 15
  - 2.1.3 Polyphenylene vinylene precursor polymer . . . . . . . . . . 16
  - 2.1.4 Graphene oxide thin film . . . . . . . . . . 17

2.2 Atomic Force Microscopy Characterization . . . . . . . . . . . . . . 18

2.2.1 AFM operation modes . . . . . . . . . . . . . . . . . . . . 18

2.2.2 Friction Force Microscopy . . . . . . . . . . . . . . . . . . 31

2.2.3 Phase Imaging . . . . . . . . . . . . . . . . . . . . . . . . 34

2.2.4 Electric Force Microscopy . . . . . . . . . . . . . . . . . . 36

2.2.5 Conductive Atomic Force Microscopy . . . . . . . . . . . . 41

2.3 Contact Angle Goniometry . . . . . . . . . . . . . . . . . . . . . . 44

2.4 Raman and Infrared Spectroscopy . . . . . . . . . . . . . . . . . . 46

2.5 Epifluorescence Microscopy . . . . . . . . . . . . . . . . . . . . . . 50

III THERMOCHEMICAL NANOLITHOGRAPHY FUNDAMENTALS . . 53

3.1 Instrumentation . . . . . . . . . . . . . . . . . . . . . . . . . . . . 53

3.2 Cantilever Mechanical Characterization . . . . . . . . . . . . . . . 57

3.3 Heat Transfer Modeling . . . . . . . . . . . . . . . . . . . . . . . . 59

3.3.1 Heater temperature modeling . . . . . . . . . . . . . . . . 59

3.3.2 Local contact temperature modeling . . . . . . . . . . . . . 63

3.3.3 Writing kinetics modeling . . . . . . . . . . . . . . . . . . 68

3.4 Spatial Resolution Modeling . . . . . . . . . . . . . . . . . . . . . . 71

IV RESULTS AND DISCUSSION . . . . . . . . . . . . . . . . . . . . . . 75

4.1 Local Wettability Modification of Polymer Surfaces . . . . . . . . . 75

4.1.1 Motivation . . . . . . . . . . . . . . . . . . . . . . . . . . . 75

4.1.2 Write-read-overwrite capability . . . . . . . . . . . . . . . 75

4.1.3 AFM and FTIR characterizations . . . . . . . . . . . . . . 76

4.2 Multifunctional Nano-Templates for Assembling Nano-Objects . . . 78

4.2.1 Motivation . . . . . . . . . . . . . . . . . . . . . . . . . . . 78

4.2.2 Multifunctional nanopatterns . . . . . . . . . . . . . . . . . 79

4.2.3 Protein Nano-arrays . . . . . . . . . . . . . . . . . . . . . . 84

4.3 Nanopatterning of Organic Semiconductors . . . . . . . . . . . . . 88

4.3.1 Motivation . . . . . . . . . . . . . . . . . . . . . . . . . . . 88

4.3.2 Direct writing of conjugate polymer nanostructures . . . . . 89
4.3.3 Raman and fluorescence characterizations . . . . . . . . . . 89
4.4 Nanoscale Tunable Reduction of Graphene Oxide . . . . . . . . . . 94
4.4.1 Motivation . . . . . . . . . . . . . . . . . . . . . . . . . . 94
4.4.2 Nanoscale reduction of graphene oxide with tunable conductivity . . . . . . . . . . . . . . . . . . . . . . . . . . . 95
4.4.3 CAFM and KPFM characterization . . . . . . . . . . . . . . 96
4.4.4 Microscopic four-probe electrical transport measurements . 97
4.4.5 Microscopic two-probe electrical transport measurements . . 99
V CONCLUSIONS AND PERSPECTIVES . . . . . . . . . . . . . . . . . 107
REFERENCES . . . . . . . . . . . . . . . . . . . . . . . . . . . . . . . 109
VITA . . . . . . . . . . . . . . . . . . . . . . . . . . . . . . . . . . . . 125
LIST OF PUBLICATIONS . . . . . . . . . . . . . . . . . . . . . . . . . 127

# LIST OF TABLES

1.1.1 Comparison of various nanofabrication techniques. . . . . . . . . . . . . 2

# LIST OF FIGURES

1.3.1 Millipede 64 × 64 cantilever array. Left panel: Glass wafer of cantilever array. Each square contains 4096 cantilevers. The inset shows the cantilever structure bonded on the glass wafer. Right panel: SEM micrograph of a section of the 4096 cantilever array [74]. Copyright 2004 IEEE. . . . . . . . . . . . . . . . . . . . . . . . . . . . . . . . 11

2.1.1 TGA analysis of $p(THP\text{-}MA)_{80}p(PMC\text{-}MA)_{20}$. The chemical structure is shown as inset. . . . . . . . . . . . . . . . . . . . . . . . . . . 13

2.1.2 Crosslinking of the cinnamate group under UV irradiation. . . . . . . 14

2.1.3 The cinnamate-carbamate copolymer and its pyrolysis products under heating. . . . . . . . . . . . . . . . . . . . . . . . . . . . . . . . . 15

2.1.4 TGA analysis of cinnamate-carbamate copolymer. . . . . . . . . . . . 16

2.1.5 Thermal conversion of PPV. . . . . . . . . . . . . . . . . . . . . . . 17

2.1.6 Raman spectra comparison of SiC, epitaxial graphene grown on SiC (EG), and oxidized EG (GO). . . . . . . . . . . . . . . . . . . . . . . 18

2.2.1 Scheme of force dection mechanism of an AFM with optical beam deflection design. A four-quadrant position sensitive photo-detector is used to detect the vertical bending and torsion of the cantilever to measure the normal and lateral forces. . . . . . . . . . . . . . . . . . 20

2.2.2 Veeco Multimode AFM scanner piezoelectric scanner tube and X-Y-Z electrical configurations. AC voltages applied to conductive areas of the tube create piezoelectric movement along the three major axes. . 21

2.2.3 Voltages applied to the X- and Y-axes produce a raster scan pattern. 22

2.2.4 Schematic of the Lennard-Jones potential. . . . . . . . . . . . . . . . 24

2.2.5 Scheme of a cantilever oscillating near the surface. The cantilever is driven by a piezoelectric oscillator attached on one end. The instantaneous tip-surface separation $d$, the instantaneous oscillation position of the tip $z$ and the average tip-surface separation $z_c$ are shown. . . . 26

2.2.6 Schematic of how the cantilever oscillation amplitude, phase, and resonance frequency change when tip approaches a surface. . . . . . . 27

2.2.7 Scheme of a damped harmonic oscillator used for modeling the motion of a cantilever/tip. . . . . . . . . . . . . . . . . . . . . . . . . . . . 28

2.2.8 A water meniscus formed between a spherical tip and a flat surface in an ambient condition. . . . . . . . . . . . . . . . . . . . . . . . . . 31

2.2.9 Friction force measurement of p(THP-MA)$_{80}$p(PMC-MA)$_{20}$ polymer surface. . . . . . . . . . . . . . . . . . . . . . . . . . . . . . . 33

2.2.10 AFM topography and friction force microscopy images of a TCNL square pattern (bottom-right corner) made on p(THP-MA)$_{80}$p(PMC-MA)$_{20}$ polymer surface [94]. Scale bars: 500 nm. . . . . . . . . . . . . 34

2.2.11 Schematic diagram of Kelvin Probe physics. (A) Two parallel plates made of materials 1 and 2 with different work functions $\phi_1$ and $\phi_2$, corresponding to the energy difference between the Fermi level $\varepsilon$ and the vacuum level. (B) The two materials are electrically contacted, electrons flow from 2 to 1 until the Fermi levels are aligned, leading to an electric field $E$ between the plates. (C) The electric field is removed by applying an external potential. . . . . . . . . . . . . . . . . . . . . 38

2.2.12 KPFM surface potential measurement of a multilayer epitaxial graphene sample. . . . . . . . . . . . . . . . . . . . . . . . . . . . . . . 39

2.2.13 KPFM and EFM measurement of a Au/Si sample. A 80 nm Au island is sitting on top of a Si wafer. Each AFM image is a 10 $\mu$m × 10 $\mu$m scan. . . . . . . . . . . . . . . . . . . . . . . . . . . . . . . 42

2.3.1 A contact angle forms among liquid, solid and vapor/gas phases in thermodynamic equilibrium. . . . . . . . . . . . . . . . . . . . . . 44

2.3.2 Exemplified static water contact angles of a hydrophobic solid surface and a hydrophilic solid surface. . . . . . . . . . . . . . . . . . . . 45

2.3.3 Static water contact angle (solid squares) and friction force (open circles) measurements of p(THP-MA)$_{80}$p(PMC-MA)$_{20}$ copolymer as a function of heating temperature [94]. . . . . . . . . . . . . . . . . 47

2.4.1 Jablonski energy diagram for infrared absorption, Raman scattering, Rayleigh scattering, and fluorescence. . . . . . . . . . . . . . . . . 48

3.1.1 Veeco MultiMode IV AFM microscope. . . . . . . . . . . . . . . . . 54

3.1.2 SEM micrograph of a TCNL thermal cantilever. The tip sits above the integrated resistive heater (shown as inset). . . . . . . . . . . . . . . 55

3.1.3 Customized printed-circuit-board (PCB) cantilever holder and chip holder for Veeco Multimode AFM microscope head. . . . . . . . . . 56

3.1.4 Schematic of Thermochemical Nanolithography (TCNL) system. . . . 57

3.2.1 Spring constant calibration of TCNL thermal cantilever #26 with reference beam method. . . . . . . . . . . . . . . . . . . . . . . . . . 59

3.3.1 Thermal circuit for heat flow of a heated TCNL thermal cantilever, the tip, and the contact with sample. . . . . . . . . . . . . . . . . . . 60

3.3.2 Variation of the electrical resistance of a TCNL integrated heater as a function of dissipated power. Competition between increased electron scattering and intrinsic carrier generation at elevated temperatures results in a peak resistance of 4.5 kΩ at 550 ℃ where $P_H = 7.9$ mW. . 61

3.3.3 Stokes shift as a function of electrical power dissipated on the thermal cantilever. The linear relationship can be used to fit the peak position dependence of cantilever power even though the quadratic polynomial fits the data better. . . . . . . . . . . . . . . . . . . . . . . . . . . . 63

3.3.4 Labview temperature calibration program. The four windows are used to estimate cantilever heater and tip temperature. Arranged from left to right then top to bottom, they are $R_{can}$ vs $V_0$, $R_{can}$ vs $P_{can}$,$T_H$ vs $P_{can}$, and $T_{int}$ vs $P_{can}$, respectively. . . . . . . . . . . . . . . . . . . . 64

3.3.5 TCNL heating efficiency calibration with PMMA, polycarbonate and polysulfonate [94]. . . . . . . . . . . . . . . . . . . . . . . . . . . 67

3.3.6 Thermal kinetic analysis of carbamate copolymer thermogram. (A) TGA thermogram of carbamate copolymer as well as a fitting curve generated from Eq. 3.3.11. (B) Linear fit of TGA data gives $E_a$ and $A$. (C) Writing speed dependence of remaining weight ratio. (D) Normal loading force dependence of remaining weight ratio. . . . . . . . . . . 70

3.4.1 COMSOL finite element modelling (FEM) of the temperature and amine conversion profile inside a carbamate copolymer. (A) Temperature profile. (B) Carbamate to amine conversion ratio profile. (C) Temperature and conversion ratio profile along lateral direction ($z = 0$). (D) Temperature and conversion ratio profile along vertical direction ($x = 0$) . . . . . . . . . . . . . . . . . . . . . . . . . . . . . . 73

3.4.2 COMSOL FEM simulation of TCNL spatial resolution. Temperature dependence $T_{int}$, writing speed dependence ($v$), and normal loading force dependence ($F_N$) are plotted in (A), (B), and (C) respectively. . 74

4.1.1 Topography and friction images of a p(THP-MA)$_{80}$ p(PMC-MA)$_{20}$ copolymer surface before (I) and after a first (II) and second (III) TCNL modification. Reprinted with permission from [94]. Copyright 2007, American Institute of Physics. . . . . . . . . . . . . . . . . . . . 77

4.1.2 FTIR spectra (left) and static water contact angle vs. friction force measurements (right) of a p(THP-MA)$_{80}$ p(PMC-MA)$_{20}$ copolymer upon heating to selected temperatures. Reprinted with permission from [94]. Copyright 2007, American Institute of Physics. . . . . . . 78

4.2.1 Scheme of multifunctional templates by TCNL.(a) A single nano-object pattern is created through three steps: TCNL, crosslinker incubation and nano-object incubation. (b) A double functionality pattern of thiols (blue triangles) and amines (green disks) is created through two rounds of TCNL and incubation processes. (c) A triple functionality pattern of thiols (blue triangles), biotins (red diamonds), and amines (green disks) is created through three rounds of TCNL and incubation processes [79]. Copyright Wiley-VCH Verlag GmbH & Co. KGaA. Reproduced with permission. . . . . . . . . . . . . . . . . . . . . . . . 81

4.2.2 A flowchart to show how the unmasked amine nanotemplates are selectively and covalently functionalized to create patterns of thiols, maleimides, aldehydes or biotins in distinct areas of the polymer surface [79]. Copyright Wiley-VCH Verlag GmbH & Co. KGaA. Reproduced with permission. . . . . . . . . . . . . . . . . . . . . . . . . . . 82

4.2.3 Single and multi-component micro-patterns. (a) Epifluorescence images of micro triangle patterns of Cy5-streptavidin (red) (crosslinked to amine via NHS-biotin), biotinylated Alexa350-antiCD3 (blue) (crosslinked to NHS-biotinylated amine with streptavidin), and atto488 fibronectin (green) (crosslinked to amine with GA). (b) AFM topography and phase images of a triangular pattern of thiol-terminated DNA single strands crosslinked to amines through PMPI. (c) Epifluorescence images of DACM and Cy5-streptavidin orthogonal functionality patterns on the same surface. Blue DACM was crosslinked to amine-terminated triangles by means of SPDP-DTT thiolation, while red Cy5-streptavidin was crosslinked to amine-terminated diamonds by means of NHS-biotin [79]. Scale bars: (a) 5 $\mu$m, (b) 1 $\mu$m, (c) 10 $\mu$m. Copyright Wiley-VCH Verlag GmbH & Co. KGaA. Reproduced with permission. . . . . . . . . . . . . . . . . . . . . . . . . . . . . 85

4.2.4 500 nm fibronectin nanoarray. Epifluorescence image of a regular array of Atto488 fibronectin patches (a) and cross section profile (b). A linear interpolation (solid line) has been used to interpolate the fluorescence data points (dots) obtained by optical microscopy. Fibronectin was crosslinked to amine groups by means of GA. It should be mentioned that the radius of the features is comparable in size with the resolution of the optical image (~0.61 $\lambda$/NA, where $\lambda$ is the wavelength used and NA is the numerical aperture of the objective), so other techniques should be used to determine the distribution of proteins within each feature [79]. Scale bar: 1 $\mu$m. Copyright Wiley-VCH Verlag GmbH & Co. KGaA. Reproduced with permission. . . . . . . . . . . . . . . . . 87

4.2.5 Fibronectin and streptavidin nanoarrays. AFM topography and phase images of a TCNL nanoarray before and after fibronectin (a) and streptavidin (b) attachment. The topography z-range in (a) is 20 nm [79]. Scale bars: 100 nm. Copyright Wiley-VCH Verlag GmbH & Co. KGaA. Reproduced with permission. . . . . . . . . . . . . . . 88

4.3.1 TCNL nanolithography of PPV nanostructures. (a) Scheme of TCNL nanolithography of PPV nanostructures. (b) Fluorescence and (c) AFM topography images of PPV nanostructures made by TCNL at a range of temperatures, 240 °C-360 °C. A zoom-in view of PPV lines made at 240 °C as outlined in (c) is shown in (d). (e) The average profile of the PPV trench outlined in (d) shows that the width (FWHM) of the line is as narrow as 70 nm. The thickness of this precursor film is 100 nm. Scale bars: (b) and (c): 5 $\mu$m, (d): 2 $\mu$m. Reprinted with permission from [173]. Copyright 2009, American Institute of Physics. 91

4.3.2 Raman spectra of (a) untreated precursor, (b) PPV reference, (c) TCNL PPV pattern, and (d) precursor annealed in ambient condition. Reprinted with permission from [173]. Copyright 2009, American Institute of Physics. . . . . . . . . . . . . . . . . . . . . . . . . . . 92

4.3.3 (a) Raman spectra as a function of the temperature used during TCNL, $T_1 = 240\,^\circ\mathrm{C}$, $T_2 = 280\,^\circ\mathrm{C}$, $T_3 = 320\,^\circ\mathrm{C}$, respectively. (b) Comparison between the Raman spectra obtained from the $\mathrm{PPV}_{TCNL}$ pattern ($I^{Experimental}_{PPV_{TCNL}}$) and the combined Raman spectra obtained from Eq. 4.3.1 ($I^{Model}_{PPV_{TCNL}}$). Note that the continuum background is much lower in the TCNL sample than in the vacuum-annealed sample according to the model. Reprinted with permission from [173]. Copyright 2009, American Institute of Physics. . . . . . . . . . . . . . . . . . . . . 100

4.4.1 Local thermal reduction of a $\mathrm{GO}_{epi}$ film: current and topographical images. (A) 3D CAFM current image (taken with a bias voltage of 2.5 V between tip and substrate) of a zigzag shaped nanowire formed after TCNL was performed on $\mathrm{GO}_{epi}$ at $T_{heater}$ ~1060 °C with a linear speed of 0.2 $\mu$m s$^{-1}$ and a load of 120 nN. (B) Corresponding topography image taken simultaneously with (A). (C) Averaged profiles of current and height of the cross sections that are indicated as dashed lines in (A) and (B). From [193]. Reprinted with permission from AAAS. . . 101

4.4.2 Micro 4-point transport and Kelvin probe force microscopy measurements. Current-voltage curves obtained by micro 4-point transport measurements of TCNL low-temperature reduced graphene oxide (Low $T$, $T_{heater}$ ∼600 °C, TCNL high-temperature reduced graphene oxide (High $T$, $T_{heater}$ ∼1200 °C), and vacuum reduced graphene oxide at 600 °C. The table presents the sheet resistance, $R_{sheet}$, measured by 4-point transport measurements, and the contact potential change ($\triangle\Phi$) between GO$_{epi}$ and each listed sample (EG, rGO$_{epi}$, and TCNL-rGO$_{epi}$, respectively). From [193]. Reprinted with permission from AAAS. . 102

4.4.3 Schematic of microscopic 4-probe electrical transport measurement. From [193]. Reprinted with permission from AAAS. . . . . . . . . . 103

4.4.4 SEM micrograph of 4-point transport measurement of a GO$_{epi}$ film. From [193]. Reprinted with permission from AAAS. . . . . . . . . . 103

4.4.5 SEM micrograph of 4-point transport measurement of a GO$_{epi}$ film. From [193]. Reprinted with permission from AAAS. . . . . . . . . . 104

4.4.6 SEM micrograph of the micro 4-probe experiment with a sketch of the tip scan lines during the TCNL reducing. The four conductive probes (T1-T4) used for the resistance measurements are also shown. From [193]. Reprinted with permission from AAAS. . . . . . . . . . . . . . 104

4.4.7 Micro 2-point electrical transport measurement. (Left) SEM images of the configuration used for 2-point transport measurements when the tips are positioned between 2 rGO$_{epi}$ squares without (top), and with (bottom) TCNL-rGO$_{epi}$ nanoribbon in between. The AFM cross section of the nanoribbon is shown as inset of the bottom SEM image. (Right) $I/V$ curves obtained measuring current between 2 rGO$_{epi}$ squares with no nanoribbon in between (top curve), and between 2 rGO$_{epi}$ squares with a nanoribbon in between (bottom curve). From [193]. Reprinted with permission from AAAS. . . . . . . . . . . . . . 105

# SUMMARY

This thesis presents the development of a novel atomic force microscope (AFM) based nanofabrication technique termed as thermochemical nanolithography (TCNL). TCNL uses a resistively heated AFM cantilever to thermally activate chemical reactions on a surface with nanometer resolution. This technique can be used for fabrication of functional nanostructures that are appealing for various applications in nanofluidics, nanoelectronics, nanophotonics, and biosensing devices.

This thesis research is focused on three main objectives. The first objective is to study the fundamentals of TCNL writing aspects. We have conducted a systematic study of the heat transfer mechanism using finite element analysis modeling, Raman spectroscopy, and local glass transition measurement. In addition, based on thermal kinetics analysis, we have identified several key factors to achieve high resolution fabrication of nanostructures during the TCNL writing process.

The second objective is to demonstrate the use of TCNL on a variety of systems and thermochemical reactions. We show that TCNL can be employed to (1) modify the wettability of a polymer surface at the nanoscale, (2) fabricate nanoscale templates on polymer films for assembling nano-objects, such as proteins and DNA, (3) fabricate conjugated polymer semiconducting nanowires, and (4) reduce graphene oxide with nanometer resolution.

The last objective is to characterize the TCNL nanostructures using AFM based methods, such as friction force microscopy, phase imaging, electric force microscopy, and conductive AFM. We show that they are useful for *in situ* characterization of nanostructures, which is particularly challenging for conventional macroscopic analytical tools, such as Raman spectroscopy, IR spectroscopy, and fluorescence microscopy.

# CHAPTER I

# INTRODUCTION

## *1.1 Nanofabrication Overview*

Nanoscience is the study of phenomena that occur in structures with dimensions below 100 nm [1]. Such structures often have properties different than those observed for bulk materials. For example, quantum dots can exhibit single-electron tunneling [2], and carbon nanotubes can have high electrical conductivity and mechanical strength [3]. These new materials, devices and systems can be rationally designed to exhibit novel, unique and significantly improved physical, chemical and biological properties, phenomena and process because of their size [4].

Nanofabrication is the process of making functional structures with arbitrary patterns having nanoscale dimensions [5, 6, 7]. Nanofabrication has been widely implemented commercially for improving microelectronic devices and information technology, for example, to increase the density of components, to lower their cost, and to increase their performance per device and per integrated circuit [8]. Other areas of applications beyond information processing and storage include optics, cell biology, and biomedicine. [9, 10].

The methods used to produce nanoscale structures and nanostructured materials are commonly categorized as "top-down" approach or "bottom-up" approach [6]. The "bottom-up" approach uses interactions between molecules or colloidal particles to self-assemble discrete nanoscale structures in two- and three-dimensions. The "top-down" approach uses various lithography methods to pattern materials with nanometer resolution. This approach includes serial and parallel techniques for patterning features.

There are two dominant "top-down" techniques: photolithography [11] and particle beam lithography [12]. The limitations of these conventional approaches, such as high capital and operational costs, restricted planar-only fabrication, and incompatibility with biological materials, have motivated the development of unconventional fabrication techniques: soft lithography, self assembly, edge lithography, and scanning probe lithography. A brief comparison of these conventional and unconventional nanofabrication techniques is given in Table 1.1.1.

**Table 1.1.1:** Comparison of various nanofabrication techniques.

| Categories | Minimum Feature Size | Methodology |
|---|---|---|
| Photolithography | 37 nm [8] | parallel replication of arbitrary patterns |
| Particle Beam Lithography | 5 nm [13] | serial writing of arbitrary patterns |
| Soft Lithography | ∼5 nm [6] | parallel replication of arbitrary patterns |
| Self Assembly | 48 nm [14] | parallel assembly of regular, repeating structures |
| Edge Lithography | 8 nm [15] | parallel generation of non-crossing structures |
| Scanning Probe Lithography | <1 nm [16] | serial writing of arbitrary structures |

### 1.1.1 Photolithography

Photons have been used for many years to induce chemical reactions in photographic materials or resist polymers. Photolithography based on this process uses a mask or aperture to localize the photochemistry spatially [11]. The image of the mask is reduced in size and projected onto the resist with the system or the mask is placed in physical contact with the resist. The resist is exposed to ultraviolet light (UV, DUV, or EUV) or X-rays. Photolithography for semiconductor industry can pattern 37 nm wide features with 193 nm wavelength light [8]. Patterning of even smaller features requires further advances such as decreasing the light wavelength and developing new photoresist with altered photo sensitivity as well as new types of optics based on reflection rather than transmission. Furthermore, another significant drawback is the time and cost required to fabricate the photomask which are typically patterned by particle beam lithography. Even though there is an alternative method that can produce simple patterns without using a photomask or most of the expensive projection optics, the projected patterns are restricted to regularly spaced arrays of lines or dots [17].

### 1.1.2 Particle beam lithography

Maskless particle beam lithography is a slow process relative to photolithography. This serial technique can generate high resolution features with arbitrary patterns. There are three main particle beam lithography techniques: (1) scanned laser beam technique with about 250 nm resolution, (2) focused electron beam technique with sub-50 nm resolution, (3) focused ion beam technique with sub-50 nm resolution, and (4) neutral metastable atom technique with 50-70 nm resolution [6]. High resolution photomask for photolithography are typically patterned using laser beam and electron beam tools.There are tradeoffs for high resolution patterning with an electron beam or ion beam. The increase of the spatial resolution needs to decrease the particle beam diameter. This results in an increase of the time necessary to achieve the same imaging dose. An improvement can be found by using highly sensitive photoresist. But photoresist that requires lower dose of electrons or ions usually have lower resolution than photoresist that requires higher dose [12].

### 1.1.3 Soft lithography

Soft lithography is a collective name for a set of lithography techniques: replica molding [18], microcontact printing [19], micromolding in capillaries [20], microtransfer molding [21], nanoimprint lithography [22], and solvent-assisted micromolding [23]. These techniques use a patterned elastomer (usually polydimethylsiloxane (PDMS)) as the mold, stamp, or mask to generate or transfer the pattern. Soft lithography offers advantages over conventional photolithography and particle beam lithography for application where nonplanar substrates or large scale patterning are involved. It is particularly promising for fabrication of simple, single-layer structures for uses in cell culture, microelectromechanical systems (MEMS) and applied optics. However, the fabrication of functional nanostructures by soft lithography requires high resolution masters that typically generated by conventional nanofabrication techniques. In addition, the replication process is limited by the number of processes due to surface fouling. Higher resolution is limited by surface diffusion of printed molecules and distortion of the features within stamp during printing. Recent works demonstrated the resolution of soft lithography has reached sub-100 nm regime [24].

### 1.1.4 Self assembly

Self assembly nanofabrication is a bottom-up approach. It relies on cooperative interactions of small components that assemble spontaneously in a predefined way to produce a larger structure in two or three dimensions. Examples are structures that self assemble from block copolymer [25], molecular and supramolecular chemistry [26], and colloidal particles [27]. When combining the use of conventional photolithography top-down approach, patterns with feature sizes as small as 50 nm have been shown [14]. Self assembly nanofabrication is a stand-alone method, but it is unable to produce structures with precise spatial positioning and arbitrary shapes with a low concentration of defects and functionality that can be achieved using conventional nanofabrication. It is also unable to generate the range of patterns required for simple electronic functionality.

### 1.1.5 Edge lithography

Edge lithography is a nanofabrication method that either transfer patterns directed by the edge of a feature or transform a feature that is thin in the vertical direction into a feature that is thin in the lateral direction. Research interest in this area has increased in the past few years. The first type of edge lithography can be divided into four strategies for generating nanostructures: (1) depositing material at step edges of crystalline lattices [28]; (2) adding or removing material at edge-defined defects in self assembly monolayers (SAMs) [29]; (3) depositing or undercutting at lithographically defined step edges [30]; and (4) patterning photoresist at regions defined by vertical edges in a soft stamp using phase-shifting photolithography [31]. The second type of edge lithography takes advantage of a number of established methods that can grow thin films (thickness between 1 and 50 nm) over large areas. Reported approaches to exposing a nanostructured edge include: (1) fracturing a thin film [32]; (2) sectioning an encapsulated thin film [33]; and (3) reorienting posts capped with a thin film [34]. Edge lithography can be used to pattern arrays of structures less than 100 nm in parallel for a range of materials. However, edge lithography techniques are restricted to generating limited types of line structures in one step of fabrication. Crossed lines can be generated by stacking features [15].

## *1.2 Scanning Probe Nanolithography Review*

Since their invention in 1982 and 1986, scanning tunneling microscopy (STM) [35] and atomic force microscopy (AFM) [36] have proven to be effective techniques capable of identifying the structure and nature of surfaces and adsorbates on substrates down to molecular and atomic resolution. The application of AFM and STM has not only find their applications in inorganic semiconductor substrates, but also in polymer and supramolecular research. Additionally, the techniques have been applied for the determination of interaction forces between proteins and receptors in biochemistry. Soon after the demonstration of ability of STM and AFM to modify substrates, the field of scanning-probe-based lithography (SPL) was developed. A variety of SPL techniques for the modification of substrates have evolved, ranging from the subtle movement of atoms using STM [16], the formation of local deformations in soft substrates using high-contact force AFM [37], to the local application of inks and the local oxidation of suitable substrates [38, 39]. With the application of SPL techniques, control over position and direction in the range of 5 to 50 nm is evident. Moreover, due to the very recently developed multi-probe systems [40] and automated scanning probe equipment [41], the patterning of large areas has become accessible. Not only physical patterns on substrates can be created, but also chemical modification reactions on substrates have been demonstrated, which allow the combination of techniques from both the top-down and the bottom-up approaches. With the increasing costs of conventional photolithography and particle beam lithography techniques, SPL is a particularly useful alternative for low volume manufacturing and prototyping in conventional processes.

### 1.2.1 Force lithography

The aim of conventional AFM surface mapping is to image surfaces without causing surface damage. However, the concept of controlled mechanical deformation of soft substrates or films is useful for fabrication of functional nanostructures. Force lithography (known as nanografting [42] or nanoshaving lithography [43]) is the selective removal of material from a surface by force-induced physical patterning. It has been successfully applied to substrates and films of polymers (such as polycarbonate [44]) and soft metals (such as Cu, Au, Ni, and Ag) [45, 37, 46]. Besides the mechanically induced deformation of substrates and films, scanning probe techniques can also be used for the gentle movement of metallic or latex nanoparticles into dimers, trimers, linear structures. The same approach has also been used for the local removal of parts of SAMs [47] and Langmuir-Blodgett (LB) films [48]. The limiting factor in creating reproducible patterns is the stability of the tip itself, which is prone to deformation and contamination. To prevent excessive deformation, several groups have used diamond or diamond-coated tips [36].

### 1.2.2 Electrochemical lithography

With the use of conductive AFM or STM tips, a type of low-energy tunneling electron beam is able to induce local oxidation of the material which is called field emitting mode. The area below the tip is oxidized by the electric field and material between the tip and substrate (for example, oxygen or water) decomposes and their reaction products oxidize the substrate. Local oxidation can be performed on most conducting substrates, even on thin organic films. The most frequently studied system of the field emission lithography method is the direct oxidation of a hydrogen-terminated Si(100) substrate [49], or metal surfaces (Ti [50], and Ta [49]). SAMs substrates have also been reported for field emission patterning [51]. Patterns of closed packed lines with 35 nm spacing have been demonstrated on photoresist substrates [52]. This electrochemical lithography method provides two advantages over conventional electron beam lithography: (1) it causes less substrate damage because a substantially lower voltage is used for field emission, and (2) it is less costly and easier to operate because it can be operated in ambient condition instead of expensive high vacuum condition.

### 1.2.3 Photochemical nanolithography

Near-field scanning optical microscopy (NSOM) joined the scanning probe microscopy family in 1992 [53]. The scanning probe is an optical fiber that forms into an asperity with a nanoscale aperture (diameter about 50 nm) at its apex. The distance between the tip apex and sample surface is kept within tens of nanometer with a shear-force feedback control system. NSOM can be used for lithography by inducing photochemical reactions on a surface. First attempt with NSOM wrote structures into a Co/Pt multilayer film using visible light (488 nm and 514 nm) [54]. NSOM was then used to expose films of conventional photoresist using UV light from an excimer laser (248 nm). Under optimal conditions, features of 100 nm size was able to fabricated with an uncoated optical fiber [55]. Photochemical oxidation of SAMs of mercaptoundecanoic acid with 244 nm light, followed by selective wet chemical etching of unmasked substrate, can pattern 55 nm wide trenches in gold [56]. Despite the enormous potential this lithography tool is able to offer, NSOM has largely failed to realize its potential due to various reasons. The most significant obstacle is the perception that near-field methods are extremely difficult to operate. The limited light signal is lost from the scattering off the surface and transmission through the optical fiber. It is further limited by the range of the chemistry that is accessible.

### 1.2.4 Dip-pen nanolithography

Dip-pen nanolithography (DPN) is an extremely versatile technique that offers high resolution and registration with direct-write patterning capabilities [57]. DPN functions by facilitating the direct transport of molecules to surfaces, much like the transfer of ink from a macroscopic dip-pen to paper. By depositing several different kinds of molecules on the same substrate, DPN can pattern a range of desired chemistries with spatial control without exposing the substrate to harsh solvents, chemical etching, and/or extreme electrical field gradients. DPN is compatible with a variety of inks, including organic molecules [58], organic [59] and biological [60] polymers, colloidal particles [47], and metal ions [61]. DPN can be used to pattern substrates ranging from metals to insulators and pattern on top functional SAMs adsorbed on a many substrates [62]. The intrinsic linear writing speed of DPN depends on molecular transport between the probe tip and the surface, and is, therefore, limited by mass diffusion. Like all SPL techniques, DPN is inherently a serial lithography process. In order to increase the throughput, DPN has developed several parallel-probe strategies. A linear array of 32 passive (non-actuated) probes has been used to write SAM features with 60 nm resolution [63]. Prototypes of active parallel-probe arrays based on thermoelectric actuation [64] or electrical conduction [65] have been demonstrated to control each individual probe. Still, the ultimate challenge of MEMS integration of DPN technology is the automation of ink delivery. Development of microfludic arrays of addressable ink wells is now underway [66].

## *1.3 Nanolithography with Thermal Cantilevers*

Scanning thermal microscopy has been used to provide heat-related surface local information such as temperature and thermal conductivity [67]. Several types of thermal cantilever with integrated resistive heaters have been developed for this use. The first kind of cantilevers designed for simultaneous topographical and thermal imaging was made from a Wollaston process wire consisting of a Ag sheath and a Pt core [68]. Another type of thermal cantilevers was developed with a thin film Ni/W resistor sandwiched between layers of polyimide [69]. The polyimide cantilever material provided low thermal conductivity for thermal isolation from the ambient medium, low stiffness for imaging soft biological samples, and low electrical conductivity for electrical isolation of the heater from the ambient medium. Finally, resistive heaters had been incorporated into cantilevers with lateral resolution equivalent to state-of-the-art silicon probes [70]. When current flows through the probe, resistive heating near the cantilever tip can raise the cantilever tip temperature to over 1000℃. These silicon thermal cantilevers have also found complimentary efforts in lithography, especially for data storage application.

### 1.3.1 Thermal cantilevers for data storage Application

The data density of magnetic disks will likely plateau in the range of 100-200 Gb in$^{-2}$ due to the super paramagnetic effect [71]. Because of its ability to form and detect nanometer-scale structures, thermomechanical based SPL has been considered a candidate technology for advanced data storage. Thermomechanical nanolithography is a combination of applying a local force by the cantilever/tip to the polymer layer and softening it by local heating. Thermomechanical nanolithography used heat provided by external laser pointed at a conventional AFM cantilever [72] in its initial design. An improved design of cantilevers with integrated doped-silicon heaters was introduced [70]. Results have shown that 40 nm bits can be written with 120 nm pitch without merging, implying a potential bit density of 400 Gb in$^{-2}$ [40]. In addition to its writing capability, the same thermal cantilevers can be used for imaging and reading with a thermomechanical sensing concept. The electrical resistance of the cantilever is temperature dependent. The thermal conductance between the heater platform and the storage substrate changes according to the distance between them. When the heater operates at a relative low temperature and the distance between heater and sample is reduced as the tip moves into a bit indentation, the temperature and resistance of the heater will decrease because the heat transport through air will be more efficient. Thus, changes in resistance of the continuously heated resistor are monitored while the cantilever is scanned over data bits, providing a means of detecting the bits. The sensitivity of thermomechanical sensing is demonstrated better than that of piezoresistive-strain sensing due to the stronger thermal effects in semiconductors.

### 1.3.2 Parallel patterning with probe arrays

The throughput of SPL technologies is limited by their intrinsic serial writing fashion. A practical approach to SPL for large-volume, parallel production may emerge by simultaneously writing patterns with multiple probes. The thermomechanical cantilevers were the first type of cantilever to be fabricated in a two-dimensional array [40]. It was made possible for data storage application through the dual read/write functionality of the heated AFM cantilever. Without the capability of the thermal cantilever for integrated reading, it would require laser beam tracking of every cantilever, optical interferometry of the entire chip, or additional electronics for individual piezoresistors on each cantilever in the array. Arrays of heated AFM cantilevers

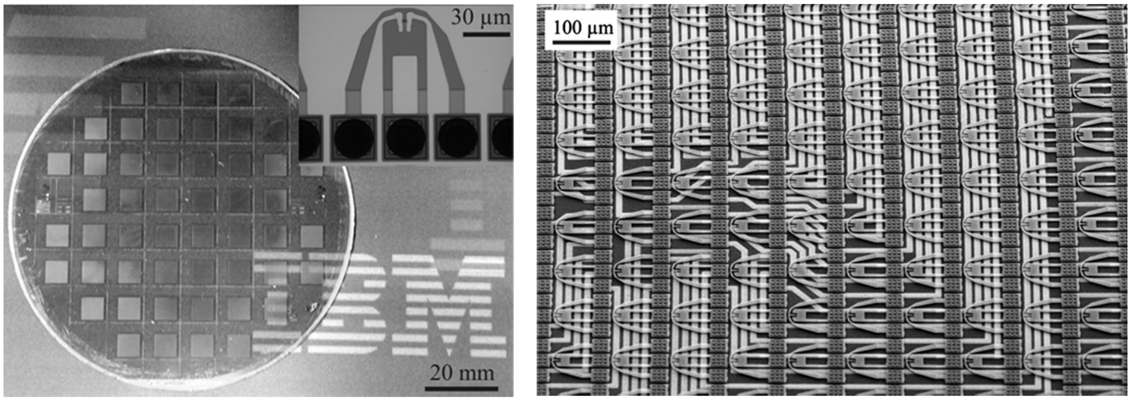

**Figure 1.3.1:** Millipede 64 × 64 cantilever array. Left panel: Glass wafer of cantilever array. Each square contains 4096 cantilevers. The inset shows the cantilever structure bonded on the glass wafer. Right panel: SEM micrograph of a section of the 4096 cantilever array [74]. Copyright 2004 IEEE.

made by IBM's Millipede project started with a 5 × 5 cantilever configuration [73] and expanded to a 32 × 32 cantilever configuration [40]. Most recent design has demonstrated arrays of 64 × 64 free-standing cantilevers as shown in Fig. 1.3.1 [74]. Operation of the cantilever array demonstrated data writing above 840 Gb in$^{-2}$ and a raw bit error rate of $10^{-4}$ [75].

The development of AFM-based data storage using arrays of thermal cantilevers has made an impact on nanoscience and nanotechnology by enabling novel nanoscale thermal transport and temperature measurements, *e.g.* writing thermomechanical indentations using carbon nanotubes affixed to the cantilever tip [76] and studying nanoscale mechanical deformation and wear using highly local heating from the tip [77]. This technology could also have broad impact on the packaging of MEMS systems [74].

# CHAPTER II

# MATERIALS AND CHARACTERIZATIONS

## *2.1 Materials*

### 2.1.1 Cinnamate-ester copolymer

The polymer used in local wettability modification study in Section. 4.1 was poly(tetrahydro-2*H*-pyran-2-yl methacrylate)$_{80}$ poly(3-4-[(E)-3-methoxy-3-oxoprop-1-enyl]phenoxypropyl-2-methacrylate)$_{20}$ copolymer (p(THP-MA)$_{80}$p(PMC-MA)$_{20}$). This copolymer was synthesized and provided by Prof. Marder's group. The details of its synthesis and characterization is described in the literature [78].

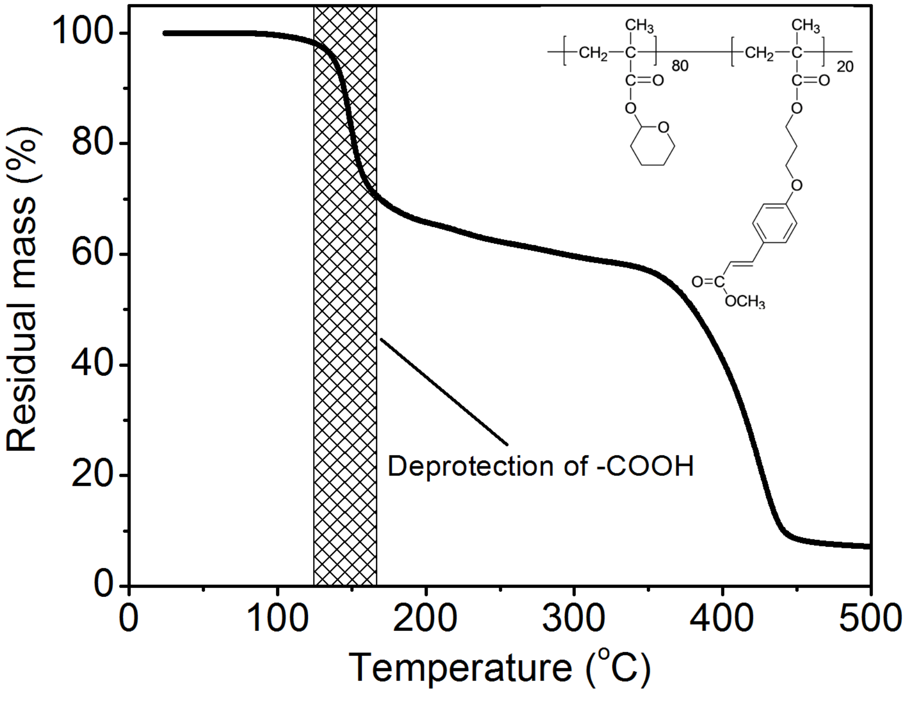

**Figure 2.1.1:** TGA analysis of p(THP-MA)$_{80}$p(PMC-MA)$_{20}$. The chemical structure is shown as inset.

Characterization of p(THP-MA)$_{80}$p(PMC-MA)$_{20}$ copolymer by thermogravimetric analysis (TGA) suggested the removal of tetrahydropyranyl (THP) around 140 °C (the deprotection temperature $T_d$), which was accompanied by a 30% weight loss, as shown in Fig. 2.1.1 (the temperature ramping rate was 5 ℃ min$^{-1}$.). Early test of TCNL on p(THP-MA) polymer film has shown chemical change with significant rippling of the film, as the polymer glass transition temperature, $T_g$(around 120 ℃), was comparable to its $T_d$. Since we were interested in probing the limits of resolution introduced only by chemical change, the cinnamate group was incorporated in order to provide a control of $T_g$ increase of the polymer. Fig. 2.1.2 shows the crosslinking mechanism of the cinnamate group under UV irradiation.

p(THP-MA)$_{80}$p(PMC-MA)$_{20}$ copolymer thin films were prepared by depositing a 5.5 wt % solution of the copolymer in tetrahydrofuran (THF)/cyclohexanone (1:1) on to cleaned glass substrates through a 0.45 $\mu$m polytetrafluoroethylene (PTFE) filter, followed by spin-coating (5 seconds @ 500 rpm followed by 115 seconds @ 1500 rpm). Glass substrates were previously prepared by sonicating 1 inch × 1 inch (1 mm thickness) microscope slides (Fisher Scientific) in acetone for 30 minutes followed by drying in a stream of nitrogen gas. Profilometry measurements revealed the film thickness to be around 500 nm after spin-coating.

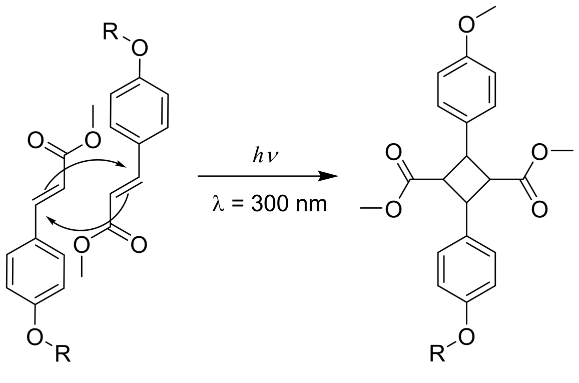

**Figure 2.1.2:** Crosslinking of the cinnamate group under UV irradiation.

### 2.1.2 Cinnamate-carbamate copolymer

Amine functional groups have been used by biologists for many years as a typical protocol to conjugate proteins to a variety of biomolecules and biocompatible surfaces. In order to explore TCNL capabilities of patterning multiple orthogonal biomolecules, we modified previously used p(THP-MA)$_{80}$p(PMC-MA)$_{20}$ copolymer and synthesized cinnamate-carbamate copolymer, poly((tetrahydropyran-2-yl N-(2-methacryloxyethyl)carbamate)-co-(methyl 4-(3-methacryloyloxypropoxy)cinnamate)), as shown in Fig. 2.1.3. This copolymer was synthesized and provided by Prof. Marder group at Georgia Tech. The details of its synthesis and characterization is described in the literature [79]. Films of the polymer were prepared on glass slides pretreated with 4-(3-chlorodimethylsilyl) propoxy benzophenone, by spin-coating from a cyclohexanone solution. The films were then exposed to UV radiation to both covalently bind the film to the substrate through the benzophenone linker (350 nm irradiation) and to crosslink the polymer at the cinnamate moieties (300 nm irradiation). For full details on the preparation and synthesis of these materials, see SI. Films were prepared with thicknesses ranging from 30 nm to 150 nm, but most experiments

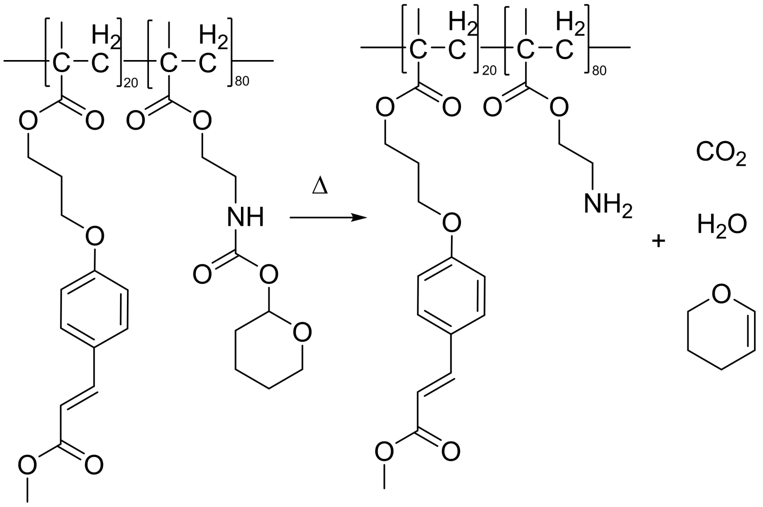

**Figure 2.1.3:** The cinnamate-carbamate copolymer and its pyrolysis products under heating.

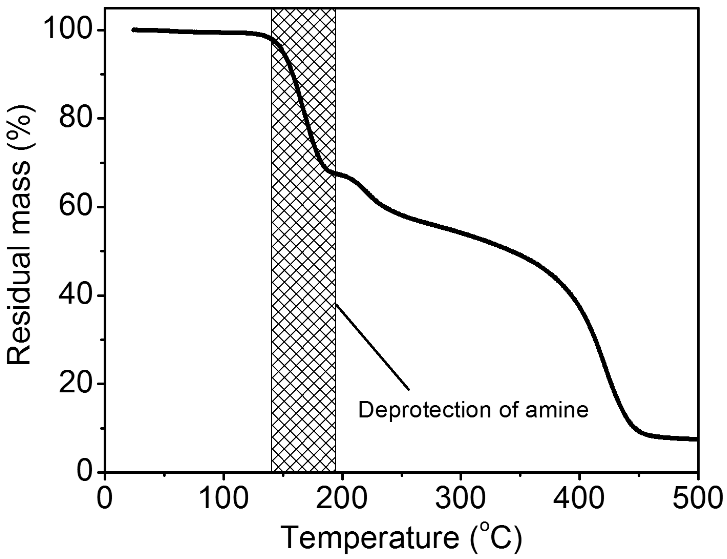

**Figure 2.1.4:** TGA analysis of cinnamate-carbamate copolymer.

were performed on films with a thickness of 75 ± 5 nm, as measured by a stylus profilometer.

The TGA analysis of this polymer, as shown in Fig. 2.1.4, indicated that upon heating the polymer exhibits an initial mass loss around 150 ℃ and a subsequent one starting at about 200 ℃. The overall 30% mass loss after these two steps is consistent with the unmasking of the amine groups in the carbamate side chains. The temperature ramping rate was 5 ℃ per minute.

### 2.1.3 Polyphenylene vinylene precursor polymer

Polyphenylene vinylene (PPV) is a highly conjugated polymer that has been widely used in photovoltaics and organic light emitting diodes as a replacement for inorganic semiconductors [80]. The pi-conjugation that provide such desirable electronic properties makes the PPV polymer highly insoluble. Several methods of soluble polymer precursors have been developed. A common route uses the pyrolysis of a sulfonium salt precursor to produce PPV (Fig. 2.1.5) [81]. As the precursor, poly(*p*-xylene tetrahydrothiophenium chloride), is water soluble large scale of uniform thin film can

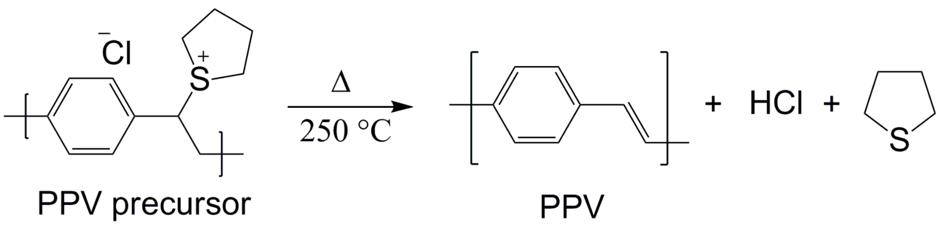

**Figure 2.1.5:** Thermal conversion of PPV.

be deposited on glass or silicon substrates. These films are known to convert to PPV at 250 ℃. [81]

The precursor solution (0.25 wt. % in $H_2O$, Aldrich) was drop-cast on either glass slides or Si(111) wafers that both had been immersed overnight in a piranha solution. These samples were used for TCNL nanopatterning of organic semiconductors as described in Section 2.1.3.

### 2.1.4 Graphene oxide thin film

Graphene oxide (GO) thin film samples were provided by Prof. de Heer's group to investigate TCNL patterning of electrical conducting nanowires for graphene nanoelectronics (see Section 4.4). Following surface flattening by $H_2$ etching at 1450 ℃, epitaxial graphene (EG) was grown on the C-face of 4H-SiC substrates (electrical resistivity $10^5$ - $10^9$ $\Omega$ $cm^{-1}$, CREE) by thermal decomposition at 1500 ℃ in a RF induction furnace under vacuum condition [82]. The samples consist typically 5-20 layers stacked with non graphitic orientational order [83]. The epitaxial graphene films were oxidized directly on chip by Hummer's method [84]. After oxidation the previously conducting grey color EG films (square resistance around 100-200 M$\Omega$) became non-conducting (square resistance $\gg$ 500 M$\Omega$) and yellowish transparent. A complete electrical characterization of GO was reported in Ref. [85] where a Schottky barrier of about 0.5 eV was found.

Raman spectroscopy measurements were carried out to characterize SiC, EG, and GO samples using a confocal Raman system (see Section 2.4). A set of Raman control

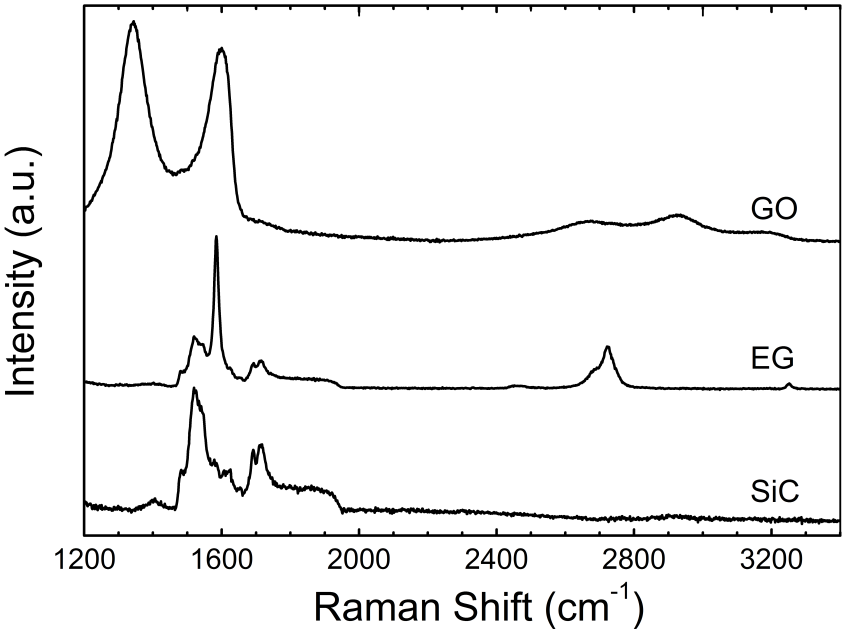

**Figure 2.1.6:** Raman spectra comparison of SiC, epitaxial graphene grown on SiC (EG), and oxidized EG (GO).

spectra is shown in Fig. 2.1.6. The absence of the 2D band around 2700 cm$^{-1}$, the EG signature Raman band, after oxidation indicates that graphene have been oxidized.

## *2.2 Atomic Force Microscopy Characterization*

### 2.2.1 AFM operation modes

The atomic force microscopy is the most popular and powerful tool for measuring forces at the nano-scale since its invention in 1986 [36]. It is a cantilever-based technique for imaging topology and measuring forces. Figure 2.2.1 shows how the AFM detects forces in a commonly used optical beam deflection design.

The tip is located at the end of the cantilever and facing downward to the sample surface. Forces between the tip and the sample surface cause the deformation of the cantilever. The normal force acting on the apex of the tip causes the bending of the cantilever, whereas the lateral force causes the torsion of the cantilever. Most commercial AFMs detect the bending and/or torsion of the cantilever with optical beam-deflection-detection techniques. A laser beam is projected onto the back of the cantilever and reflected to a four-quadrant position sensitive photo-detector (PSPD). The bending of the cantilever makes the position of the laser reflection change vertically (up and down) on the PSPD. The torsion of the cantilever makes the laser deflection change laterally (left and right) on the PSPD. Normal forces are measured by detecting the change of intensity difference between the top and bottom portions of the PSPD ($\Delta[(A+B)-(C+D)]$). Lateral forces are measured by detecting the change of intensity difference between left and right portions ($\Delta[(A+C)-(B+D)]$).

The PSPD itself can measure displacements of light as small as 10 Å. The ratio of the path length between the cantilever and the detector to the length of the cantilever itself produces a mechanical amplification. As a result, the system can detect sub-angstrom vertical movement of the cantilever. A piezoelectric scanner tube is used to move the sample in X-, Y- and Z-direction by applying voltages to deform the tube as shown in Fig. 2.2.2. AFMs rely on raster scanning to probe an area of the sample surface. Raster scanning is performed with piezoelectric scanner whose motion can be incremented in small steps and with high precision. Raster scanning makes it possible to record the tip-sample interaction point-by-point. For each location with X,Y coordinate, the interaction is recorded as one data point. The collection of these data points is then synthesized into the AFM image, a 3-dimensional map. In other words, the area of the sample surface under study is probed not all at once, but in a time series of measurements that are put together point-by-point, and line-by-line as shown in Fig. 2.2.3. The tip moves (relatively to the sample surface) rapidly along fast scan direction with a trace-retrace round trip scan. In the meantime, it moves incrementally along a perpendicular slow scan direction. This is why the AFM is called a scanning probe microscope. In this sense, AFMs are identical to scanning electron microscopes (SEM), except that instead of an electron beam, AFMs use mechanical probes to interact with the sample surface and to investigate

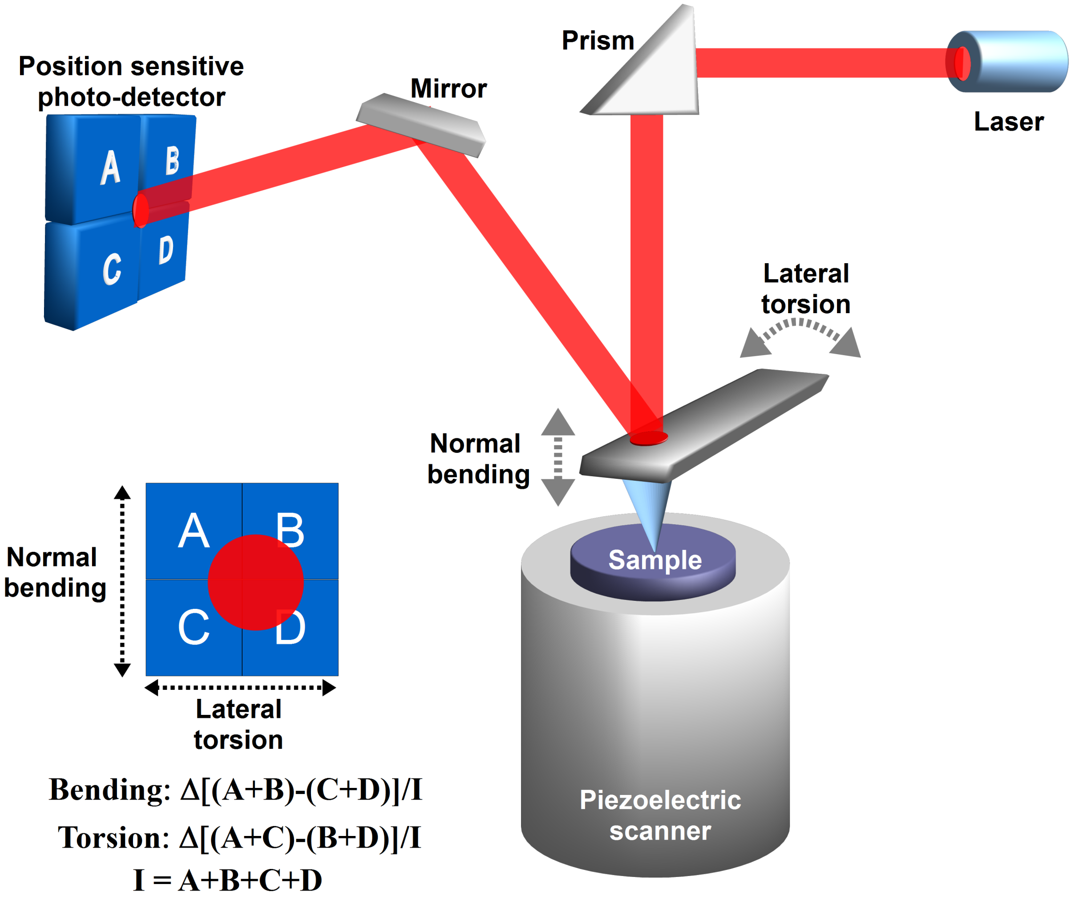
Prism
Laser
Position sensitive photo-detector
Mirror
A
B
C
D
Lateral torsion
Normal bending
Sample
Piezoelectric scanner
Normal bending
A
B
C
D
Lateral torsion
Bending: Δ[(A+B)-(C+D)]/I
Torsion: Δ[(A+C)-(B+D)]/I
I = A+B+C+D

**Figure 2.2.1:** Scheme of force dection mechanism of an AFM with optical beam deflection design. A four-quadrant position sensitive photo-detector is used to detect the vertical bending and torsion of the cantilever to measure the normal and lateral forces.

its properties. The underlying principle of AFM is that the interactions between

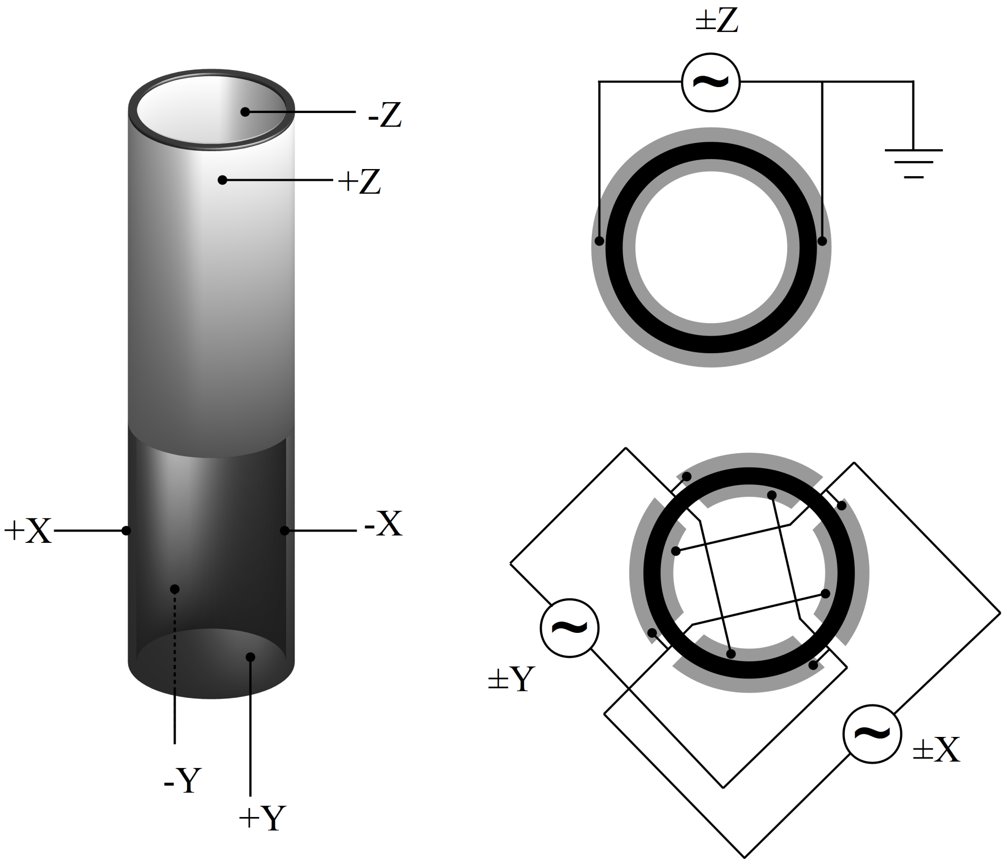

**Figure 2.2.2:** Veeco Multimode AFM scanner piezoelectric scanner tube and X-Y-Z electrical configurations. AC voltages applied to conductive areas of the tube create piezoelectric movement along the three major axes.

the end of a probe tip and the surface results in a response in the cantilever, *i.e.* the deflection of the cantilever. There are several operation modes based on atomic forces. One can measure the deflection of the cantilever associated with such forces. Keeping the deflection constant by varying the vertical position of the tip produces a constant force image. When the tip is sufficiently close to the surface that the repulsive hard wall interaction dominates, the contact mode image represent the topographic structure of the surface. An alternative measurement uses the vibrational characteristics of the cantilever. When the tip oscillates close to the surface, the mid-range to long-range forces cause the damping of the cantilever oscillation. This can results in reduced amplitude, resonance frequency shift, and phase shift of the cantilever oscillation. AFM dynamic imaging mode (tapping mode and non-contact mode) utilize those changes to produce images that contain topographic, magnetic and electrical information of the surface.

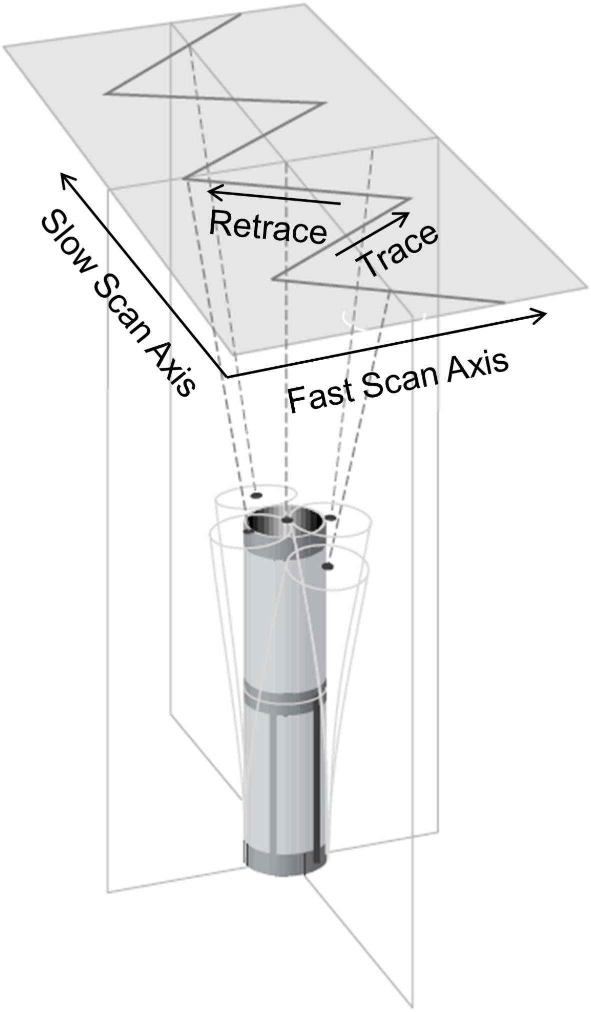

**Figure 2.2.3:** Voltages applied to the X- and Y-axes produce a raster scan pattern.

### *2.2.1.1 Contact Mode*

In the contact mode, also known as the repulsive mode, an AFM tip makes soft physical contact with a sample surface. The tip is attached to the end of a cantilever with a low spring constant, lower than the effective spring constant holding the atoms of the sample together. As the scanner gently traces the tip across the sample (or the sample under the tip), the contact force causes the cantilever to bend to accommodate changes in topography. A feedback loop maintains a constant bending/force of the cantilever by adjusting the height of the sample to compensate for topographical features [86].

When the tip is brought within 10 nm above the sample surface, the resulting interacting forces can be represented by the Lennard-Jones intermolecular potential [87]:

$$V(d) = \frac{\alpha}{d^{12}} - \frac{C}{d^{6}}, \tag{1}$$

where d is the distance between molecules and $\alpha$ and $C$ are constants. The behavior of the Lennard-Jones potential is shown in Fig. 2.2.4. The first term is the repulsive electrostatic interaction due to the electron orbital overlapping. The second term is the van der Waals energy. As the atoms are gradually brought together, they first weakly attract to each other (van der Waals force). This attraction increases until the atoms are so close together that their electron clouds begin to overlap with each other electrostatically. This Pauli repulsion (alternatively called Born repulsion) progressively weakens the attractive force as the interatomic separation continues to decrease. The force goes to zero when the distance between the atoms reaches a couple of angstroms, about the length of a chemical bond. As shown in Fig 2.2.4, the repulsive interaction increases rapidly in the contact regime. As a result, the repulsive force balances almost any force that attempts to push the atoms closer together. In the contact mode AFM operation, when the cantilever pushes the tip against the sample, it will result in the bending of cantilever rather than the movement of the atoms of the tip towards the atoms of the sample surface. Even by applying larger forces with a stiffer cantilever, the interatomic separation between the tip and sample atoms is unlikely to decrease much. Instead, it is more likely for the sample surface to deform which results in nanoindentation.

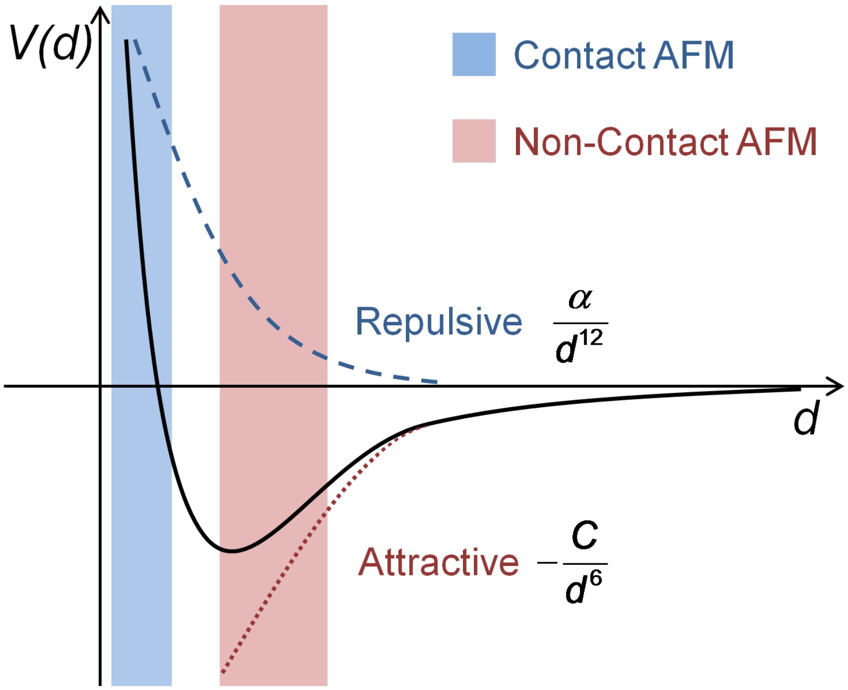

**Figure 2.2.4:** Schematic of the Lennard-Jones potential.

In addition to the repulsive force described above, two other forces are generally present during the contact mode AFM operation in an ambient condition: a capillary force exerted by the thin water layer often present in an ambient environment, and the force exerted by the cantilever itself. The capillary force arises when water wicks its way around the tip, applying a strong attractive force (about 10 nN) that holds the tip in contact with the surface. The magnitude of the capillary force depends upon the tip-to-sample separation.

The force exerted by a cantilever can be treated as the force of a compressed spring. The spring constant of a cantilever, $k$, is determined by its geometry dimensions and material properties. For a common cantilever with a rectangular cross section, $k$ is given by [88]:

$$k = \frac{Ewt^3}{4L^3}, \tag{2.2.2}$$

where $E$ is the Young modulus of the cantilever material, $w$ is the cantilever width, $t$ the thickness, and $l$ the length. In the contact mode, the tip-surface force exerted by the short range repulsive and/or attractive interactions ($F_{ts}$) is balanced by the force exerted by the bending of the cantilever ($F_c$) that relates to the tip movement in vertical direction $z$ by Hook's law:

$$F_{ts} = -F_c = kz. \tag{2.2.3}$$

The magnitude and sign (repulsive or attractive) of the cantilever force depends upon the deflection of the cantilever and upon its spring constant.

#### *2.2.1.2 Tapping Mode*

Tapping mode imaging is a key advance in atomic force microscopy (AFM) on soft, adhesive, or fragile samples. This technique allows high resolution topographic imaging of soft matter sample surfaces that are easily damaged, loosely held to their substrate, or otherwise difficult to image by other AFM techniques. Specifically, Tapping Mode overcomes problems associated with friction, adhesion, and other difficulties that can plague conventional AFM scanning methods [89].

Tapping Mode imaging is implemented by oscillating the cantilever at or near its resonance frequency using a piezoelectric oscillator attached to one end of the cantilever as shown in Fig.2.2.5. When the tip is far from surface, the cantilever is excited at its natural frequency. When the oscillating tip moves toward the surface, it begins to tap the surface: the vertically oscillating tip alternately contacts the surface and lifts off. As the oscillating cantilever begins to intermittently contact the surface, the cantilever oscillation is necessarily damped due to energy loss caused by the interaction between the tip and the surface. The approaching of the tip towards the surface will modify the resonance frequency which in turns implies a modification of the oscillation amplitude. The actual amplitude will be given by the value of the new resonance curve at the excitation frequency of the oscillator. As a result, the new oscillation amplitude would be smaller than the free amplitude (Fig. 2.2.6).

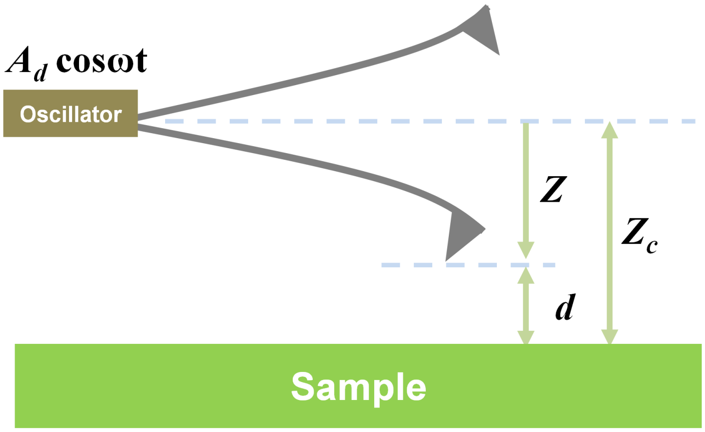

**Figure 2.2.5:** Scheme of a cantilever oscillating near the surface. The cantilever is driven by a piezoelectric oscillator attached on one end. The instantaneous tip-surface separation $d$, the instantaneous oscillation position of the tip $z$ and the average tip-surface separation $z_c$ are shown.

A thorough understanding of dynamic AFM operation requires to solve the equation of motion of the cantilever-tip ensemble under the influence of tip-surface forces. A complete rigorous approach is a formidable task that involves the solution of the equation of motion of a three dimensional vibrating cantilever. On the other hand, it has been shown that the cantilever-tip system can be described as a damped harmonic oscillator as shown in Fig. 2.2.7. The equation of motion can be written as:

$$m\ddot{z} = F_{ts} + F_0 \cos(\omega t) - kz - \gamma \dot{z}, \tag{2.2.4}$$

where $m$ is the effective mass, $F_0$ and $\omega$ are the amplitude and angular frequency of the driving force, respectively; $\gamma$ is the damping coefficient of the internal friction of the cantilever determined by its resonance frequency $\omega_0$, and quality factor $Q$:

$$\gamma = \frac{m\omega_0}{Q}. \tag{2.2.5}$$

The resonance frequency of a cantilever, $\omega_0$, is determined by its geometry dimensions and material properties. For a cantilever with a rectangular cross section, the natural

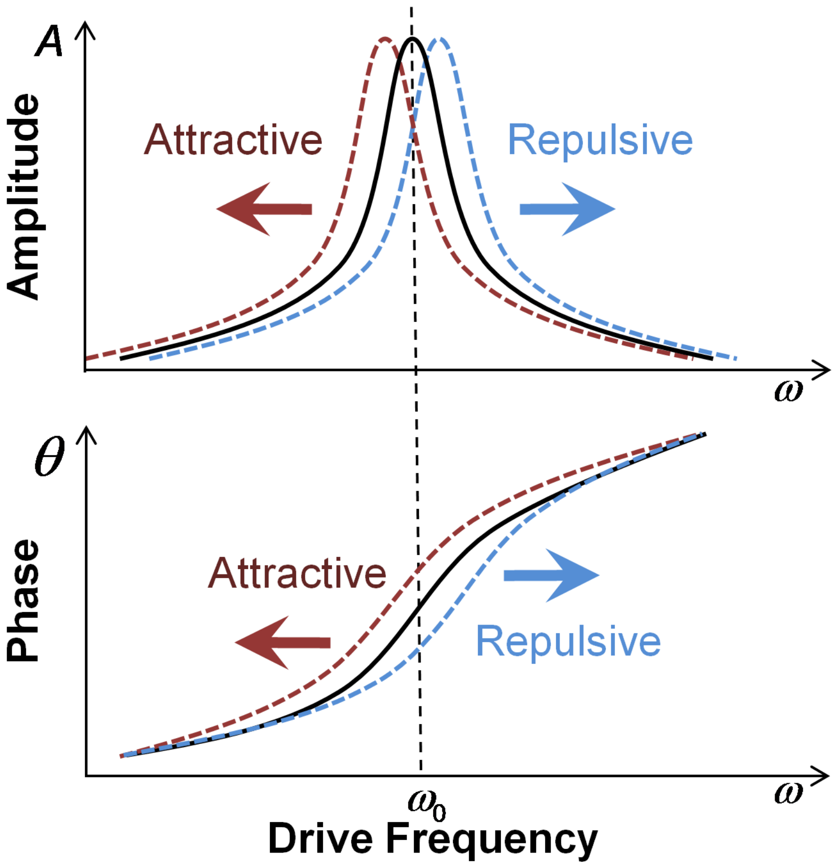

**Figure 2.2.6:** Schematic of how the cantilever oscillation amplitude, phase, and resonance frequency change when tip approaches a surface.

frequency (free resonance frequency) is given by:

$$\omega_0 = \sqrt{\frac{k}{m_{eff}}} = \sqrt{\frac{Ewt^3}{4ml^3}}, \tag{2.2.6}$$

where $E$ is the Young modulus of the cantilever material, $w$ is the cantilever width, $t$ the thickness, $l$ the length, and $m_{eff}$ is the effective mass $0.24m$. Typical value for dynamic mode AFM cantilevers range between 50 kHz to 500 kHz.

In the absence of tip-surface forces $F_{ts} = 0$, Eq. 2.2.4 is the quation of a forced harmonic oscillator with damping. The solution can be found as:

$$z = B\exp\left(-\frac{\omega_0 t}{2Q}\right)\cos(\omega_r t + \beta) + A\cos(\omega t - \theta). \tag{2.2.7}$$

The solution contains a transient term and a steady term. After a time constant $2Q/\omega_0$, the motion is dominated by the steady term. The steady term is a harmonic

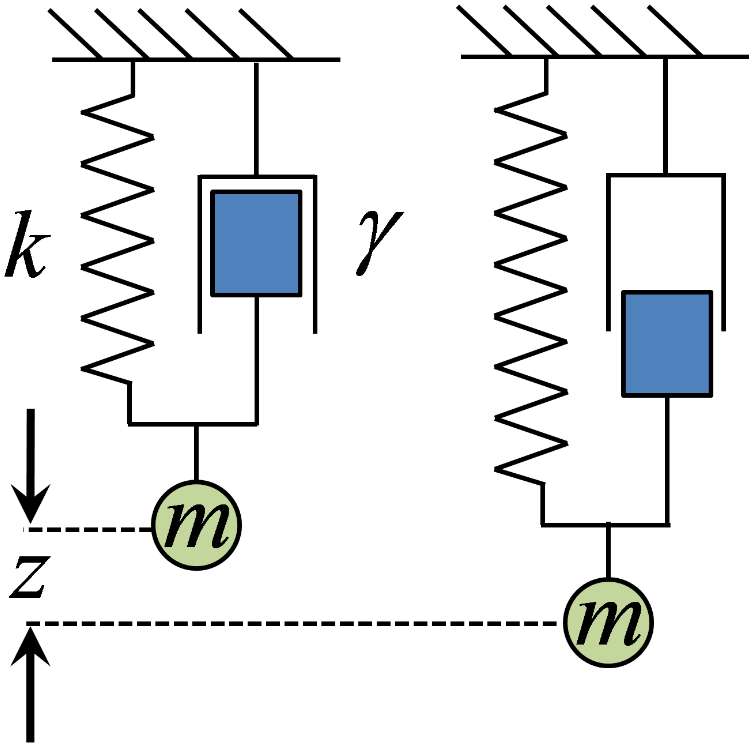

**Figure 2.2.7:** Scheme of a damped harmonic oscillator used for modeling the motion of a cantilever/tip.

function with a phase shift with respect to the excitation source. The dependence of amplitude with the excitation frequency ($\omega$) can be calculated by the Lorentzian expression:

$$A = \frac{A_d \omega_0^2}{\sqrt{(\omega_0^2 - \omega^2)^2 + (\omega\omega_0/Q)}}, \tag{2.2.8}$$

where $A_d$ is driving amplitude of the piezoelectric oscillator. The phase shift is calculated as:

$$\theta = \arctan \frac{\omega\omega_0}{Q(\omega_0^2 - \omega^2)}. \tag{2.2.9}$$

When operated at its resonance frequency ($\omega = \omega_0$), the resonance amplitude is:

$$A_0 = \frac{A_d \omega_0}{\sqrt{Q}}. \tag{2.2.10}$$

It is important to note that the damping modifies the resonance frequency of the cantilever ($\omega_r$) from its natural frequency ($\omega_0$) as the following:

$$\omega_r = \omega_0 \sqrt{\left(1 - \frac{1}{2Q^2}\right)}. \tag{2.2.11}$$

Assuming the tip is under the influence of a parabolic tip-surface interaction potential, the total force acting on the tip should include the interaction force $F_{ts}$. For small displacements with respect to the equilibrium position, the effective spring constant can be expressed as:

$$k_e = k - \frac{\partial F_{ts}}{\partial z}, \tag{2.2.12}$$

then the effective resonance frequency is calculated by:

$$\omega_e = \sqrt{\frac{k - \frac{\partial F_{ts}}{\partial z}}{m}} \approx \omega_0 \left(1 - \frac{1}{2k}\frac{\partial F_{ts}}{\partial z}\right). \tag{2.2.13}$$

This shows that the resonance frequency of a weakly perturbed harmonic oscillator depends on the gradient of the interaction force. A change in the effective resonance frequency implies a whole shift of the resonance curve according to the Eq. 2.2.8 where $\omega_0$ is replaced by $\omega_e$. The changes in amplitude and phase as shown in Fig. 2.2.6 can be calculated as:

$$\Delta A = \frac{2QA_0\frac{\partial F}{\partial z}}{3\sqrt{3}\left(k - \frac{\partial F}{\partial z}\right)}, \tag{2.2.14}$$

$$\Delta\theta = \frac{Q}{k}\frac{\partial F}{\partial z}. \tag{2.2.15}$$

During the tapping mode operation, the oscillation amplitude of the tip is measured by the detector and sent to the controller electronics. The cantilever oscillation amplitude is maintained constant by adjusting the tip-sample separation with the feedback loop. The movement of the piezoelectric scanner and the phase shift of the cantilever oscillation are recorded to identify the topographic features and measure surface properties of interst.

#### *2.2.1.3 Non-Contact Mode*

Non-Contact AFM is one of several vibrating cantilever techniques in which an AFM cantilever oscillates near the surface and rasters across it [89]. The spacing between the tip and the sample is of the order of tens to hundreds of angstroms. This spacing range is the same as the van der Waals interaction in Fig. 2.2.4 as the Non-Contact regime.

During each oscillation cycle in the non-contact mode, the tip experiences a mixture of short-range interactions and long-range interactions. Example of long-range interactions include electrostatic interaction, current-induced or static-magnetic interactions. These interactions are smaller than the van der Waals interactions and usually contribute little to the signal. When the tip is far from the surface, the van der Waals interactions decay rapidly to the point of negligible. In this regime, long-range interactions are still significant. The difference in decay length provides a means to distinguish the two types of interactions.

In order to maintain tip-surface spacing at long-range interaction regime, non-contact mode is usually achieved with two-pass scan. In the first-pass scan, AFM operates in contact mode or tapping mode and the topography information is recorded

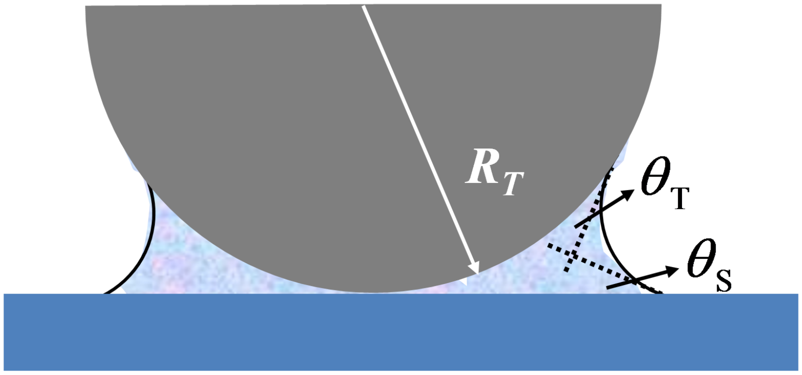

**Figure 2.2.8:** A water meniscus formed between a spherical tip and a flat surface in an ambient condition.

in the computer. In the second-pass scan, the tip lifts up and scan the same area with a constant height above the sample surface. Hence, it is also called lift mode or constant height mode.

### 2.2.2 Friction Force Microscopy

Friction force microscopy (FFM) is an AFM technique that provides local material contrast at nanometer scale [45]. When operated in the contact mode, the friction between the tip and the sample produces a lateral force on the moving tip, which results in the torsion the cantilever. Under ambient conditions, FFM is able to provide material contrast related to its wetting properties.

When the tip slides across the surface, water capillary bridges (meniscus) are formed between the tip and the surface as shown in Fig. 2.2.8. For an ideally smooth spherical tip of radius $R_T$ and a flat surface, the capillary force can be expressed as [90]:

$$F_C = 2\pi R_T \gamma(\cos\theta_T + \cos\theta_S), \tag{2.2.16}$$

where $\gamma$ is the liquid tension and $\theta_T$ and $\theta_S$ are static contact angle of the tip and flat surface, respectively. The capillary force due to these liquid meniscus makes a significant contribution to the total friction force of the tip. The friction between two macroscopic bodies is composed of contributions from a multitude of small microcontacts and is independent of contact area. On the contrary, for the contact between an infinite flat surface and an AFM tip, the single asperity model is valid and the friction is proportional to the contact area. According Hertzian contact theory, the contact radius between the tip (radius of curvature $R$) and the surface is determined by [91]:

$$a = \left( \frac{3}{4} \frac{F_N R}{E^*} \right)^{\frac{1}{3}}, \tag{2.2.17}$$

where $F_N$ is the normal loading force applied to the tip, and $E^*$ is the effective Young modulus of the system that can be expressed by:

$$\frac{1}{E^*} = \frac{(1-\nu_1^2)}{E_1} + \frac{(1-\nu_2^2)}{E_2}, \tag{2.2.18}$$

where $E_1$, $\nu_1$, $E_2$, and $\nu_2$ are the Young modulus and the Poisson ratio of the tip material and the surface material, respectively. As a result, the friction force $F_F$ increases as $F_N^{2/3}$. Under an ambient condition, we must take into account the adhesion force $F_A$ that is mainly composed of van der Waals forces and capillary force [92]. Therefore, $F_F$ can be expressed as:

$$F_F = \mu \left( F_N + F_A \right)^{\frac{2}{3}}, \tag{2.2.19}$$

where $\mu$ is the friction coefficient. An example can be found in a FFM measurement performed on a smooth p(THP-MA)$_{80}$p(PMC-MA)$_{20}$ polymer thin film surface as shown in Fig. 2.2.9. The fitted curve shows a very good 2/3 power dependence of the total applied force $F_N + F_A$, indicating the validity of the single asperity contact model. In addition, FFM acts as an surface chemical mapping technique to distinguish materials with different wettability properties [93]. In the contact mode, the tip raster scan over the surface with a constant normal force $F_N$. According to Eq. 2.2.19, hydrophilic surface tends to produce larger friction force than hydrophobic surface because of its larger capillary interaction with the tip. In this way, the computer

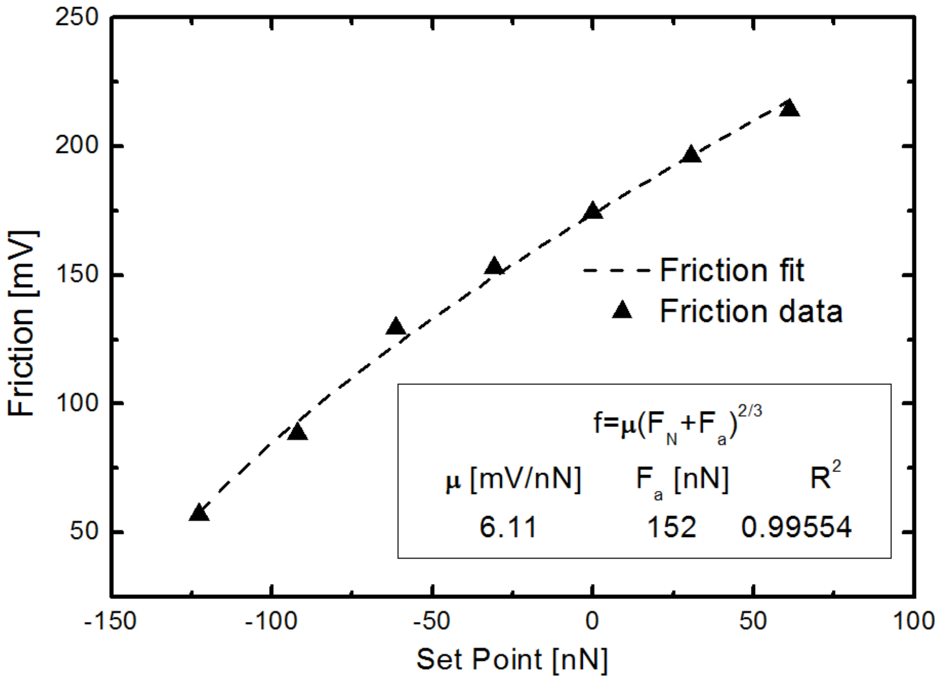

**Figure 2.2.9:** Friction force measurement of p(THP-MA)$_{80}$p(PMC-MA)$_{20}$ polymer surface.

can generate friction mapping images showing visible contrast between hydrophilic (bright, high values) and hydrophobic (dark, low values) areas. Figure 2.2.10 shows a FFM measurement of p(THP-MA)$_{80}$p(PMC-MA)$_{20}$ polymer surface. A TCNL square pattern was made on the bottom-right corner of the image. The topography image shows unnoticeable change. However, the friction image shows a drastic contrast in the patterned area. This is because the hydrophobic surface became hydrophilic after THP protection groups were removed during the thermochemical patterning process. In this thesis research, FFM was exploited to identify TCNL patterns right after the nanolithography process. The TCNL patterns always showed up in FFM with distinct contrast with the untreated area in the background due to the change of wettability. The TCNL probes ($k \approx 0.5$ N $m^{-1}$) and Nanosensors PPP-CONT contact mode probes ($k \approx 0.2$ N $m^{-1}$) were used to acquire FFM contrast images.

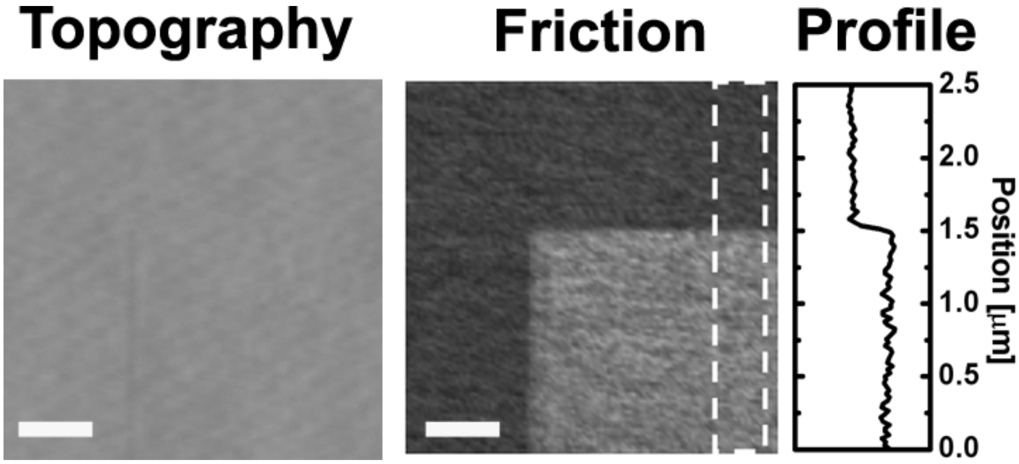

**Figure 2.2.10:** AFM topography and friction force microscopy images of a TCNL square pattern (bottom-right corner) made on p(THP-MA)$_{80}$p(PMC-MA)$_{20}$ polymer surface [94]. Scale bars: 500 nm.

### 2.2.3 Phase Imaging

Phase Imaging is a derivative mode of dynamic mode AFM (tapping mode and non-contact mode). The phase of the cantilever oscillations $\theta$, measured relative to the drive signal of the piezoelectric crystal, has turned out to be a powerful signal for studying the properties of the sample surface, especially heterogeneous surfaces [89]. Phase Imaging has become especially useful for soft matter research (such as polymers, proteins, and DNA) [95], and for electrical and magnetic property investigations as in electrostatic force microscopy and magnetic force microscopy.

As shown in Eq. 2.2.9, the phase shift relative to the oscillator drive oscillation depends on the the medium (quality factor, $Q$) and relationship between the excitation and resonance frequencies of the oscillator. It is reasonable to relate the phase shift to the surface properties. During the phase imaging operation, the phase shift is recorded while feedback electronics keeps the amplitude at a constant set point. A considerable research has been devoted to the potential of phase imaging for detecting variations in material properties, such as adhesion, elasticity and viscoelasticity [96].

A handful of theoretical descriptions have been attempted to interpret the phase images. The goal is to find an expression to relate a given material property with its corresponding phase shift. Magonov *et al.* assumed a harmonic approximation to relate phase shifts and sample stiffness [97]. They argued that the effect of tip-surface interaction on the tip motion could be accounted by introducing an effective force constant $k_{eff} = k + \sigma$, where $\sigma = \Sigma(\partial F_i/\partial z)$ is the deivative of the forces acting on the tip. They propose to calculate the phase shift by:

$$\theta = \arctan \frac{m\omega\omega_0}{Q\left(k + \sigma - m\omega^2\right)}. \tag{2.2.20}$$

If $\sigma \ll k$, the above expression gives the phase at $\omega = \omega_0$:

$$\theta_0 = \arctan\left(\frac{k}{Q\sigma}\right) \approx \frac{\pi}{2} - \frac{Q}{\sigma k} = \frac{\pi}{2} - \epsilon a E^* \frac{Q}{k}, \tag{2.2.21}$$

where $\sigma$ has been approximated by the surface stiffness $s = \epsilon a E^*$ defined by the tip-surface contact radius $a$, and the effective elastic Young modulus $E^*$ as expressed by Eq. 2.2.18. Therefore, phase imaging provides a mapping of stiffness variation on the sample surface. In general, a stiffer region has a larger phase shift and hence appears brighter in a phase image. However, the contrast can be reversed under large driving amplitude $A_d$ and small set point. Under such setting, the tip taps very harshly on the surface that it leads to a large contact radius $a$ on soft material region and hence large phase signal. It is important to examine how the phase shifts depend on the parameters ($A_d$ and set points) and establish a range of the parameters for which the surface stiffness is dominated by Young modulus.

Phase Images often compliment topography images by mapping the various regions of the sample surface each of which interact with the tip differently from others. This difference is sometimes so subtle that it is barely noticeable in the topography images, but clearly visible in the contrast variations in the phase images. However, topographic features convolve into the phase Image, and must be recognized apart from the contrast in the phase image that is primarily a result of material inhomogeneity.

Phase imaging is exploited in this thesis research as a characterization tool to provide high resolution images of biomolecules such as proteins and DNA (Section 4.2). Nanosensors SSS-NCHR tapping mode AFM probes were used. They are designed with super sharp tips with very small radius of curvature (typically 2 nm) and very high aspect ratio (4:1 at 200 nm from tip apex). They are able to produce much higher spatial resolution images with less tip-convolution effect than other generic tapping mode probes or contact mode tips.

### 2.2.4 Electric Force Microscopy

Scanning tunneling microscopy (STM) and scanning tunneling spectroscopy (STS) techniques are very powerful methodologies which possess a chemical sensitivity and can achieve a subnanometer resolution. However, their application is restricted to the first few atomic layers of electrically conducting films. Therefore, this limits their application to the study of working electronic devices that are made up of thick conductive layers with alternating highly insulating areas. Alternatively, a number of new AFM techniques using electrically conducting probes have been developed. They can measure primary physical properties such as current flows, resistance, capacitance, electrostatic forces, charge distribution, surface potential. These new AFM techniques, *i.e.* Conductivity AFM (CAFM) [98], Electrostatic Force microscopy (EFM) [99], and Kelvin Probe Force Microscopy (KPFM) [100], hold great promises for electronic characterization of materials since they allow simultaneous high resolution acquisition of topographic images along with electrical and electronic characterization. In this section, we focus on EFM and KPFM techniques. CAFM will be discussed in Section 2.2.5.

KPFM measurement is suited for the study of soft samples such as organic materials since it does not require a direct physical contact between the conductive tip and the sample. In addition, its high voltage resolution of a few millivolts, allows the study of surface potential distributions of a variety of thin films, including poorly conductive materials [99].

The Kelvin probe technique is named after William Thomson, known as Lord Kelvin, who introduced it in 1898 to explain the formation of built-in contact potential differences in metals. In a metal, the work function $\varphi$, is defined as the difference in energy between an electron in the vacuum state and an electron at the Fermi energy of the metal, hence,the minimal energy needed to remove an electron from the electronic ground state. For semiconductors and insulators, it can be regarded as the difference in energy between the vacuum level and the most loosely bound electron inside the solid.

When two plates of a capacitor composed of different materials are electrically wired together (Fig. 2.2.11), electrons will flow from the material with the lower work function to the higher one, generating opposite charges on the capacitor plates and contact potential difference (CPD, $\Delta\varphi = \varphi_1 - \varphi_2$) between these two materials. The presence of an electric field in the capacitor due to these charges can be found. An external potential $V_{dc}$ can be applied to nullify this field. At equilibrium, the field is zero, and $V_{dc}$ equals CPD. Therefore, the work function of the material understudy can be determined as $\varphi_2 = \varphi_1 - qV_{dc}$, where $q$ is the electron charge. KPFM was developed by Wickramasinghe and co-workers a few years after the invention of AFM [100]. In this setup, the reference capacitor plate is a sharp conductive AFM tip attached to a cantilever. The tip-sample interaction is highly localized and the potential differences between the tip and the sample can be detected by measuring the deflection of the cantilever due to the electrostatic interactions, allowing measurement of $\varphi$ with high spatial and electrical resolutions.

KPFM records the electrostatic force interaction between the tip and the sample. In order to derive an expression for the electrostatic force $F$ between the tip and the sample, we assume a parallel-plate capacitor geometry as shown in Fig. 2.2.11. The

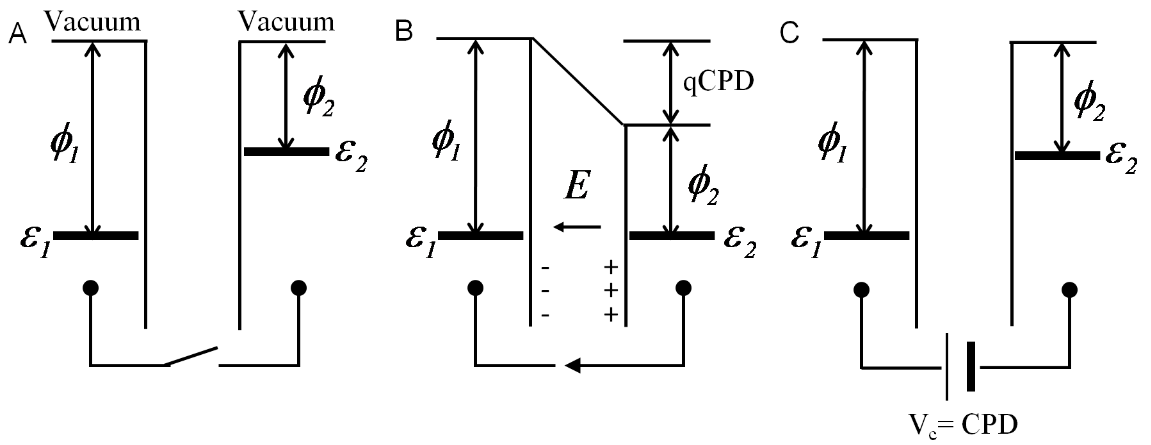
A
Vacuum
Vacuum
$\phi_1$
$\phi_2$
$\varepsilon_1$
$\varepsilon_2$
B
qCPD
$\phi_1$
$\phi_2$
E
$\varepsilon_1$
$\varepsilon_2$
- - -
+ + +
C
$\phi_1$
$\phi_2$
$\varepsilon_1$
$\varepsilon_2$
V$_c$= CPD

**Figure 2.2.11:** Schematic diagram of Kelvin Probe physics. (A) Two parallel plates made of materials 1 and 2 with different work functions $\phi_1$ and $\phi_2$, corresponding to the energy difference between the Fermi level $\varepsilon$ and the vacuum level. (B) The two materials are electrically contacted, electrons flow from 2 to 1 until the Fermi levels are aligned, leading to an electric field $E$ between the plates. (C) The electric field is removed by applying an external potential.

energy $U$ in a parallel plate capacitor can be expressed as:

$$U = \frac{1}{2}C(\Delta V)^2, \tag{2.2.22}$$

where $C$ and $\Delta V$ are the local capacitance and the voltage difference between the tip and the sample, respectively. When applied with a tip voltage containing both a DC ($V_{dc}$) and an AC ($V_{ac}\sin(\omega t)$) components, $\Delta V$ can be expressed as:

$$\Delta V = \frac{\Delta\phi}{q} - V_{dc} + V_{ac}\sin(\omega t), \tag{2.2.23}$$

where $\Delta\phi$ is the difference in contact potential. The force is then the rate of change of the energy with tip-sample separation distance, $z$:

$$F = -\frac{\partial U}{\partial z} = -\frac{1}{2}\frac{\partial C}{\partial z}\Delta V^2 = F_{dc} + F_\omega + F_{2\omega}, \tag{2.2.24}$$

where the static component is:

$$F_{dc} = -\frac{1}{2}\frac{\partial C}{\partial z}\left[\left(\frac{\Delta\phi}{q} - V_{dc}\right)^2 + V_{ac}^2\right], \tag{2.2.25}$$

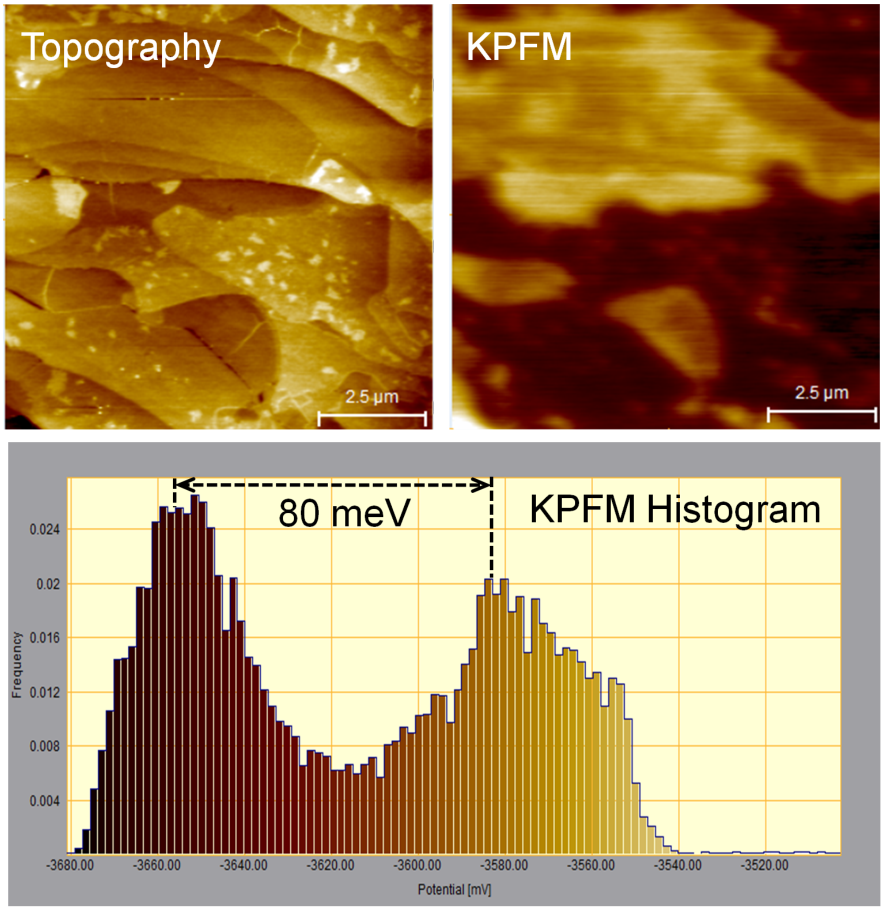

**Figure 2.2.12:** KPFM surface potential measurement of a multilayer epitaxial graphene sample.

and the dynamic components at frequencies $\omega$ and $2\omega$ are:

$$F_\omega = -\frac{\partial C}{\partial z}\left[\left(\frac{\Delta\phi}{q} - V_{dc}\right) V_{ac}\sin(\omega t)\right], \tag{2.2.26}$$

$$F_{2\omega} = \frac{1}{4}\frac{\partial C}{\partial z}\left[V_{ac}^2\cos(2\omega t)\right]. \tag{2.2.27}$$

The AFM servo controller contains a lock-in amplifier that tracks the $\omega$ component of the electrostatic force and a feedback loop that adjusts the DC voltage. The goal is to minimize $F_\omega$ until $\Delta\varphi = qV_{dc}$ and find the work function of the sample $\varphi_2 = \varphi_1 - qV_{dc}$.

In the Veeco Multimode IV AFM system, KPFM is carried out with a two-pass lift mode (non-contact) procedure. The surface topography is obtained by generic tapping mode in the first pass and the surface potential is measured on the second pass. On the first pass (main scan), the cantilever is mechanically vibrated near its resonance frequency by a small piezoelectric oscillator as described in Section 2.2.1.2. On the second pass (interleave scan), the tip ascends to a constant lift scan height; the oscillator used for tapping mode is turned off and an oscillating voltage $V_{dc}+V_{ac}\sin(\omega t)$ is applied directly to the probe tip. If there is a non-zero DC voltage bias between the tip and sample, *i.e.* $V_{dc} \neq \frac{\Delta\phi}{q}$, the oscillating force on the cantilever at frequency $F_\omega$ causes the cantilever to vibrate at frequency $\omega$, and the amplitude can be detected. Therefore, local CPD is determined by adjusting $V_{dc}$ until the first harmonic oscillation is nullified. $V_{dc}$ is recorded by the computer to construct a CPD map of the surface. Figure 2.2.12 shows a KPFM measurement of a multilayer epitaxial graphene sample. A couple of layers of graphene was grown on a 4H SiC substrate as described in Section 2.1.4. The surface morphology mapping as shown in topography image was not able to distinguish the number of graphene layers as they grew inwards. However, KPFM channel showed very clear contrast of different graphene layers. Surface potential difference between each layer is measured to be 80 meV.

EFM is an alternative option to measure the electrostatic interaction between the tip and the sample. As discussed in Section 2.2.1.2, the phase shift in tapping mode imaging can be used to describe the force gradient variation. EFM phase imaging is able to capture the variation of the electrostatic force gradient induced by electrical potential difference and sample surface charge or dipole. As with KPFM, EFM operates in a two-pass scan procedure. However, on the second pass scan when tip is separated 50 - 100 nm above the surface, the cantilever is still driven by the piezoelectric oscillator near its resonance frequency. Instead of a varying DC bias voltage controlled by the feedback loop, a fixed DC bias is applied to the tip or the sample. For a parallel plate capacitor, the force gradient $\partial F/\partial z$ can be expressed by:

$$\frac{\partial F}{\partial z} = -\frac{1}{2}\frac{\partial^2 C}{\partial z^2}(\Delta V)^2, \tag{2.2.28}$$

where the potential difference $\Delta V$ is given by Eq. 2.2.23. According to Eq. 2.2.15, the phase shift in EFM can be directly related to the potential difference by:

$$\Delta\theta = -\frac{Q}{2k}\frac{\partial^2 C}{\partial z^2}(\Delta V)^2. \tag{2.2.29}$$

This means that the phase shift are squared functions of the potential difference $\Delta V$ between the tip and the sample, and that the resolution of the technique is determined by the lateral variations of the gradient $\partial^2 C/\partial z^2$. The shift is always negative, because $\partial^2 C/\partial z^2$ is always positive. Figure 2.2.13 shows a KPFM and EFM measurement of a routine calibration sample. A 80 nm high Au island was deposited on a Si wafer. KPFM is able to distinguish the surface potential difference between the Au and Si (about 250 meV). The EFM phase image was able to produce electrostatic force gradient map when the sample substrate was biased with 3 V. In this thesis research, EFM and KPFM were implemented to characterize TCNL reduced graphene oxide nanopatterns. They were able to distinguish the surface potential contrast between treated and untreated graphene oxide regions at nanometer scale. Nanoworld SCM-PIT probes were selected for EFM and KPFM operation. The force constant ($k$ = 2.8 N·m$^{-1}$ and resonance frequency $f$ = 75 kHz) and the special Pt/Ir5 coating of probes are optimized for the electrostatic force application. The typical tip radius of curvature is less than 25 nm.

### 2.2.5 Conductive Atomic Force Microscopy

Conductive Atomic Force Microscopy (CAFM) is a secondary imaging mode derived from the contact mode AFM that characterizes conductivity variations across medium- to low-conducting and semiconducting materials [98]. CAFM employs conductive probe tips (*i.e.* doped Si tips, or Pt coated Si tips) and has a current sensing

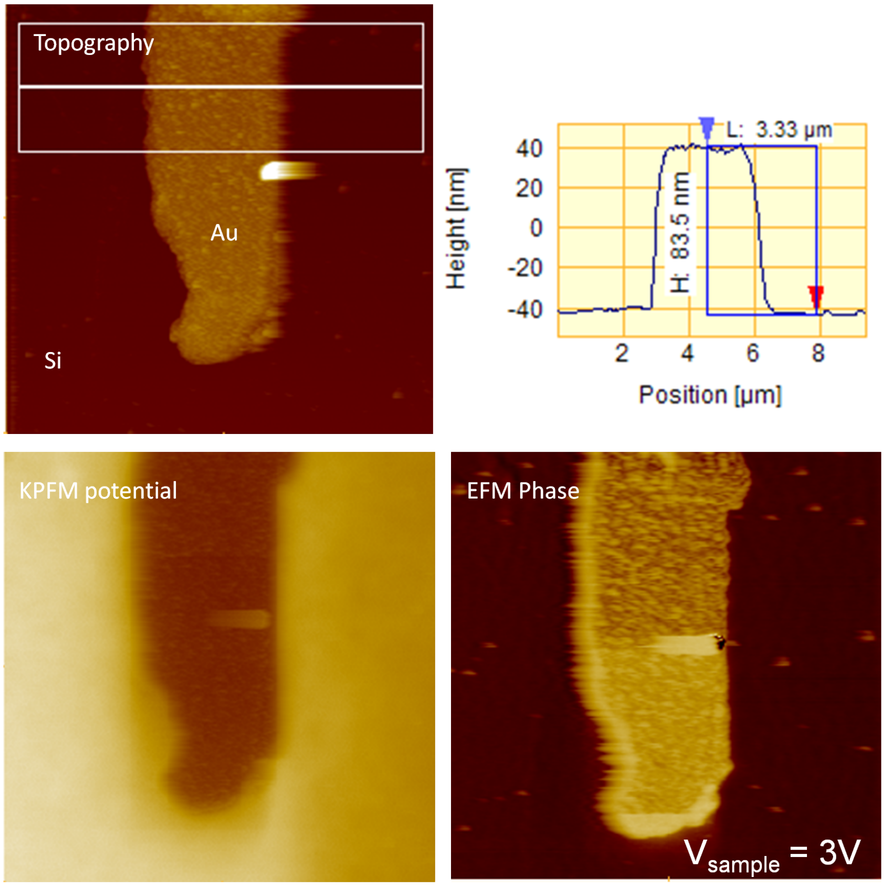

**Figure 2.2.13:** KPFM and EFM measurement of a Au/Si sample. A 80 nm Au island is sitting on top of a Si wafer. Each AFM image is a 10 $\mu$m × 10 $\mu$m scan.

range of 1 pA to 1 $\mu$A. The CAFM application module can be operated in either imaging or spectroscopy mode. In the imaging mode, images of the electrical current are obtained, while in the spectroscopy mode one can collect current-voltage $(I-V)$ or current-force $(I-F)$ spectra. In the imaging mode, an conductive probe is scanned over the sample surface in the contact mode as a feedback loop keeps the deflection of the cantilever constant while the local height of the sample is measured. During the scan, a DC bias is applied between the tip and the sample. A low-noise linear current amplifier senses the resulting current passing through the sample as the topography image is simultaneously obtained. The observed current can be used as a measure for the local conductivity or electrical integrity of the sample. In spectroscopy mode, the imaging scan is stopped and the tip is held in a fixed location while the sample bias is sweeping.

CAFM is commonly used to determine dielectric thin film thickness in the order of 1-100 nm. In the early stage of CAFM development, it is widely used for monitoring the thickness variation of $SiO_2$ dielectric films that can be used as gate oxides in field emission transistors or used as tunneling oxides for memory capacitors. The dielectric film thickness can be obtained by fitting CAFM $I-V$ spectroscopy data with field emission Fowler-Nordheim tunneling (FNT) model or direct tunneling (DT) model in the following form [101]:

$$I = A_{eff}\frac{q^2}{8\pi h\phi}\frac{m_0}{m_{eff}}\frac{\beta^2V^2}{d^2}\exp\left\{-\frac{8\pi\sqrt{2m_{eff}q}}{3h}\frac{d}{\beta V}\phi^{\frac{3}{2}}\left[1-\left(1-\frac{qV}{\phi}\right)^{\frac{3}{2}}\right]\right\}, \quad (2.2.30)$$

where $q$ is the electron charge, $h$ is the Plank's constant, $m_0$ is electron mass, $m_{eff}$ is the effective electron mass in the conduction band of the dielectric material, $d$ is the dielectric film thickness, $V$ is the applied DC bias between CAFM tip and sample, and $\phi$ is the energy barrier between the emission electrode, the conductive tip, and dielectric material. $A_{eff}$ is effective emission area, *i.e.* the tip-surface contact area that can be calculated according to Eq. 2.2.17:

$$A_{eff} = \pi a^2 = \pi\left(\frac{3FR}{4E^*}\right)^{\frac{2}{3}}. \quad (2.2.31)$$

Eq. 2.2.30 holds for the DT regime ($V < \phi/q$) and for the FNT regime ($V > \phi/q$) provided the correction factor, in square brackets, is maintained at unity [102].

CAFM is exploited in this thesis research to characterize TCNL reduced graphene oxide nanostructures. TCNL nanostructures shows distinct CAFM current contrast due to its change of conductivity upon thermal reduction. Nanoworld SCM-PIC probes were selected for CAFM operation. The force constant ($k = 0.2Nm^{-1}$ and the special Pt/Ir5 coating of probes are optimized for electrostatic force application. The typical tip radius of curvature is less than 25 nm.

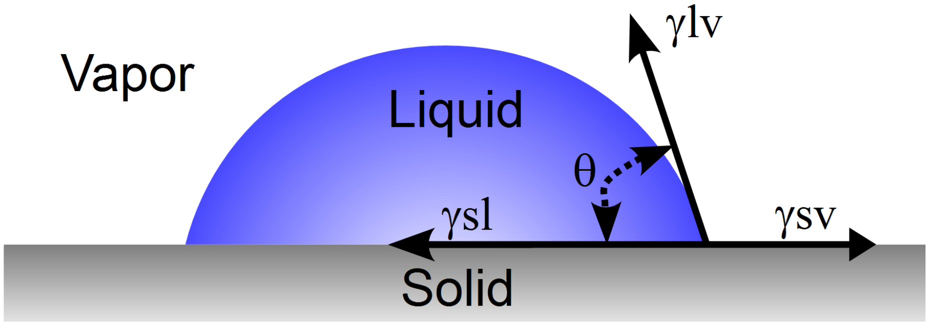

**Figure 2.3.1:** A contact angle forms among liquid, solid and vapor/gas phases in thermodynamic equilibrium.

## *2.3 Contact Angle Goniometry*

Contact angle goniometry measurement is typically used for evaluation of wettability and adhesiveness between solid and liquid surfaces. By producing a droplet of pure liquid on a solid surface, an angle is formed between the solid-liquid interface and liquid-vapor interface. This is referred to as a contact angle ($\theta$) as shown in Fig. 2.3.1.

The theoretical description of contact arises from the consideration of a thermodynamic equilibrium between the three phases: the liquid phase of the droplet ($L$), the solid phase of the substrate ($S$), and the gas/vapor phase of the ambient ($V$) (which will be a mixture of ambient atmosphere and an equilibrium concentration of the liquid vapor). At equilibrium, the chemical potential in the three phases should be equal. Here we denote the solid-vapor interfacial energy as $\gamma_{SV}$, the solid-liquid interfacial energy as $\gamma_{SL}$ and the liquid-vapor energy as simply $\gamma_{LV}$. The relationship among the above three surface energies (surface tensions) at equilibrium is formulated by Young's equation [103]:

$$\gamma_{SV} = \gamma_{SL} + \gamma_{LV} \cos \theta. \tag{2.3.1}$$

Note that if the commonly used assumption of negligible liquid vapor adsorption is applied, then Eq. 2.3.1 may be written in terms of $\gamma_S$ and $\gamma_L$ instead of $\gamma_{SV}$ and $\gamma_{LV}$.

For the four quantities in Young's equation, $\gamma_{LV}$ and $\theta$ are readily measurable.

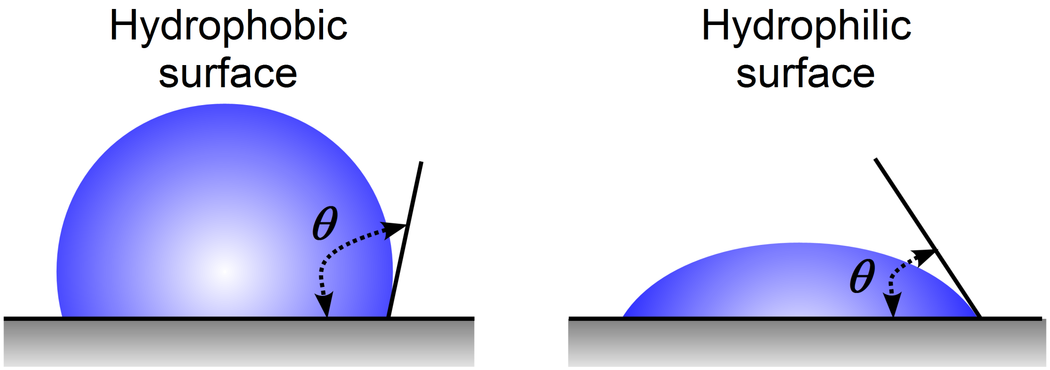

**Figure 2.3.2:** Exemplified static water contact angles of a hydrophobic solid surface and a hydrophilic solid surface.

In order to determine the solid surface energy $\gamma_{SV}$, further information between the quantities is needed. An equation of state for solid-liquid interfacial energy has been developed by Rayleigh and Good as the following [104]:

$$\gamma_{SL} = \gamma_S + \gamma_L - 2\Phi(\gamma_S \gamma_L)^{\frac{1}{2}}, \tag{2.3.2}$$

where the Good interaction parameter $\Phi$ is given by:

$$\Phi = e^{-\beta(\gamma_L - \gamma_S)^2}, \tag{2.3.3}$$

and the constant $\beta$ can be empirically determined. By combining Eq. 2.3.1 and Eq. 2.3.2, the surface energy of the solid $\gamma_S$ can be obtained from:

$$\cos\theta = -1 + 2\sqrt{\frac{\gamma_S}{\gamma_L}} e^{-\beta(\gamma_L - \gamma_S)^2}. \tag{2.3.4}$$

For liquids with relatively small surface energies, $\Phi \approx 1$, and solid surface energy can be simplified as:

$$\gamma_S = \frac{1}{4}\gamma_L(1 + \cos\theta)^2. \tag{2.3.5}$$

The static contact angle is an index of the wettability of a solid surface. In studies of surface hydrophilicity, a low water contact angle (typically $< 90°$) indicate the surface is hydrophilic and has high surface energy. In contrast, a high water contact angle (typically $> 90°$) indicates the surface is hydrophobic and has low surface energy (Fig. 2.3.2).

In this thesis research, water contact angle goniometry was utilized to characterize the surface hydrophilicity changes due to the thermochemical reactions of the ester copolymer and carbamate copolymer. Polymer samples were bulk heated at selected temperatures by a hot plate (Corning, PC-200) and were then taken to contact angle goniometer (SEO, Phoenix 150) for static water contact angle measurements. Figure 2.3.3 shows a series of temperature dependence water contact angle measurements of an ester copolymer sample (data shown in solid squares symbols). The contact angle increased to 80° from 55° at 130 ℃ because of the deprotection of carboxylic acid. This rendered the surface hydrophilic. At 180 ℃, carboxylic acid underwent a pyrolysis reaction and anhydride was formed. The surface became hydrophobic again and water contact angle dropped back to around 60°. This hydrophilicity evolution was confirmed by AFM friction force microscopy measurement (data shown in open circle symbols) where high friction corresponded to hydrophilic surface and low contact angle, and low friction corresponded to hydrophobic surface and high contact angle.

## *2.4 Raman and Infrared Spectroscopy*

Raman spectroscopy and infrared (IR) spectroscopy are two important analytical and research tools for chemical identification and molecular structure characterization. IR spectroscopy allows one to characterize molecules by measuring the absorption of incident infrared light of energies associated with certain vibration modes [105]. Raman spectroscopy arises from a different process. When monochromatic radiation is incident upon a sample it will interact with sample and may be reflected, absorbed, or transmitted. While the majority of the scattering radiation undergoes elastic collisions (Rayleigh scattering), a small fraction (about 1 in $10^7$) experiences inelastic collisions with polarized molecules and may radiate photons associated with a series

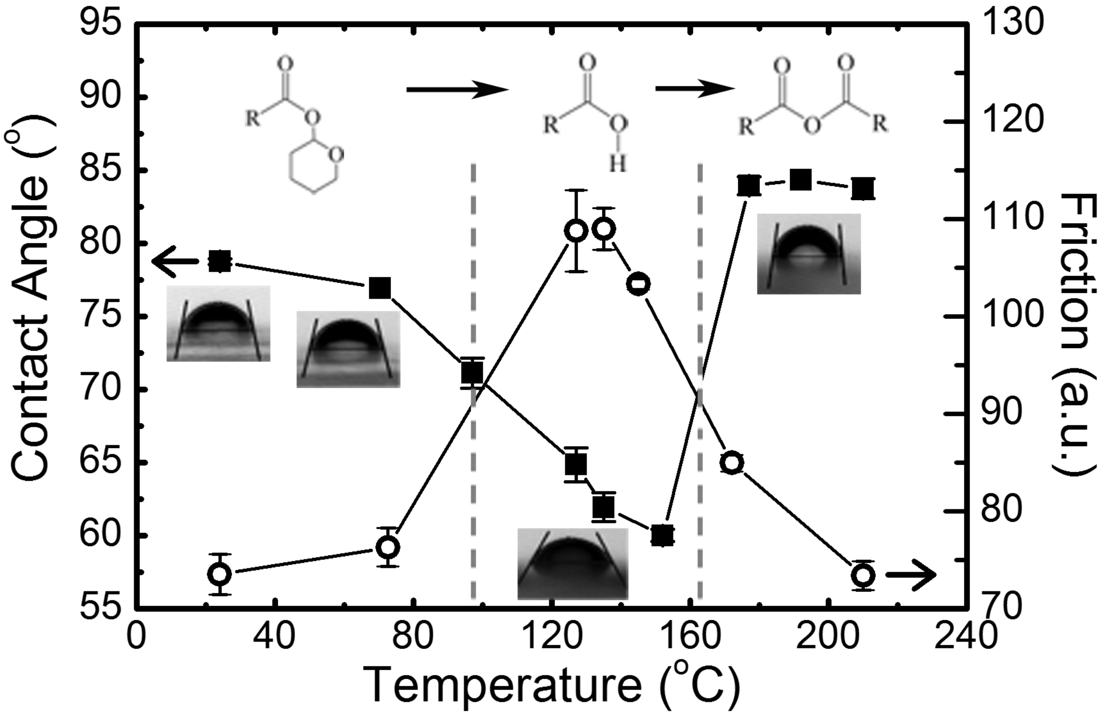

**Figure 2.3.3:** Static water contact angle (solid squares) and friction force (open circles) measurements of p(THP-MA)$_{80}$p(PMC-MA)$_{20}$ copolymer as a function of heating temperature [94].

of vibrational modes (Raman scattering) [106].

The Raman effect is due to the interaction of the electromagnetic field of the incident radiation, $E_i$, with a molecule. The field may induce an electric dipole in the molecule given by:

$$p = \alpha E_i, \tag{2.4.1}$$

where $\alpha$ is the polarizability of the molecule and $p$ is the induced dipole. The electric field due to the incident radiation is a time-varying quantity of the form:

$$E_i = E_0 \cos(\omega_i t). \tag{2.4.2}$$

For a vibrating molecule, the polarizability is also a time-varying term that depends on the vibrational frequency of the molecule $\omega_v$:

$$\alpha = \alpha_0 + \alpha_v \cos(\omega_v t). \tag{2.4.3}$$

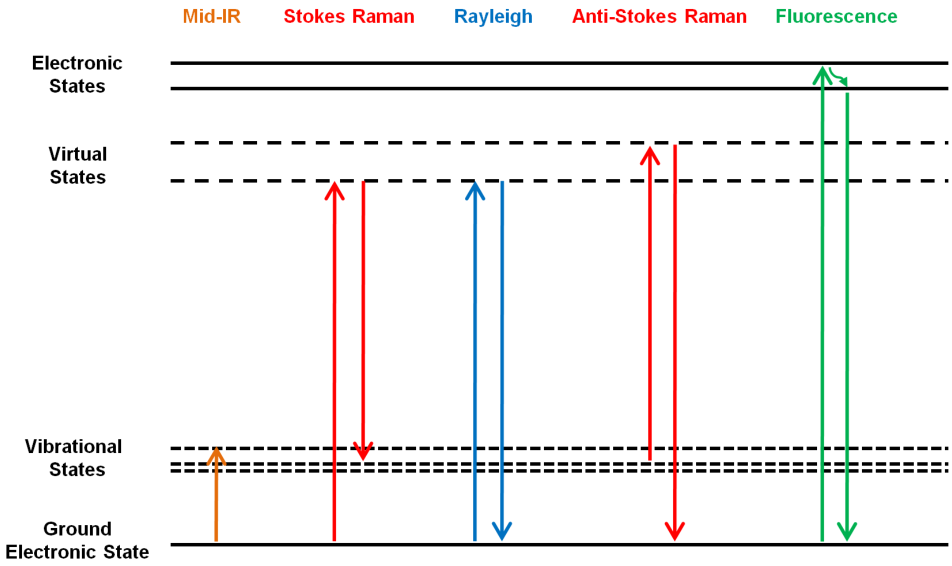

**Figure 2.4.1:** Jablonski energy diagram for infrared absorption, Raman scattering, Rayleigh scattering, and fluorescence.

Multiplication of Eq. 2.4.2 and Eq. 2.4.3 yields Eq. 2.4.1 in the following form:

$$p = \underbrace{\alpha_0 E_0 \cos(\omega_i t)}_{p_R} + \underbrace{\frac{\alpha_v E_0}{2} \cos\left[(\omega_i - \omega_v)t\right]}_{p_S} + \underbrace{\frac{\alpha_v E_0}{2} \cos\left[(\omega_i + \omega_v)t\right]}_{p_A}, \tag{2.4.4}$$

where the first term $p_R$ represents the elastic Rayleigh scattering of the incident radiation, the second term $p_S$ represents the Stokes scattering which is the Raman scattering with energy lower than incident radiation, and last term $p_A$ represents the Anti-Stokes scattering which is the Raman scattering with energy higher than incident radiation (shown in Fig. 2.4.1).

The intensity ratio of these two types of Raman scattering can be calculated as:

$$\frac{I_S}{I_A} = \left(\frac{\omega_i - \omega_v}{\omega_i - \omega_v}\right)^4 \exp\left(\frac{\hbar\omega_v}{k_B T}\right). \tag{2.4.5}$$

Since at room temperature the molecules are principally at their ground states, the Raman scattering is dominated by Stokes scattering. The intensity of anti-Stokes scattering is about one order of magnitude smaller than that of Stokes scattering.

The modes of vibrations of a molecule may be demonstrated by a classical analogy where atoms are represented by weights and interatomic forces by springs. It can be shown that the complex motions of the weights are combinations of $3N$-5 normal modes of vibrations for linear molecules, or $3N$-6 in the case of non-linear molecules. Some examples of the normal modes of vibrations are: stretching motion, bending motion, rocking motion, and out-of-plane deformation.

Raman spectroscopy and IR spectroscopy are complimentary vibrational techniques because some normal modes of vibration are Raman active but IR inactive, and *vice versa*. There are selection rules that govern the ability of a molecule to be detected by Raman spectroscopy or IR spectroscopy. For a vibration mode to be Raman active, the polarizability must change with the vibration. For a vibration to be IR active, the dipole moment of the molecule must change with the vibration. For example, symmetric stretching vibration mode is Raman active but IR inactive [105].

For this thesis research, Raman spectroscopy was used for characterize TCNL made PPV and reduced graphene oxide micro-structures. Spectroscopy measurements were performed in a Horiba LabRAM HR800 micro Raman system coupled with a Olympus BX41 inverted optical microscope. The use of a confocal Raman microscope enables micrometer scale high spatial resolution chemical identification. This is particularly useful for thin film sample measurements. High power diode laser ($\lambda = 785$ nm and 532 nm, $I_{max} = 20$ mW) was used to acquire the weak Stokes Raman scattering signal radiated from the sample. With its high density grating and high focal length, the spectrometer was able to provide 0.3 $cm^{-1}$ to 1 $cm^{-1}$ high spectral resolution. Fig. 2.1.6 shows a series of Raman measurements of a group of control samples: SiC, epitaxial graphene, and chemically oxidized graphene.

IR spectroscopy was used to verify the thermochemical reaction of bulk-heated ester and carbamate copolymer samples. Measurements were performed in a Digilab UMA-600 Fourier transform (FT) IR system. A 125 W ceramic filament was used a as mid-IR radiation source. The interferometric spectrometer generated interferometry pattern with transmission efficiency at specific wavelengths. A FT algorithm was employed to analyze the interferogram. The advantages of FTIR are that it provide high throughput (10 scans per second) and high spectral resolution (0.25 $\text{cm}^{-1}$). In order to produce the best spectral reproducibility, the technique of attenuated total reflectance (ATR) was used. The ATR accessory operated by measuring the changes that occur in a totally internal reflected IR beam when the beam comes into contact with a sample. The IR beam was directed on to an optically dense crystal with high refractive index (Germanium). This internal reflectance creats an evanescent wave that extends 0.5 $\mu$m to 5 $\mu$m beyond the crystal surface. As with confocal Raman microscope, the use of ATR is particularly useful for our study of thin film copolymer samples (film thickness about 0.1 $\mu$m to 2 $\mu$m). A series of FTIR measurements of ester copolymer bulk samples heated at selected temperatures are shown in Fig. 4.1.2.

## *2.5 Epifluorescence Microscopy*

Fluorescence microscopy was intensively used in the study of assembling nano-objects with TCNL made nano-templates (Section 4.2). Fluorescence is a molecular phenomenon in which a fluorescing molecule absorbs light of certain range of wavelengths (excitation) and almost instantaneously radiates light of lower energies and thus longer wavelengths (emission) [107, 108].

Many organic and inorganic materials exhibit certain fluorescence when irradiated. Such primary fluorescence (or autofluorescence) is often extremely faint or non-specific. Many fluorophores with very bright fluorescence have been developed and are used to selectively stain molecules of interest. The use of fluorophores make it possible to identify sub-micron biological molecules, such as proteins and DNA, that are bond to TCNL nano-templates. Fluorescence microscopy is able to provide high degree of specifity among non-fluorescing material. It can reveal the presence of fluorophores with exquisite sensitivity. As few as 50 fluorescing molecules per cubic micron can be detected. For a given sample, through the use of multiple steps of staining, different fluorophores with distinctive emission characteristics will reveal the presence of different target molecules. Although the fluorescence microscopy cannot provide spatial resolution below the diffraction limit of half of visible wavelength, the presence of fluorophores below such limits is made visible using confocal microscope [109].

Epifluorescence microscopy is the most common type of fluorescence microscopy. Its most important feature is that by illuminating with incident light (*i.e.* episcopic illumination) it need only filter out excitation light scattering back from the sample. High magnification objective lenses with high numerical aperture (60x: NA 1.2, 100x: NA 1.4) are used to eliminate surface reflections. In addition, the dichroic beamsplitter inside the filter cube is able to filter out back-scattered excitation light by a factor up to 500.

For this thesis research, epifluorescence microscopy was performed on a Nikon TE2000 inverted microscope. A Plan Apo 60x water immersion objective and a Plan Apo 100X oil immersion objective were used to obtain high resolution fluorescence images. Samples were illuminated by the radiation from a mercury lamp a Nikon for illumination. The fluorescence signal was collected by a Nikon EM-CCD monochrome digital CCD camera. This CCD camera works at -30 ℃ and is specifically designed for high sensitivity fluorescence imaging.

The primary filtering element in the epifluorescence microscope is the set of three filters housed in the fluorescence filter cube: the excitation filter, the emission filter and the dichroic beamsplitter. Three types of filter cubes were used for our research: UV-2EC DAPI filter set for UV region(excitation 340-380 nm, dichroic splitter DM400, emission 435-485 nm), FITC/GFP HyQ filter set for green color region (excitation 460-500 nm, dichroic mirror DM505, emission 510-560 nm), and Cy5 HQ filter set for red color region (excitation 620-660 nm, dichroic mirror DM Q660LP, emission 700-775 nm). The fluorescence images were processed with ImageJ software.

# CHAPTER III

# THERMOCHEMICAL NANOLITHOGRAPHY FUNDAMENTALS

## *3.1 Instrumentation*

Thermochemical Nanolithography (TCNL) is carried out with a modified Veeco AFM system. The system consists of a Multimode IV AFM microscope (Fig. 3.1.1), a Nanoscope IV electronic controller unit, and Nanoscope control software running on a PC computer.

TCNL is able to achieve local chemical modification on surfaces by utilizing a silicon AFM cantilever integrated with a Joule-heating resistive heater (Fig. 3.1.2). These customized AFM cantilevers were provided by Prof. King's group [110]. They were made using a standard silicon-on-insulator (SOI) process following a documented fabrication process. The process started with an SOI wafer of orientation $< 100 >$, n-type doping at $2 \times 10^{14}$ cm$^{-3}$ and having a resistivity of approximately 4 $\Omega$-cm. The cantilever tip was formed using an oxidation sharpening process and typically have a radius of curvature about 20 nm and a height of 1.5 $\mu$m. The cantilevers were made electrically active by selectively doping different parts of the cantilever through a two-step process. First, a low-dosage blanket ion implantation was performed on the entire cantilever and furnace-annealed in order to establish an essentially uniform background doping level ($10^{17}$ cm$^{-3}$, phosphorous n type). The cantilever was then subjected to a heavy implantation step during which a region around the tip (width 8 $\mu$m)is masked off ($10^{20}$ cm$^{-3}$, phosphorous n type). The masked region became a relatively lightly doped region at the free end of the cantilever, *i.e.* the resistive heater. The cantilever was electrically connected to the base via highly conducting legs (length

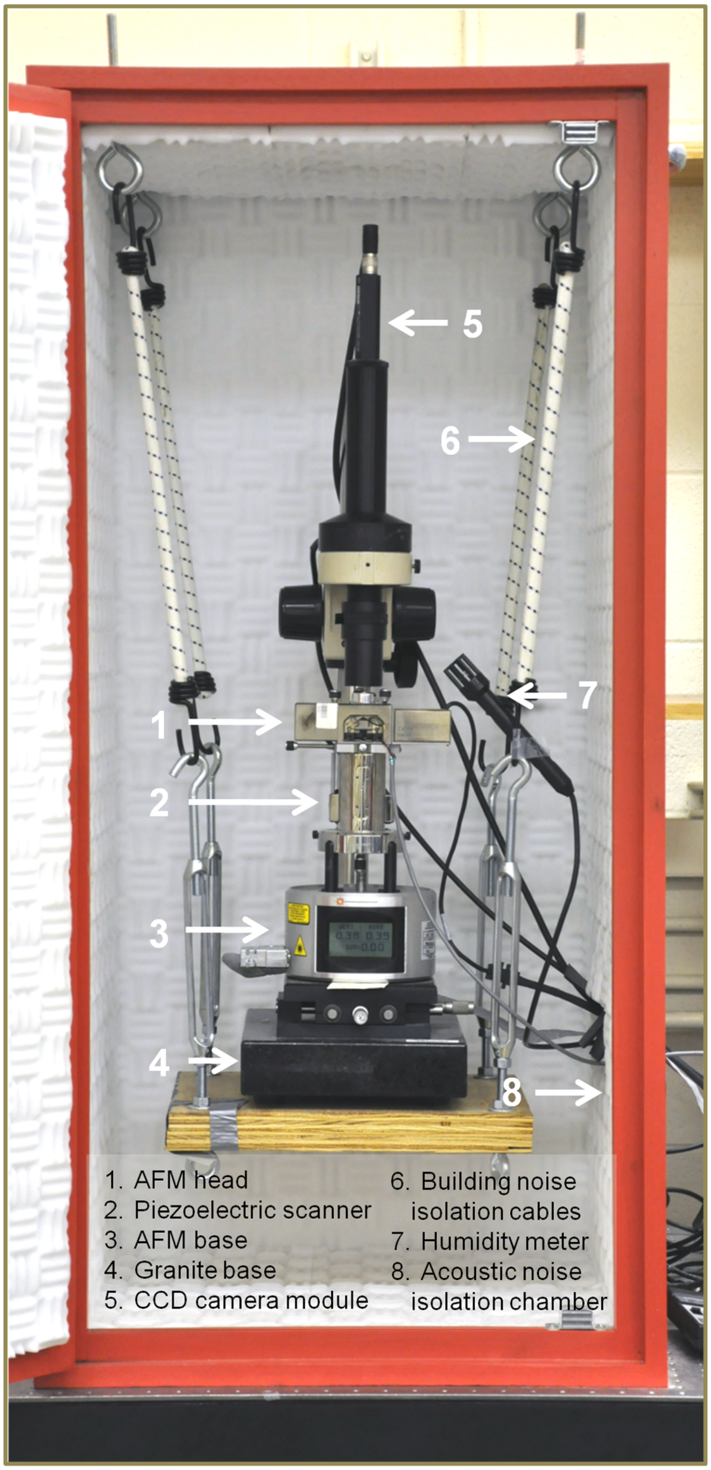
5
6
7
1
2
3
4
8
1. AFM head
2. Piezoelectric scanner
3. AFM base
4. Granite base
5. CCD camera module
6. Building noise isolation cables
7. Humidity meter
8. Acoustic noise isolation chamber

**Figure 3.1.1:** Veeco MultiMode IV AFM microscope.

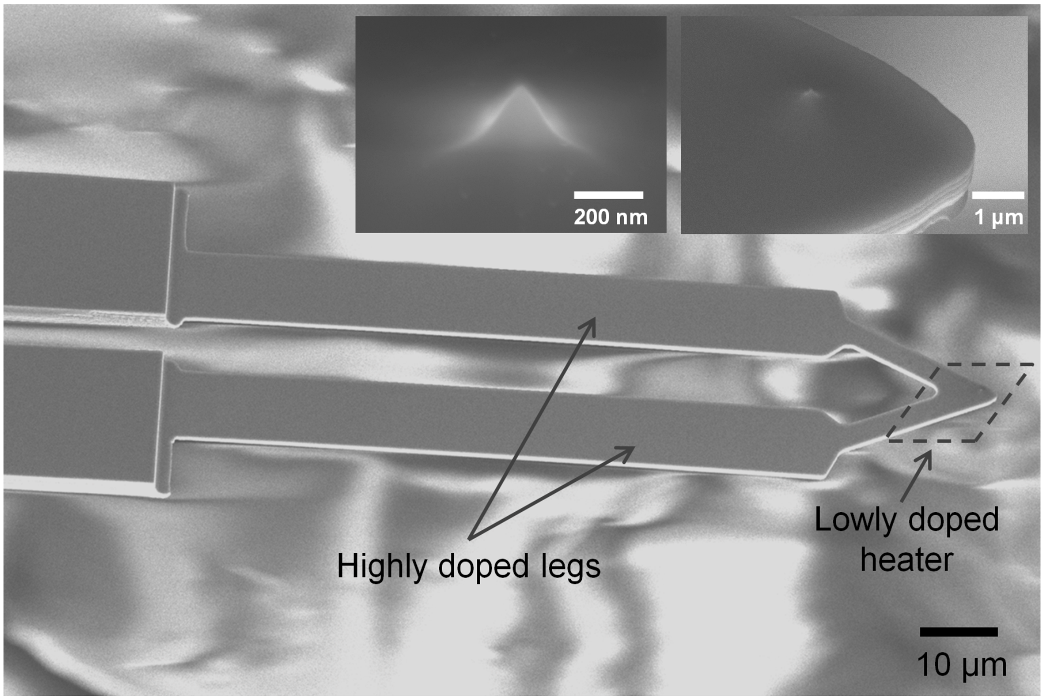

**Figure 3.1.2:** SEM micrograph of a TCNL thermal cantilever. The tip sits above the integrated resistive heater (shown as inset).

110 $\mu$m, width 15 $\mu$m). With the cantilever dimensions and temperature-dependent resistivity, the heater accounts for more than 90% of the electrical resistance of entire cantilever.

A customized printed-circuit-board (PCB) cantilever holder and a chip holder were designed to place TCNL thermal cantilevers into the commercial Veeco AFM microscope head as shown in Fig. 3.1.3.

Figure 3.1.4 shows a schematic of TCNL system setup used to operate the heated AFM probe throughout this thesis. The electric circuit had a sense resistor, $R_s = 2$ k$\Omega$, connected to the cantilever in series to protect the probe by limiting the current at high power as well as to sense the current, $I_s$. An Agilent DC power supply (E3645A) was used to provide heating power to the thermal AFM cantilever with a DC voltage, $V_0$. A Fluke 73III multimeter measured the voltage drop across the sense resistor, $V_s$. A Labview control and measurement system was used to monitor the TCNL process as well as record $V_s$ and $V_0$. With this instrumentation, the cantilever

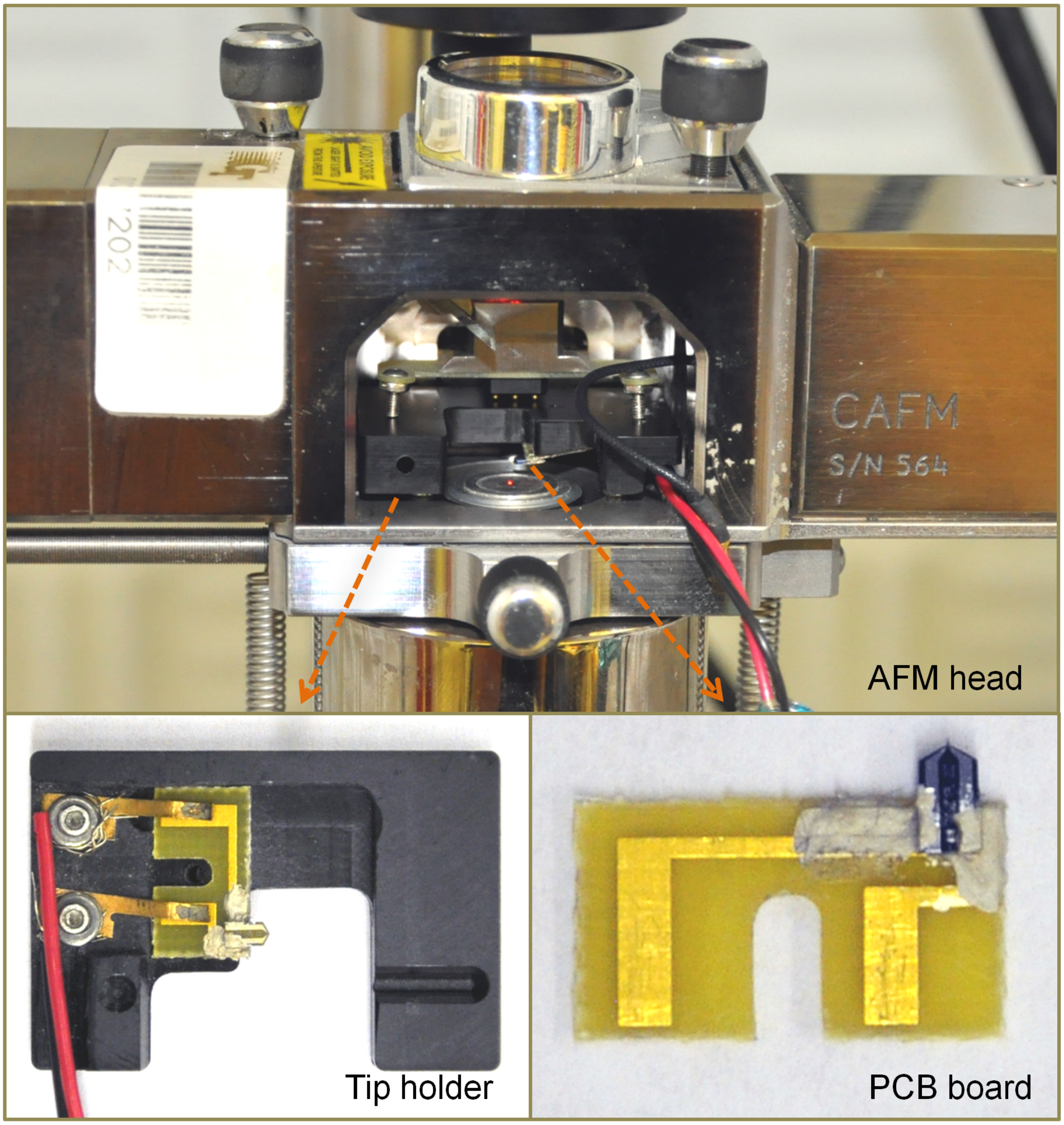
202
CAFM
S/N 564
AFM head
Tip holder
PCB board

**Figure 3.1.3:** Customized printed-circuit-board (PCB) cantilever holder and chip holder for Veeco Multimode AFM microscope head.

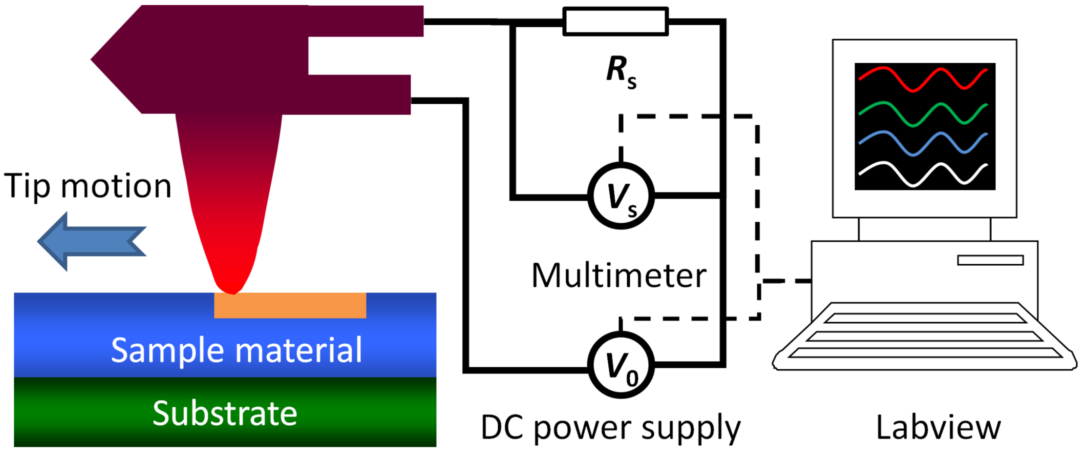

**Figure 3.1.4:** Schematic of Thermochemical Nanolithography (TCNL) system.

electrical resistance and power dissipation can be obtained.

In order to pattern desired arbitrary two dimensional geometries, such as arrays of dot, straight lines, zigzag lines, triangles or polygons, a nanolithography package is used to write C++ scripts used by the Veeco Nanoscope control software.

## *3.2 Cantilever Mechanical Characterization*

During TCNL operation, the interaction between the cantilever tip and the underlying substrate is of great importance. According to Hertz theory (Eq. 2.2.31), the normal loading force determines the contact area between cantilever tip and surface in contact mode, which directly relates to the TCNL spacial writing resolution and heating efficiency. In addition, it has often been noted in the literature that spring constants can vary greatly from one to another, even within the same batch process. This is because the techniques used to fabricate the probes can result in substantially different cantilever dimensions, particularly thickness of the cantilevers, from wafer to wafer and smaller variations within a single wafer. According to Eq. 2, a 10% variation in thickness can result in a variation of spring constant as large as 30%. Therefore, the TCNL process requires a precise measurement of the spring constant,

$k_can$, of each individual TCNL thermal cantilever.

There is a wealth of literature devoted to spring constant calibration techniques [111, 112, 113, 113]. The most common method is the geometry method based on cantilever geometries such as rectangular beam or V-shape beam. Due to the special, and complex geometry of the TCNL thermal cantilever, it is not straightforward to derive a simple, analytical calibration equation. Instead, we used another popular static deflection technique known as reference beam method [114, 115, 116]. In this method, a cantilever with a well-known spring constant is used as a calibrated reference cantilever. Two force curves of the TCNL thermal cantilevers need to be measured: one on the free end of the reference cantilever, while the other one on a hard surface. The spring constant of the cantilever $k_{can}$ then can be calculated from the slope of the contact portion of these two force curves (defined as deflection sensitivity $S$ in nm/V):

$$k_{can} = k_{ref}\left(\frac{S_{ref}}{S_{hard}} - 1\right), \tag{3.2.1}$$

where $k_{ref}$ is the spring constant of the reference cantilever, $S_{ref}$ is the deflection sensitivity measured on the reference cantilever, and $S_{hard}$ is the deflection sensitivity measured on a hard surface. The cantilever must be positioned so that it contacts the reference cantilever as close to its end as possible since the reference cantilever becomes progressively stiffer as loads are applied closer to its base. If the spring constant is measured with the tip offset from the end of the reference cantilever, it can be corrected by:

$$k_{adj} = k_{can}\left(\frac{L}{L - \Delta L}\right)^3, \tag{3.2.2}$$

where $k$ is the spring constant measured offset from the end of the cantilever as in Eq. 3.2.1, $L$ is the length of the reference cantilever, and $\Delta L$ is the distance that the tip is offset from the free end of the reference cantilever. This correction is exact for rectangular reference cantilevers. It is important to note that the tip should be positioned near the midline of the cantilever to avoid errors due to torsional bending.

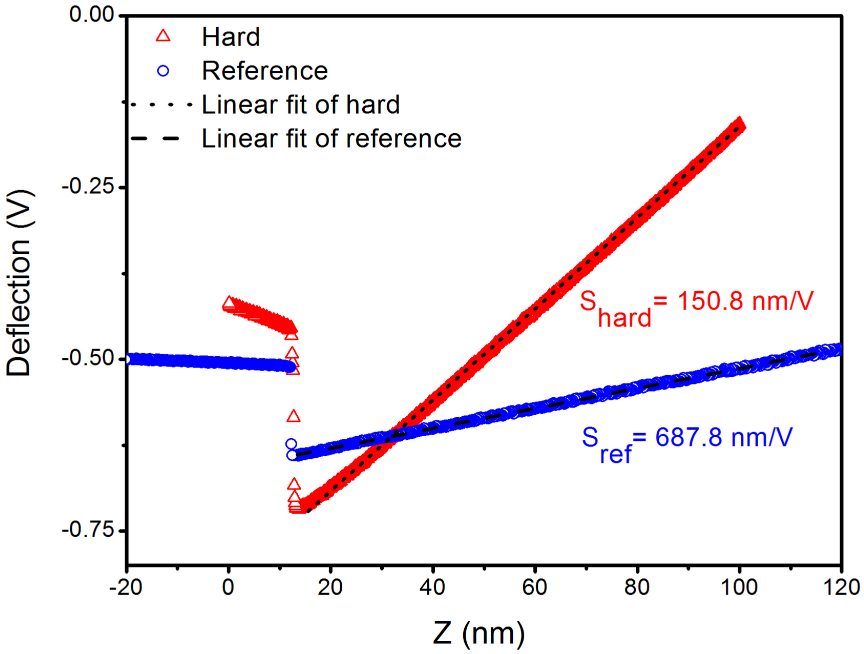

**Figure 3.2.1:** Spring constant calibration of TCNL thermal cantilever #26 with reference beam method.

In this thesis research, a type of tip-less commercially available cantilevers were used as reference cantilevers (TL-CONT, Nanosensors). They had been double calibrated with the geometry method (Eq. 2) and the frequency method (Eq. 2.2.6) ($k_{ref}$ $= 0.2 \pm 0.1$ N m$^{-1}$). The spring constants of the TCNL thermal cantilevers were determined as 0.2 - 1.0 N m$^{-1}$. An example is shown in Fig. 3.2.1. In this case, the reference cantilever has a spring constant $k_{ref} = 0.18$ N m$^{-1}$, its length was $L = 450$ $\mu$m, the tip offset length was $\Delta L = 30$ $\mu$m, the spring constant of TCNL thermal cantilever #26 was calculated to be 0.45 N m$^{-1}$.

## *3.3 Heat Transfer Modeling*

### 3.3.1 Heater temperature modeling

Since the local chemical changes are highly depent on the activation temperature, precise calibration of heater temperature ($T_H$, shown in Fig 3.3.1) is an essential component of this thesis research. The electrical resistance of the heater ($R_H$) varies

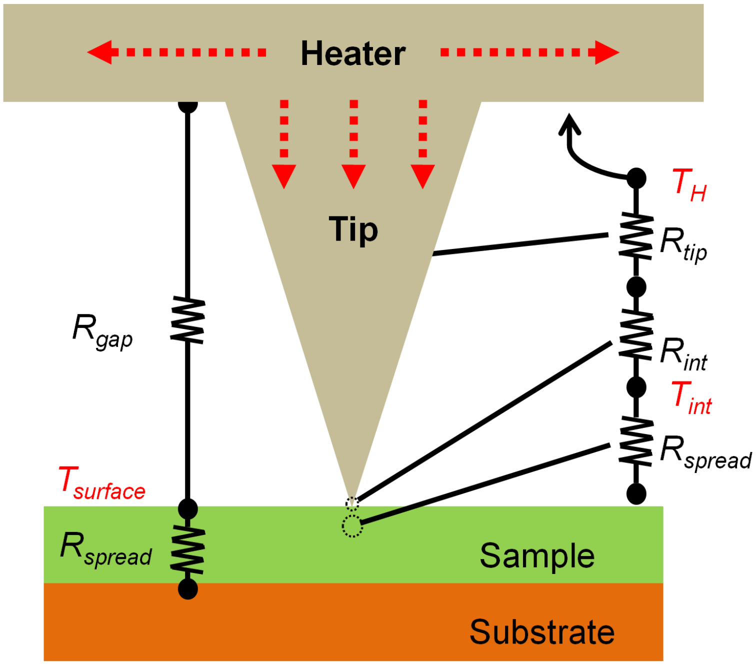

**Figure 3.3.1:** Thermal circuit for heat flow of a heated TCNL thermal cantilever, the tip, and the contact with sample.

nonlinearly with temperature and significant temperature gradients can exist in the whole cantilever. The TCNL process requires a systematic heat transfer modeling and experimental protocols to calibrate $T_H$.

The electrical resistivity of the doped silicon is a strong function of temperature. Fig. 3.3.2 shows the variation of $R_H$ with dissipated power of the heater, $P_H$, of a typical TCNL thermal cantilever. $R_H$ and $P_H$ can be obtained by:

$$R_H = R_s \frac{V_0 - V_s}{V_s}, \tag{3.3.1}$$

$$P_H = (V_0 - V_s)\frac{V_s}{R_s}, \tag{3.3.2}$$

where $V_0$ is the voltage generated by the power supply, $V_s$ and $R_s$ are the voltage drops and resistance of the sense resistor (Fig. 3.1.4).As shown in Fig. 3.3.2, the cantilever had a room temperature resistance near 1.2 kΩ, which could increase with temperature to a peak resistance of 4.5 kΩ at 550 ℃ where $P_H = 7.9$ mW.

Near room temperature, the cantilever resistance increases with temperature, since

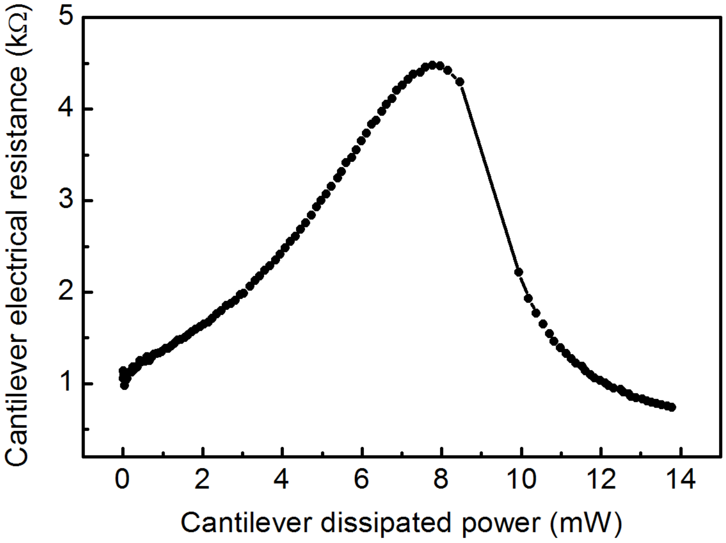

**Figure 3.3.2:** Variation of the electrical resistance of a TCNL integrated heater as a function of dissipated power. Competition between increased electron scattering and intrinsic carrier generation at elevated temperatures results in a peak resistance of 4.5 kΩ at 550 ℃ where $P_H = 7.9$ mW.

the carrier mobility in the doped silicon cantilever decreases with temperature. However, the intrinsic carriers in the silicon increase with increasing temperature. At approximately 550 ℃ (intrinsic temperature, $T_i$), the thermally generated intrinsic carriers become the dominant parameter affecting cantilever resistance, and the resistance decreases sharply. This thermal runaway effect has been well studied for cantilever heating at steady state [117, 118]. Due to the thermal runaway at higher power levels, the heated cantilever can have the same electrical resistance at two different heater temperatures, which precludes the use of resistance monitoring for temperature measurements. Therefore, using cantilever power as a measure of temperature has advantages over the resistance due to its one-to-one correspondence.

$T_H$ can be calibrated by measuring $P_H$ while externally heating the entire cantilever to an isothermal temperature, and by using external thermometry to measure $T_H$ while the cantilever was self-heated. Among external thermometry techniques, optical thermometry is advantageous for measuring $T_H$ because it does not require heat to diffuse from the cantilever into an external sensor. Micro-IR thermometry can measure temperature from the emitted radiation from a sample [40], but the spatial resolution of the IR microscope is diffraction-limited to 5 $\mu$m, which is similar to the total size of the cantilever heater. Raman spectroscopy has advantages over IR thermometry, as it has submicron lateral resolution and does not require calibrating the sample emissivity.

In Raman spectroscopy, the temperature of the illuminated region of the sample can be determined from several aspects of the Raman optical scattering signature: the position of the Stokes peak, the width of the Stokes peak, and the ratio of the Stokes peak to the anti-Stokes peak. The latter two provide absolute measurements of temperature but also require long accumulation times to account for statistical fluctuations and to resolve the weak anti-Stokes peak. Additionally, the ratio of the Stokes peak to the anti-Stokes peak loses sensitivity to temperature above 500℃ for silicon. The Stokes peak position can be measured quickly and accurately but is partially affected by stress within the sample. The model used to match the absolute frequency shift $\omega_{shift}$ and temperature is given by [119]:

$$\omega_{shift} = \omega_0 + A\left[1 + \frac{2}{\exp\left(\frac{\hbar\omega_0}{2kT}\right) - 1}\right] + B\left\{1 + \frac{3}{\exp\left(\frac{\hbar\omega_0}{3kT}\right) - 1} + \frac{3}{\left[\exp\left(\frac{\hbar\omega_0}{3kT}\right) - 1\right]^2}\right\}, \tag{3.3.3}$$

where $A$, $B$, and $\omega_0$ are material specific parameters for doped silicon. Although it is a non-linear relationship over a large temperature range, it is reasonable to assume a linear response of Stokes peak position for doped silicon cantilever between room tempearature and 1000 ℃, which is sufficient for most TCNL operations in this thesis.

Figure 3.3.3 shows a measurement of the Stokes peak position as a function of cantilever power using a commercial confocal Raman microscope with a 785 nm laser source. The data was taken while the laser spot was focused on the heater. The Stokes peak position shifts almost linearly with cantilever power. Therefore, a linear relationship between heater temperature $T_H$ and power $P_H$ can be established. $T_H$

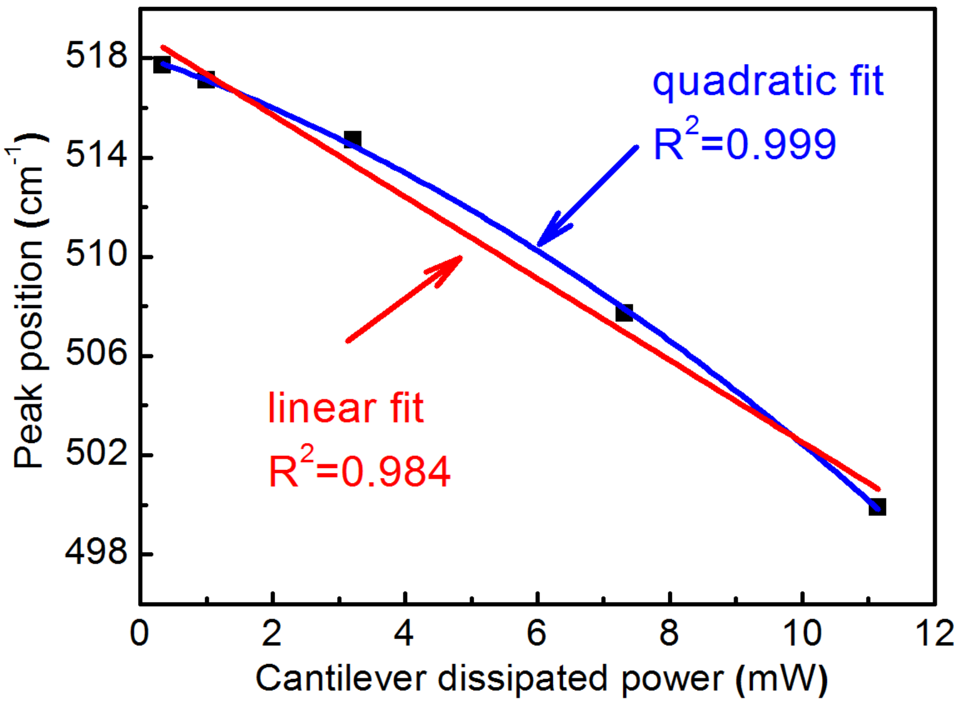

**Figure 3.3.3:** Stokes shift as a function of electrical power dissipated on the thermal cantilever. The linear relationship can be used to fit the peak position dependence of cantilever power even though the quadratic polynomial fits the data better.

can be estimated by:

$$T_H = RT + \frac{T_i - RT}{P_i} P_H, \tag{3.3.4}$$

where $RT$ is the room temperature, $P_i$ is the cantilever power at intrinsic temperature $T_i$. The cantilever temperature has been routinely calibrated several times before each TCNL operation. A Labview program was written to increase the ease of the calibration routine as shown in Fig. 3.3.4.

### 3.3.2 Local contact temperature modeling

During a TCNL thermal process, the temperature rise at the tip-sample-surface interface, $T_{int}$, is of greater interest than $T_H$ since $T_{int}$ is not generally the same as $T_H$. The difference between $T_{int}$ and $T_H$ depends on the thermal resistances of a number of components within the tip-sample system, as shown in Fig.3.3.1. The tip-sample

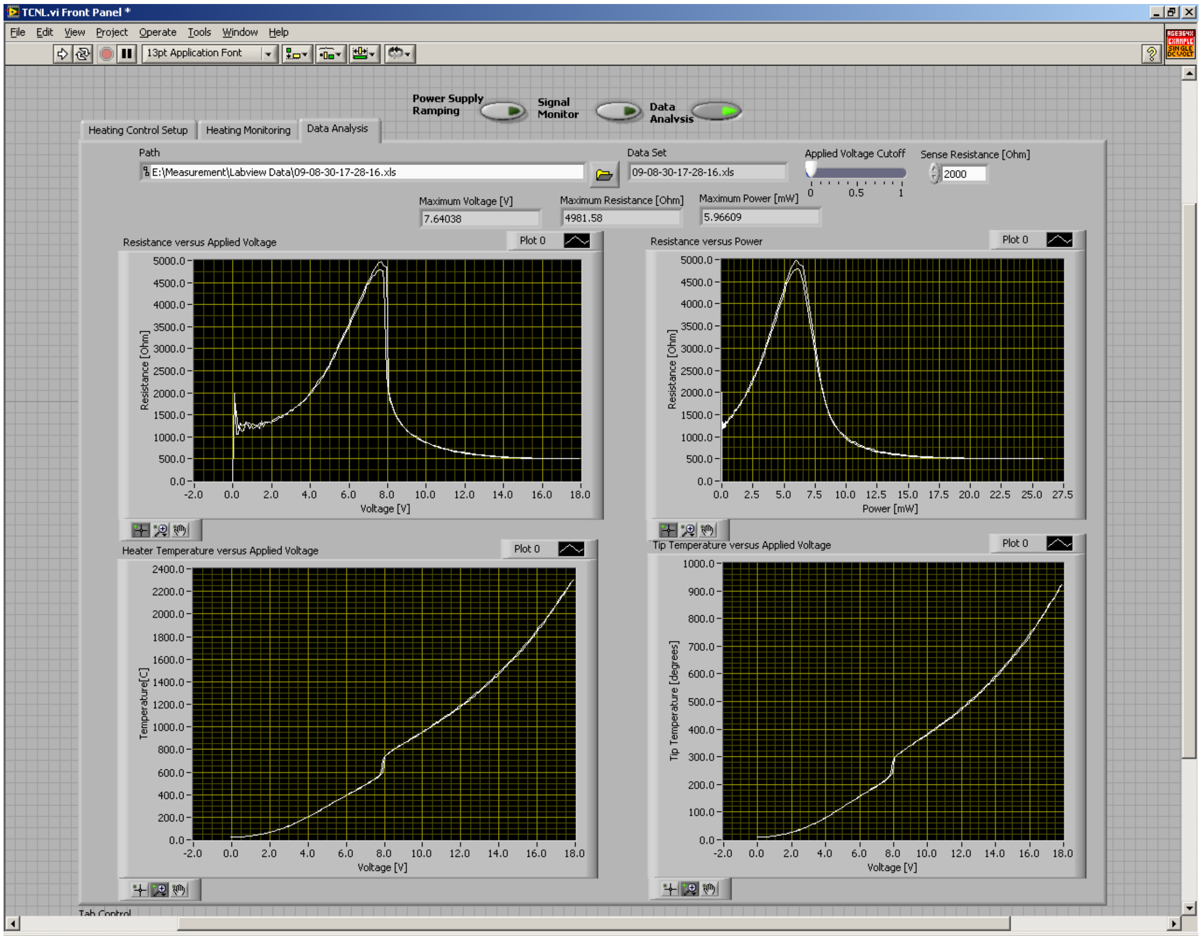
TCNL.vi Front Panel *
File Edit View Project Operate Tools Window Help
13pt Application Font
Power Supply Ramping
Signal Monitor
Data Analysis
Heating Control Setup
Heating Monitoring
Data Analysis
Applied Voltage Cutoff
0
0.5
1
Resistance versus Applied Voltage
Plot 0
Resistance [Ohm]
5000.0 4500.0 4000.0 3500.0 3000.0 2500.0 2000.0 1500.0 1000.0 500.0 0.0
-2.0 0.0 2.0 4.0 6.0 8.0 10.0 12.0 14.0 16.0 18.0
Voltage [V]
Resistance versus Power
Plot 0
Resistance [Ohm]
5000.0 4500.0 4000.0 3500.0 3000.0 2500.0 2000.0 1500.0 1000.0 500.0 0.0
0.0 2.5 5.0 7.5 10.0 12.5 15.0 17.5 20.0 22.5 25.0 27.5
Power [mW]
Heater Temperature versus Applied Voltage
Plot 0
Temperature[C]
2400.0 2200.0 2000.0 1800.0 1600.0 1400.0 1200.0 1000.0 800.0 600.0 400.0 200.0 0.0
-2.0 0.0 2.0 4.0 6.0 8.0 10.0 12.0 14.0 16.0 18.0
Voltage [V]
Tip Temperature versus Applied Voltage
Plot 0
Tip Temperature [degrees]
1000.0 900.0 800.0 700.0 600.0 500.0 400.0 300.0 200.0 100.0 0.0
-2.0 0.0 2.0 4.0 6.0 8.0 10.0 12.0 14.0 16.0 18.0
Voltage [V]
Tab Control

Path: E:\Measurement\Labview Data\09-08-30-17-28-16.xls
Data Set: 09-08-30-17-28-16.xls
Sense Resistance [Ohm]: 2000
Maximum Voltage [V]: 7.64038
Maximum Resistance [Ohm]: 4981.58
Maximum Power [mW]: 5.96609

**Figure 3.3.4:** Labview temperature calibration program. The four windows are used to estimate cantilever heater and tip temperature. Arranged from left to right then top to bottom, they are $R_{can}$ vs $V_0$, $R_{can}$ vs $P_{can}$,$T_H$ vs $P_{can}$, and $T_{int}$ vs $P_{can}$, respectively.

thermal circuit system includes thermal resistances of the tip ($R_{tip}$), tip-surface interface ($R_{int}$), and sample spreading resistance ($R_{spread}$). Heat also flows directly from the cantilever heater to the substrate through the ambient air, with thermal resistance $R_{gap}$. The dominant mode of heat transfer is through the ambient air, as $R_{gap}$ is approximately an order of magnitude smaller than the total thermal resistance through the tip. However, the temperature rise on the sample surface due to the heat transfer through air, $T_{surface}$, is controlled by the thermal conductivities of ambient air and sample, and thus $T_{surface} \ll T_{int}$. This makes the TCNL thermal cantilever-tip an attractive instrument for performing highly localized thermal processing.

The thermal resistance of the tip, $R_{tip}$, originates from the conductance of the phonons within the silicon tip and from the layer of native oxide covering it. The thermal conductivity is given by [120]:

$$k = \frac{1}{3} C v \left( \Lambda_0^{-1} + d^{-1} \right)^{-1}, \qquad (3.3.5)$$

where $k$ is the thermal conductivity, $C$ is the volumetric heat capacity, $v$ is the average phonon speed, $\Lambda_0$ is the temperature-dependent phonon mean free path in the bulk material, and $d$ is the diameter of the structure. $Cv$ is $1.8 \times 10^9 \mathrm{W/m^2K}$ and $\Lambda_0$ is 260 nm for bulk silicon at room temperature. It can be clearly seen that the resistivity inside the tip increases with respect to bulk silicon because of (1) enhanced phonon scattering with boundary surfaces, and (2) reduction of the cross section area towards the tip apex ($d$ changes from 1 $\mu$m at tip base to 10 nm at the tip-surface contact). The integral expression of $R_{tip}$ for varying $d$ is given by [121]:

$$R_{tip} = \int_{2rL/D}^{L} \frac{dz}{k(z)A(z)} = \frac{3}{2Cva} \left[ 1 - \left( \frac{2a}{D} \right)^2 \right] + \frac{4}{2k_{tip}a} \left( 1 - \frac{2a}{D} \right), \qquad (3.3.6)$$

where $z$ is the height from the tip apex to tip base, $L$ is the tip length, $D$ is the tip base diameter, $a$ is the contact radius determined by Eq. 2.2.31, $k_{tip}$ is the bulk thermal conductivity of the tip, $k_z$ is the height-dependent thermal conductivity as shown in Eq. 3.3.5. The above integral yields a thermal resistance of the order of $10^6$

K/W due to phonon scattering. It is important to note that over 90% of $R_{tip}$ occurs at the first 10% of the tip length. The end of the tip thus governs heat transport through the entire structure.

At the tip-sample interface, thermal resistance occurs due to phonon scattering at the interface. The interfacial resistance can be estimated as [122]:

$$R_{int} = \frac{r_{int}}{\pi a^2}, \tag{3.3.7}$$

where $r_{int}$ is the thermal boundary resistance. Experimental measurements of $r_{int}$ for solid-solid contacts near room temperature typically give a range of $10^{-9}$ m$^2$·K·W$^{-1}$, which is smaller than typical bulk thermal contact resistances. We expect $R_{int}$ in the range of $10^7$ K·W$^{-1}$ for $a$ around 5 nm.

The contact of a TCNL thermal cantilever-tip with a flat sample surface can be approximated as a circular heat source in contact with a flat, homogeneous semi-infinite surface, which has a spreading resistance given by [123]:

$$R_{spread} = \frac{1}{\pi k_{sam} a} \int_0^\infty \left[\frac{1 + K\exp(-2\zeta t_{sam}/a)}{1 + K\exp(-2\zeta t_{sam}/a)}\right] J_1(\zeta)\sin(\zeta)\frac{d\zeta}{\zeta^2}, \tag{3.3.8}$$

where the thermal conductivity parameter $K$ is defined as

$$K = \frac{1 - \frac{k_{sub}}{k_{sam}}}{1 + \frac{k_{sub}}{k_{sam}}}, \tag{3.3.9}$$

$k_{sam}$ and $t_{sam}$ are the thermal conductivity and thickness of the sample film, $k_{sub}$ is the thermal conductivity of substrate, $J_1$ is the Bessel function. For TCNL nanolithography systems, most of the samples are polymer thin films deposited on glass slides. Given $k_{sam}$ of polymer $\sim$ 0.2 W·K$^{-1}$·m$^{-1}$ [124], $k_{sub}$ of glass $\sim$ 1.1 W·K$^{-1}$·m$^{-1}$ [124], $t_{sam}$ of polymer film $\sim$ 100 nm, Eq. 3.3.8 yields $R_{spread} \sim 10^8$ W·K$^{-1}$. For a graphene oxide system, graphene oxide is covered on SiC surfaces. Given $k_{sam}$ of graphene oxide $\sim$ 1.9 W·K$^{-1}$·m$^{-1}$ [125], $k_{sub}$ of SiC $\sim$ 380 W·K$^{-1}$·m$^{-1}$ [126], $t_{sam}$ of polymer film $\sim$ 20 nm, Eq. 3.3.8 yields $R_{spread} \sim 10^7$ W·K$^{-1}$.

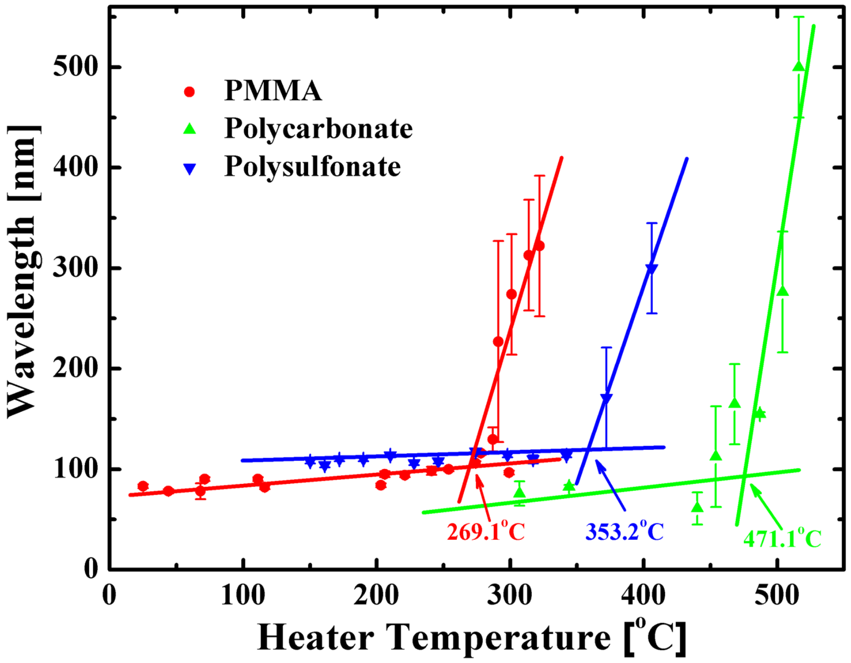

**Figure 3.3.5:** TCNL heating efficiency calibration with PMMA, polycarbonate and polysulfonate [94].

From the above discussion, we can estimate $T_{int}$ by evaluation of the proportion of each thermal resistance component in the thermal circuit via the heater-tip heat transfer route. We define heating efficiency, $c$, as the ratio between $T_{int}$ and $T_H$ which can be expressed as:

$$c = \frac{T_{int}}{T_H} = \frac{R_{spread}}{R_{tip} + R_{int} + R_{spread}}. \tag{3.3.10}$$

We can summarize that $c \sim 60\%$ - $70\%$ for polymer-glass sample-substrate system and $c \sim 10\%$ - $15\%$ for graphene oxide-SiC sample-substrate system. The heating efficiency value for polymer samples was verified experimentally by measuring temperature dependent polymer surface ripple wavelength. The thermal cantilevers were used to scan a polymer surface in contact mode. With the tip scanning at very low heater temperature, the polymer surface was smooth and ripples were formed. However, ripples only began to become visible with increased heater temperature.

At moderate heater temperatures, the wavelength increases linearly with temperature. Above a critical heater temperature, the wavelength increases at a significantly faster rate (see Fig. 3.3.5). The critical heater temperature is defined as the intersection of the linear fits of the two distinct regions. Macroscopic heating measurements show that the critical heater temperature corresponds to the glass transition temperature of the polymer ($T_g$). We used three commercial thermoplastic polymers with well known $T_g$: polysulfonate ($T_g$ = 240 ℃), polycarbonate ($T_g$ = 150 ℃) and poly(methylmethacrylate) (PMMA, $T_g$ = 110 ℃, Sigma-Aldrich).From the data in Fig. 3.3.5, we find that the ratio between the polymer surface temperature and the cantilever heater temperature is about 40%.

### 3.3.3 Writing kinetics modeling

According to the TGA analysis of the carbamate copolymer (Fig. 2.1.4), the deprotection of amine groups occurs around 160 ℃. However, there is a significant temperature mismatch between the TCNL writing temperature and the bulk reaction temperature as indicated by TGA analysis. TCNL experiments show that the deprotection starts when the cantilever heater temperature rises to around 410 ℃. Even considering the heat transfer circuit previously discussed, $T_{int}$ is required to rise to about 300 ℃. This is because the thermal reaction involved in TCNL writing process usually occurs on the time scale of milliseconds. This corresponds to several orders of magnitude faster than normal TGA temperature ramping rates (0.1 ℃·second$^{-1}$).

Assuming the thermal deprotection of an amine follows first order thermal kinetics, the rate constant ($K$) is temperature dependent and follows the Arrhenius equation [127]:

$$-\frac{dw}{dt} = Kw, \tag{3.3.11}$$

and,

$$K = A\exp\left(\frac{E_a}{RT}\right), \tag{3.3.12}$$

where $w$ is the remaining weight ratio, $A$ is the pre-exponential factor, $E_a$ is activation energy, and $R$ is universal gas constant. By arranging the above kinetics equation Eq. 3.3.11, we obtain the following linear equation:

$$\ln\left(-\frac{d\ln w}{dT}\right) = \ln\left(\frac{A}{C}\right) - \frac{E_a}{R}\frac{1}{T}, \tag{3.3.13}$$

where $C$ is the heating rate.

Using Eq. 3.3.13, we can obtain $E_a$ and $A$ of the carbamate polymer thermal reaction through a linear fit of the TGA curve. This is shown in Fig. 3.3.6(B). The TGA data is chosen between 120 ℃ and 180 ℃ because this is where the weight loss occurs. The data is fitted quite well by a linear equation. From the slope and intercept of the linear fit equation, we obtain $E_a = 159$ kJ mol$^{-1}$ and $A = 1.70 \times 10^{16}$ sec$^{-1}$. From these fitted values we calculate TGA curves under various temperature ramping conditions with Matlab. The simulated TGA curve with a temperature ramping rate of 5 ℃ min$^{-1}$ provides a good fit for the measured TGA data as shown in (A). Simulated TGA curves with various TCNL writing speeds and normal loading forces are plotted in (C) and (D) respectively. For a moderate TCNL writing speed of 10 $\mu$m sec$^{-1}$, and normal loading force of 100 nN, we estimate the local heating time to be 1.7 milliseconds. This corresponds to a temperature ramping rate of $10^7$ ℃ min$^{-1}$ which is six orders of magnitude faster than a typical TGA ramping rate. Thus it requires a significantly higher temperature (around 350 ℃) to initiate the amine deprotection. The simulation results indicates that decreasing the writing speed (down to a few nm sec$^{-1}$) is an effective way to reduce the heater temperature during TCNL process. Increasing normal loading force is not a judicial choice since it has limited effect on reducing heater temperature and it can induce undesirable physical damage to the soft polymer film surface.

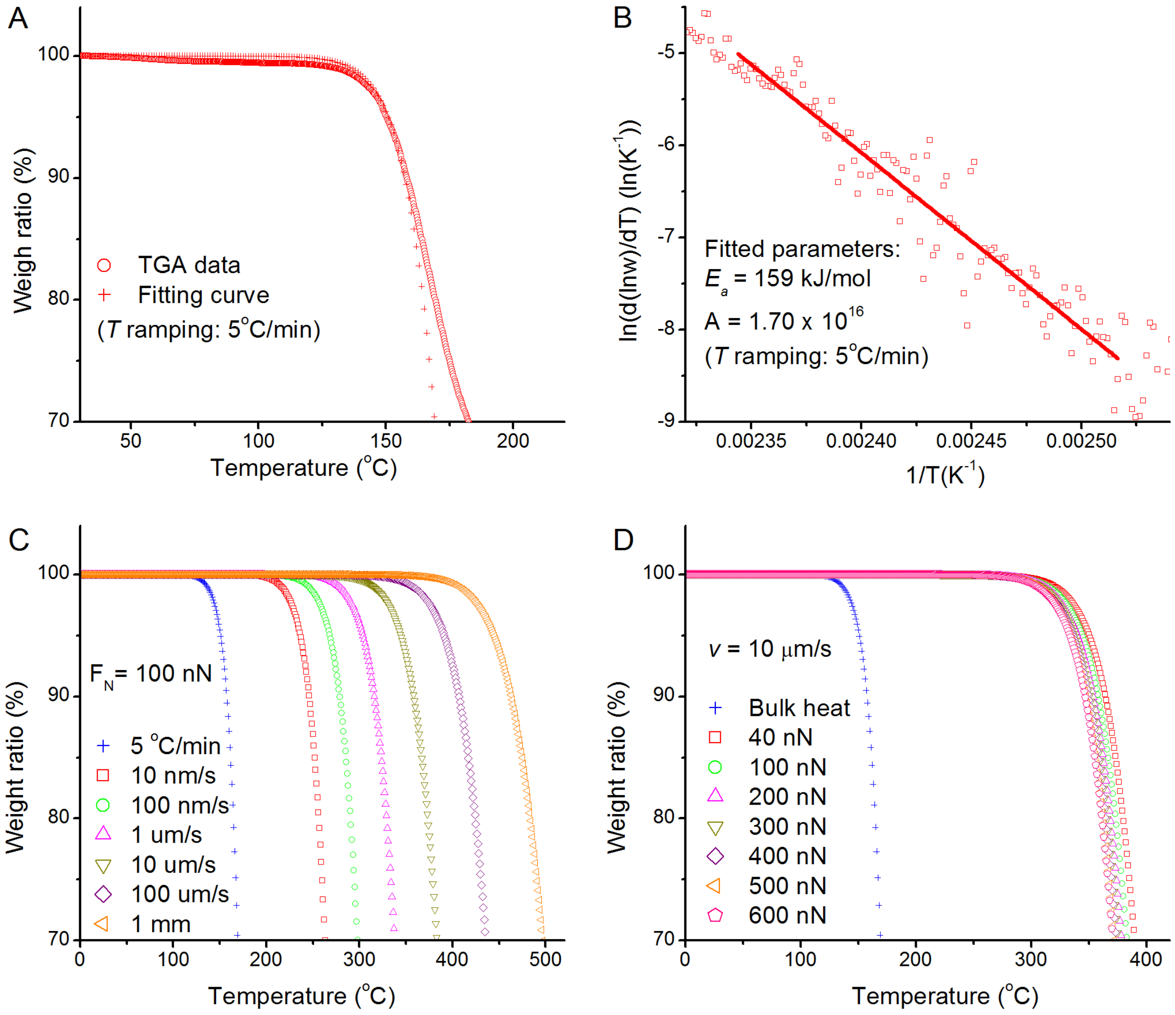

**Figure 3.3.6:** Thermal kinetic analysis of carbamate copolymer thermogram. (A) TGA thermogram of carbamate copolymer as well as a fitting curve generated from Eq. 3.3.11. (B) Linear fit of TGA data gives $E_a$ and $A$. (C) Writing speed dependence of remaining weight ratio. (D) Normal loading force dependence of remaining weight ratio.

## *3.4 Spatial Resolution Modeling*

Since high spatial resolution of nanostructures is extremely desirable for a variety of nanotechnology applications. In particular, we are interested in investigating TCNL's potential for fabricating sub 100 nm chemical nanostructures. To this end we analyze the temperature profile in the vicinity of tip-surface contact using a finite element modeling (FEM) software tool COMSOL.

Figure 3.4.1 shows a steady-state heat transfer FEM model of TCNL tip-sample surface system. Part (A) is a cross section plot of temperature distribution inside a 50 nm thick carbamate copolymer. A semi-sphere represents the tip apex with a radius of 20 nm. The normal loading force $F_N = 100$ nN results in a tip-surface contact radius about 9 nm and a penetration into the polymer film of about 2 nm. $T_{int}$ is set as 400℃. The writing speed of the TCNL tip, $v$, is 10 $\mu$m sec$^{-1}$. As seen from this figure, the temperature shows a rapid decay within a narrow range from the tip-sample contact. A critical temperature must be achieved to ensure the deprotection of amine groups. According to the discussion in Section 3.3.3, the critical temperature is much higher than $T_d$ measured by TGA (160℃) as required by the fast local heating process. We used the following relation to estimate the amine conversion ratio ($R_c$) for a range of temperatures [128]:

$$R_c = 1 - \exp\left(-Kt\right) = 1 - \exp\left[-A\exp\left(-\frac{E_a}{RT}\right)t\right], \tag{3.4.1}$$

where $t$ is the TCNL local heating time determined by writing speed $v$ and contact radius. Using the Arrhenius parameters obtained in Section 3.3.3, we translate the temperature plot in (A) to an amine conversion plot in (B). Temperature and conversion line profiles along lateral direction ($z = 0$) and vertical direction ($x = 0$) are plotted in (C) and (D) respectively. These profiles indicate the full deprotection of amine groups occurs across a narrow temperature range of 380℃ to 400℃ which corresponds to a spatial range of 2 nm to 3 nm within the vicinity of the tip-surface contact. The conversion ratio decays even faster than temperature does. The conversion ratio drops to zero only 6 nm away from the contact where the temperature is still 160℃. The lateral spatial resolution under such TCNL writing condition is thus determined as 20 nm.

Changing the interface temperature $T_{int}$ can effectively control the spatial resolution. We simulate and plot the temperature dependence of lateral spatial resolution with $T_{int}$ ranging between 250 ℃ and 600 ℃ in Fig. 3.4.2 (A). No full deprotection occurs at the tip-surface contact below 350 ℃. When $T_{int} > 400$ ℃, spatial resolution increases quasi-linearly with $T_{int}$ as predicted from Eq. 3.4.1.

For a given temperature $T_{int} = 400$℃, writing speed $v$ and normal loading force $F_N$ both affect the spatial resolution since they are related to the local heating time $t$. Increasing writing speed decreases the local heating time, whereas increasing loading force increases contact area and thus increases the local heating time. This dependence of the lateral spatial resolution is simulated and plotted in Fig. 3.4.2 (B) and (C) respectively. In Fig. 3.4.2 (B), the resolution increase exponentially with decreasing writing speed when $v \leq 100$ $\mu$m sec$^{-1}$. This is the result of the $t$ exponential dependence of the conversion ratio $R_c$ according to Eq. 3.4.1. In the case of loading force dependence as shown in Fig. 3.4.2 (C), due to a 1/3 power dependence of the contact radius shown in Eq. 2.2.31, the later spatial resolution shows a 1/3 power dependence of normal loading force.

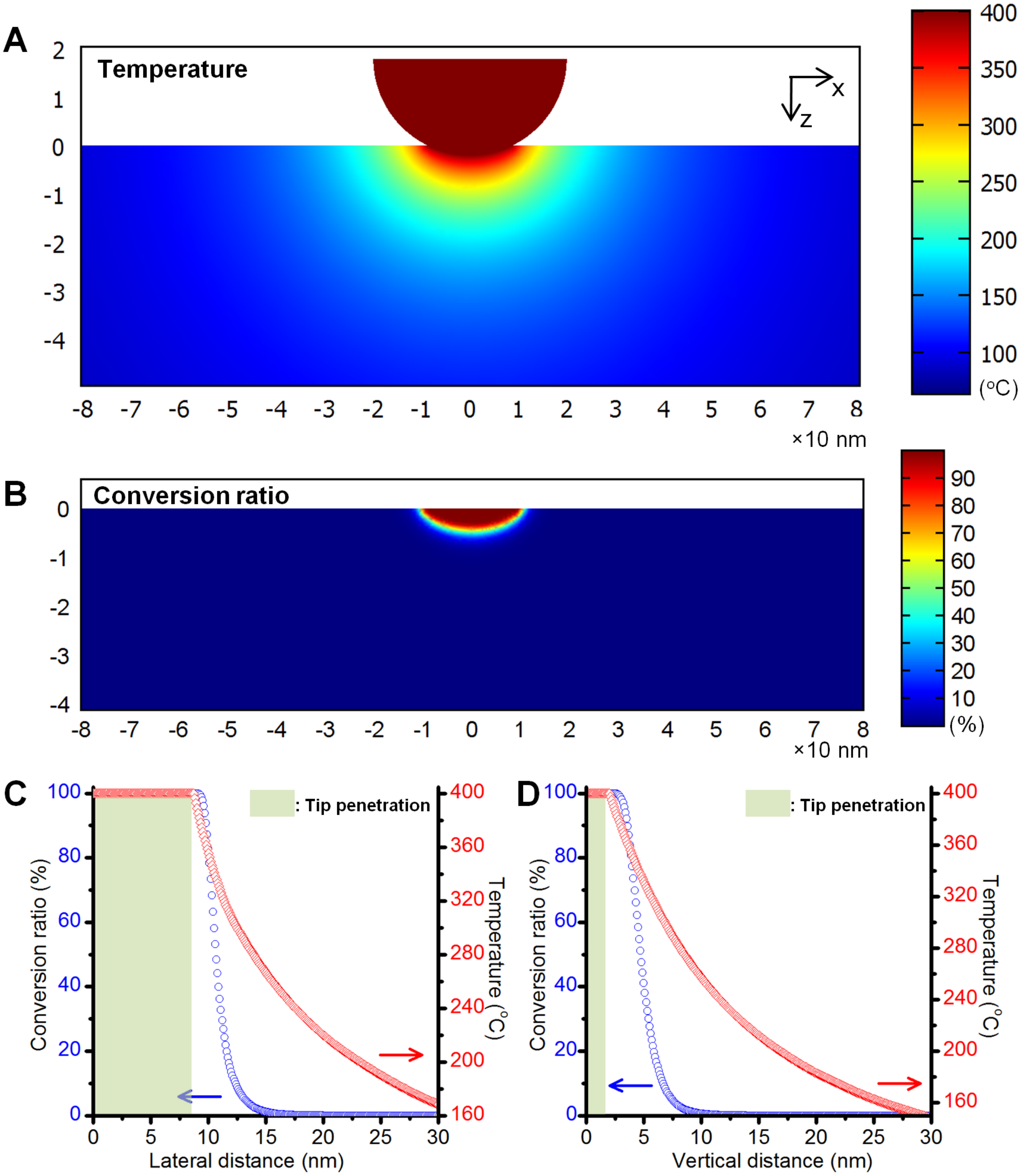

**Figure 3.4.1:** COMSOL finite element modelling (FEM) of the temperature and amine conversion profile inside a carbamate copolymer. (A) Temperature profile. (B) Carbamate to amine conversion ratio profile. (C) Temperature and conversion ratio profile along lateral direction ($z = 0$). (D) Temperature and conversion ratio profile along vertical direction ($x = 0$)

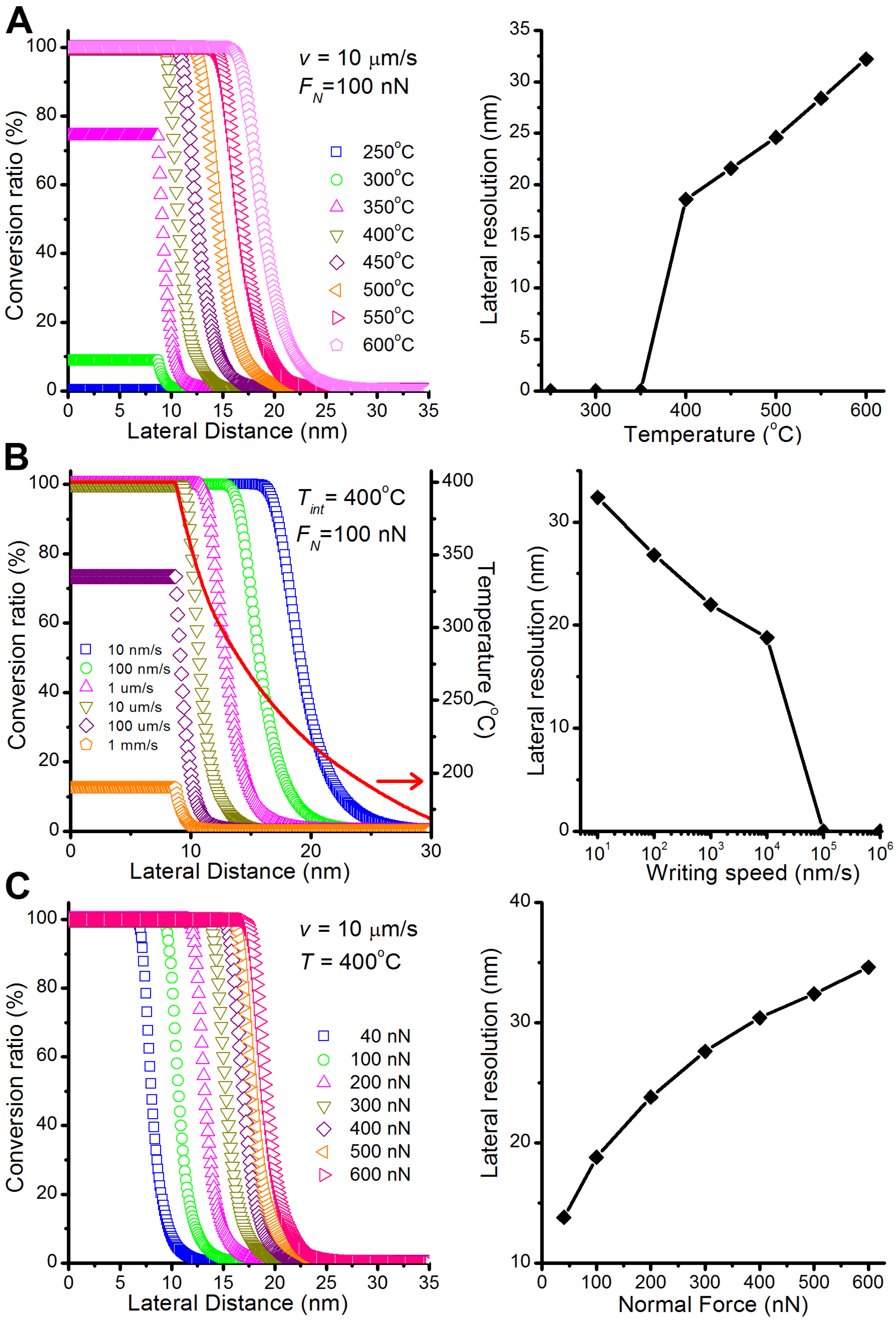

**Figure 3.4.2:** COMSOL FEM simulation of TCNL spatial resolution. Temperature dependence $T_{int}$, writing speed dependence ($v$), and normal loading force dependence ($F_N$) are plotted in (A), (B), and (C) respectively.

# CHAPTER IV

# RESULTS AND DISCUSSION

## *4.1 Local Wettability Modification of Polymer Surfaces*

### 4.1.1 Motivation

In the past decade, the need to introduce local chemical modifications on a variety of substrates, particularly useful for the immobilization of biomolecules, has motivated the development of new scanning probe-based nano patterning techniques [129, 130]. Dip-pen nanolithography enabled the deposition of a wide variety of inorganic, organic and biological inks with a resolution of tens of nm [38] and an overwriting capability [58]. However, only some substrates are suitable for this technique and the overwriting process requires a probe change and the use of elaborate alignment marks. Combined write-read-erase-rewrite or write-read-overwrite capabilities are not only important for data storage applications, they also give the flexibility required by complex multiple-step manufacturing processes. Previous attempts to develop these rewriting/overwriting capabilities relied on reversible light-induced chemical reactions [131], oxidation/reduction reaction [132], and electrochemical deposition/removal of metallic particles [133]. Each of these methods has its disadvantages, such as the low resolution, the slow writing speed, the need for a conductive substrate and the lack of control over the water meniscus in electrochemical processes.

### 4.1.2 Write-read-overwrite capability

The p(THP-MA)$_{80}$p(PMC-MA)$_{20}$ copolymer surface was first heated to 70 ± 20 °C, below the THP deprotection temperature, by means of a thermal cantilever [110]. No change in topography or friction was detected on the heated area (Fig. 4.1.2, region I). After heating a 1.5 $\mu$m × 1.5 $\mu$m square to 110 ± 20 °C a corresponding pattern in the friction image is observed (Fig. 4.1.2, region II). The topography shows no depletion inside the square. The friction increase in the written pattern suggests that the THP groups were deprotected, leaving the area covered with hydrophilic carboxylic acid groups. A second smaller 0.65 $\mu$m × 0.4 $\mu$m square pattern (Fig. 4.1.2, region III) was overwritten inside the hydrophilic pattern (region II) by further heating to 190 ± 20 °C. The friction image shows that the surface becomes again hydrophobic (lower friction). The corresponding topography depletion is 6 nm deep. This change is consistent with the formation of anhydrides [134].

### 4.1.3 AFM and FTIR characterizations

The FTIR spectrum collected on the non-heated sample (Fig. 4.1.2, left) is characterized by the presence of the carbonyl band corresponding to the stretching vibration of the C=O bond in esters around 1730 $\text{cm}^{-1}$ [135]. The FTIR spectrum of the sample heated to 130 °C shows that the carbonyl band shifts from 1730 $\text{cm}^{-1}$ to 1700 $\text{cm}^{-1}$, consistent with the THP removal and formation of carboxylic acids. The friction force, measured by AFM at a normal load $F_N = 70 \pm 2nN$, increases by 48 ± 7 % upon heating to 135 °C. The friction force increase in the chemically-modified area is consistent with a local change of the wettability, *i.e.* the originally hydrophobic surface becomes hydrophilic (Fig. 4.1.2, right) [136]. This is confirmed by the static water contact angle that decreases from 79 ± 0.2 to 62 ± 1.0 ° as the temperature increases from 70 °C to 135 °C (Figure 3, right) [137]. After further heating above 180 °C, the appearance of two additional peaks at 1760 $\text{cm}^{-1}$ and 1802 $\text{cm}^{-1}$ on the FTIR spectrum confirms the conversion of carboxylic acids into anhydrides (Figure 3, left). This second chemical modification is accompanied by a water contact angle increase to 84 ± 0.7 °. Consistently, the friction force (at $F_N = 70 \pm 2nN$) decreases to a value almost equal to that of the untreated sample. The wettability change introduced by the first chemical modification (THP to carboxylic acid) is fully reversed

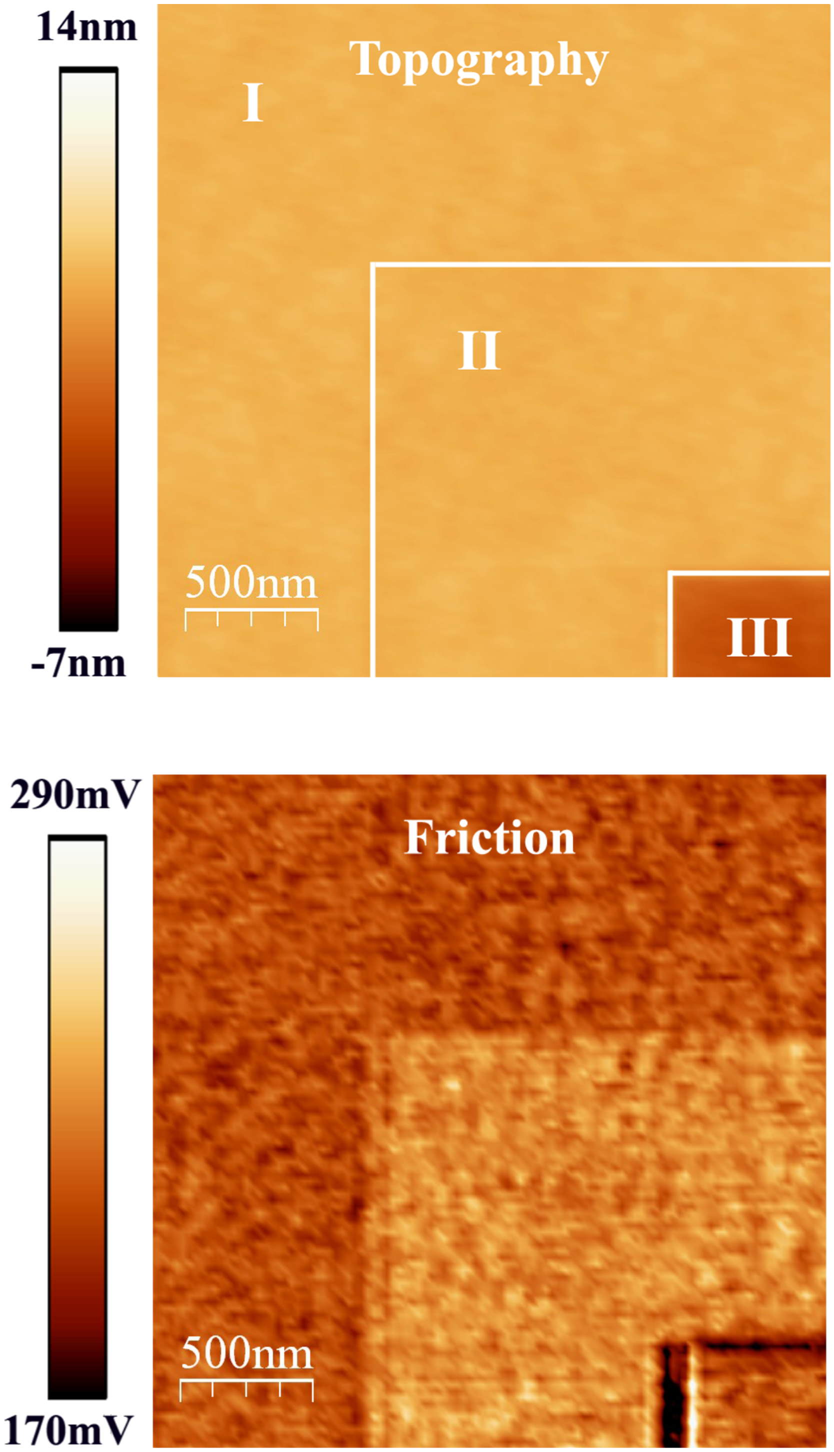
14nm
-7nm
Topography
I
II
III
500nm
290mV
170mV
Friction
500nm

**Figure 4.1.1:** Topography and friction images of a p(THP-MA)$_{80}$ p(PMC-MA)$_{20}$ copolymer surface before (I) and after a first (II) and second (III) TCNL modification. Reprinted with permission from [94]. Copyright 2007, American Institute of Physics.

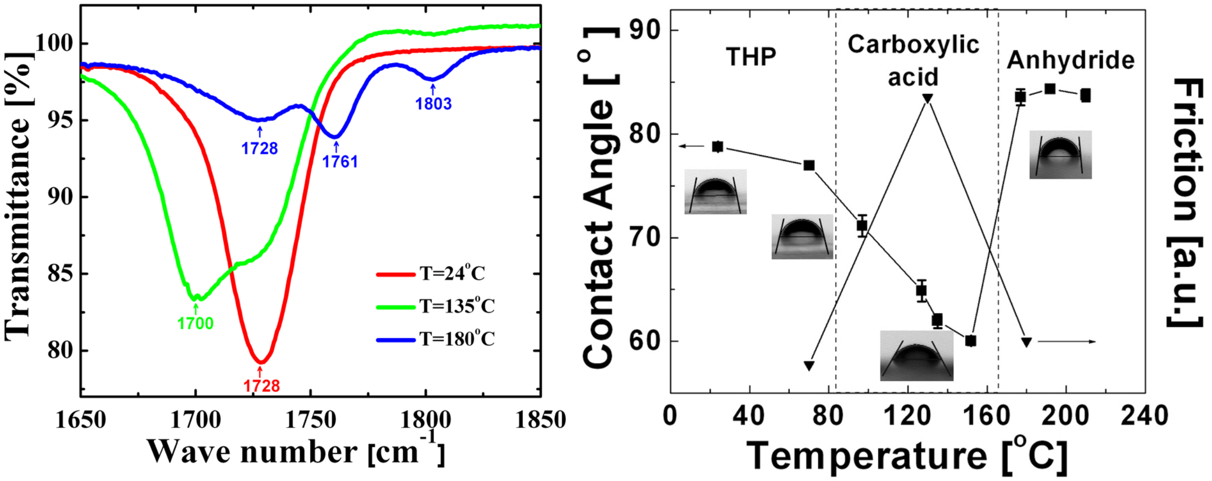

**Figure 4.1.2:** FTIR spectra (left) and static water contact angle vs. friction force measurements (right) of a p(THP-MA)$_{80}$ p(PMC-MA)$_{20}$ copolymer upon heating to selected temperatures. Reprinted with permission from [94]. Copyright 2007, American Institute of Physics.

by the second chemical modification (carboxylic acid to anhydride).

## *4.2 Multifunctional Nano-Templates for Assembling Nano-Objects*

### 4.2.1 Motivation

At the forefront of nanobiotechnology and nanoscience is the challenge to manipulate and control the surface positioning of individual proteins, nanoparticles, and other complex nanostructures [138, 136, 139, 140, 141, 142, 143, 144]. Achieving this aim would greatly facilitate the development of protein chips with single-molecule detection capability, nanoelectronics devices, and fundamental studies of complex cell-cell and cell-matrix interactions, such as the formation of immunological synapses and focal contacts. Numerous approaches have been proposed to assemble molecules on surfaces with nanometer scale resolution, including photolithography [145], electron beam lithography [146], micro-contact printing [147], self-assembly [148], and several scanning probe microscopy based lithography methods, such as dip-pen nanolithography [149], nanografting [150, 42], nanoshaving [151], nanopippetting [152], and scanning near-field optical microscopy lithography [153].

While significant advances have been made in the nanopatterning of some inorganic nano-objects, challenges still exist in particular for protein and DNA nanolithography [154, 60, 155, 156, 157, 57]. The main goals are obtaining a resolution below fifty nanometers, achieving high writing speeds [139], reducing costs, producing multiple functionalities coexisting on a single surface [152, 158], preserving biological functionality [158], and finding a robust and accessible technique that is compatible with a variety of substrates. Bioactivity is a particularly delicate problem because denaturation, oxidation, and dehydration in air are common drawbacks that complicate many potential protein nanopatterning techniques. It also limits the choice of surfaces. For example, proteins directly chemisorbed onto gold tend to denature.

Most protein nanopatterning techniques are incapable of making features below 100 nm and only a few have been established for independently patterning multiple protein species on the same surface [152, 57, 158]. Self-assembly techniques have achieved nanometer scale patterning of proteins [159] but with the disadvantage that the proteins are arranged in fixed regular arrays rather than in tailor-made patterns. Recently, a new solution-based technique was introduced that uses a vibrating AFM cantilever to mechanically displace proteins from a protein monolayer, so that a different protein type fills the gap to create a desired pattern [158]. With this approach, bioactive proteins have been patterned with features as small as 50 nm; however, these patterns are embedded in a self-assembled monolayer of other proteins and an AFM is required during protein patterning.

### 4.2.2 Multifunctional nanopatterns

TCNL can create multi-functional nanopatterns coexisting on the same surface, which later can be selectively functionalized with the desired species of nano-objects. The approach is conceptually simple, as outlined in Fig. 4.2.1 After using TCNL to write the first of the desired amine patterns, the deprotected amines can be thiolated via a reaction with N-succinimidyl 3-(2-pyridyldithio)propionate (SPDP) (triangles). A second TCNL pattern can then be created on a different area of the same polymer surface (diamonds), exposing additional amines in a new region. The di-thiols obtained after the first patterning step are then reduced to thiols using dithiothreitol (DTT) [160], thereby producing a surface with tailored patterns of amine and thiol groups.

TCNL can create multi-functional nanopatterns coexisting on the same surface, which later can be selectively functionalized with the desired species of nano-objects. The approach is conceptually simple, as outlined in Fig. 4.2.1 After using TCNL to write the first of the desired amine patterns, the deprotected amines can be thiolated via a reaction with N-succinimidyl 3-(2-pyridyldithio)propionate (SPDP) (triangles). A second TCNL pattern can then be created on a different area of the same polymer surface (diamonds), exposing additional amines in a new region. The di-thiols obtained after the first patterning step are then reduced to thiols using dithiothreitol (DTT) [160], thereby producing a surface with tailored patterns of amine and thiol groups.

Alternately, we can transform the amine pattern from the second application of TCNL, using N-hydroxysuccinimide (NHS)-biotin, thus modifying the amine functionality to biotin functionality. At this stage, reduction with DTT can create a co-patterned surface of thiols and biotins. In order to nanopattern surfaces with three different functionalities (Fig. 4.2.1), a third application of TCNL produces a triple-patterned surface consisting of thiols, biotins, and amines.

Once the surfaces have been patterned with the desired chemical groups, they can be stored in a desiccator for later functionalization with proteins or other nano-objects. Thus far, we have stored the nanopatterned surfaces for a maximum duration of three weeks before successful two-protein functionalization. In future studies we

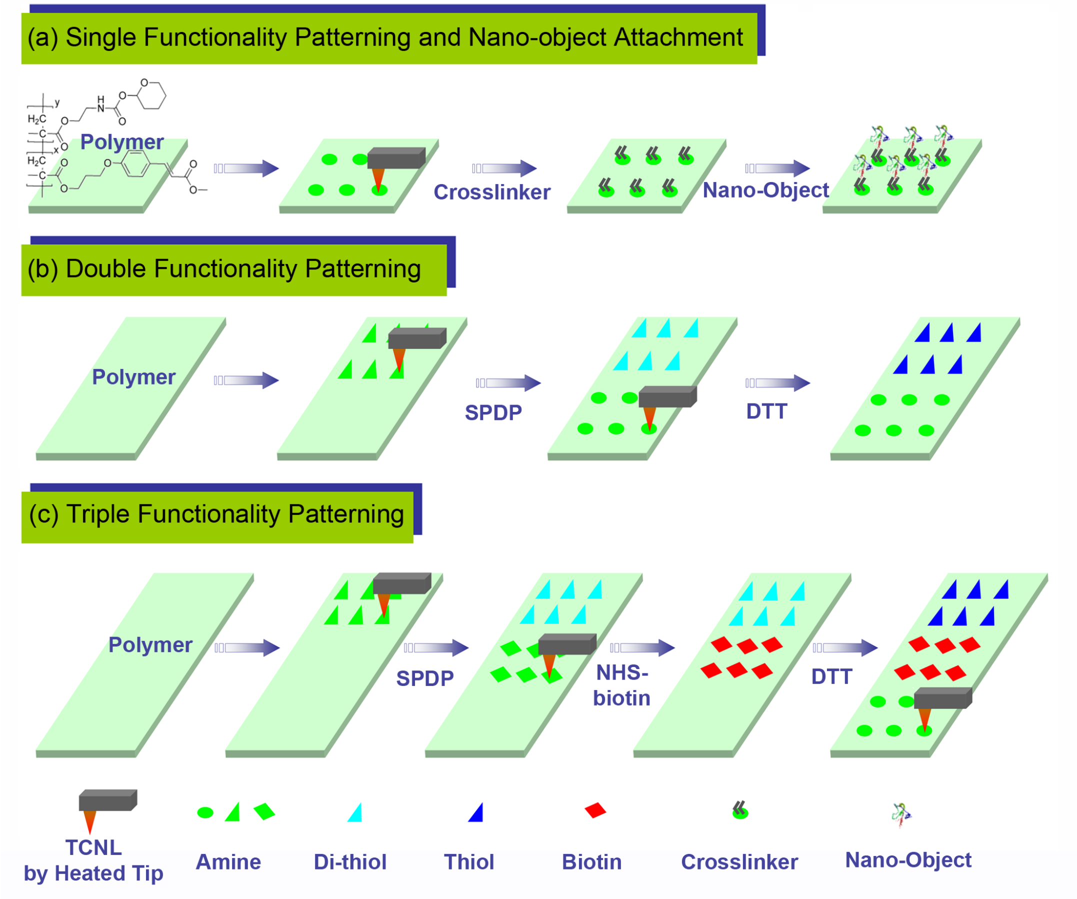
(a) Single Functionality Patterning and Nano-object Attachment
Polymer
Crosslinker
Nano-Object
(b) Double Functionality Patterning
Polymer
SPDP
DTT
(c) Triple Functionality Patterning
Polymer
SPDP
NHS-biotin
DTT
TCNL by Heated Tip
Amine
Di-thiol
Thiol
Biotin
Crosslinker
Nano-Object

**Figure 4.2.1:** Scheme of multifunctional templates by TCNL.(a) A single nano-object pattern is created through three steps: TCNL, crosslinker incubation and nano-object incubation. (b) A double functionality pattern of thiols (blue triangles) and amines (green disks) is created through two rounds of TCNL and incubation processes. (c) A triple functionality pattern of thiols (blue triangles), biotins (red diamonds), and amines (green disks) is created through three rounds of TCNL and incubation processes [79]. Copyright Wiley-VCH Verlag GmbH & Co. KGaA. Reproduced with permission.

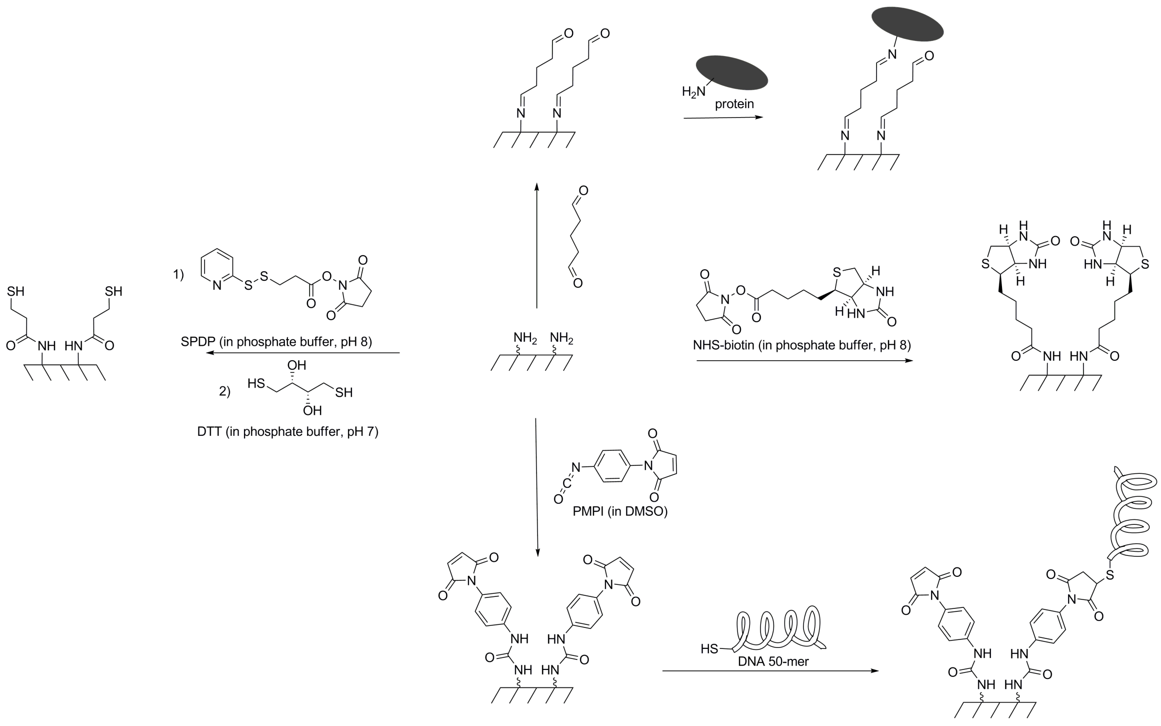
H2N
protein
1)
SPDP (in phosphate buffer, pH 8)
2)
DTT (in phosphate buffer, pH 7)
NH2 NH2
NHS-biotin (in phosphate buffer, pH 8)
PMPI (in DMSO)
HS
DNA 50-mer

**Figure 4.2.2:** A flowchart to show how the unmasked amine nanotemplates are selectively and covalently functionalized to create patterns of thiols, maleimides, aldehydes or biotins in distinct areas of the polymer surface [79]. Copyright Wiley-VCH Verlag GmbH & Co. KGaA. Reproduced with permission.

will investigate longer storage times.

Several approaches provide evidence that reactive amines are created by local thermal deprotection. A first confirmation of a chemical change by TCNL is obtained in-situ by friction force microscopy [78, 94], indicating a regular increase in friction in the areas heated by the tip. This friction increase is consistent with a decrease of the water contact angle (larger hydrophilicity) when the copolymer film is bulk heated above $T_d$ [155]. No chemical transformation is observed if the tip temperature during patterning was below $T_d$. Direct confirmation of the chemical viability of our surfaces is shown in Fig. 4.2.3. Using several amine crosslinking strategies, we demonstrated that TCNL patterns can be functionalized with small molecules, proteins, or other nano-objects that can selectively interact with the underlying amine pattern, but not with the unmodified polymer. Specifically, part a of Fig. 4.2.3 shows the binding of different fluorescently-labeled proteins to the TCNL amine patterns via two different crosslinking mechanisms, NHS-biotin and glutaraldehyde (GA). The fluorescent patterns of single protein species show bound streptavidin, anti-CD3, and fibronectin. The amine patterns for streptavidin and fibronectin conjugation were made by heating the thermal AFM tip at 230 °C ± 20 °C with a normal load of 210 nN at a linear writing speed of 100 $\mu$m s$^{-1}$; the amine pattern for antiCD3 conjugation was made at 200 ℃ ± 20 ℃ with a normal load of 500 nN at a linear writing speed of 100 $\mu$m s$^{-1}$. Images produced using epifluorescence microscopy verified that fluorescent patterns are consistent with the patterns written by TCNL and with the post-patterning functionalization utilized. Fluorescence imaging was performed using epifluorescence microscopy on an inverted Nikon TE2000 microscope equipped with a Nikon Intensilight (C-HGFIE) for illumination and a Nikon EM-CCD camera (DQC-FS). Images were obtained using a Plan Apo 60x water immersion objective (Nikon, NA 1.2) or a Plan Apo 100X oil immersion objective (Nikon, NA 1.4). Nikon filter cube sets were used to image fluorescent dyes in the region of UV (#96310, UV-2EC DAPI filter set, excitation 340-380 nm, dichroic mirror DM400, emission 435-485 nm), in the green (#96320, FITC/GFP HyQ filter set, excitation 460-500 nm, dichroic mirror DM505, emission 510-560 nm), and in the red (#96324, Cy5 HQ filter set, excitation 620-660 nm, dichroic mirror DM Q660LP, emission 700-775 nm).

In order to provide a simple demonstration of the generality of the approach, part b of Fig. 4.2.3 shows AFM images of a TCNL generated triangular amine pattern that has been functionalized with 50-mer single-stranded (ss) DNA. The surface amines were converted to maleimides (via N-(p-maleimidophenyl)isocyanate, PMPI, in dimethylsulfoxide) and then crosslinked to thiol-terminated DNA strands. The triangle amine pattern was made by heating the thermal AFM tip at 180 °C ± 20 °C with a normal load of 250 nN at a linear writing speed of 100 $\mu$m s$^{-1}$. The AFM topography and phase images (recorded simultaneously at a raster scan speed of 140

$\mu$m s$^{-1}$) of the patterns before and after DNA functionalization are consistent with the binding of DNA in the TCNL activated triangular area. The observed height contrast of about 5 nm is also consistent with previous work on DNA patterning where, for 37-mer ssDNA, the patterns showed height contrast of about 4 nm [161]. We note that for this particular triangular pattern the depletion height in the active area (excluding the edges) written by TCNL before DNA functionalization is about 1 nm.

The viability of multi-functional patterns was then verified using the approach described in Fig. 4.2.1. A co-pattern of thiols and biotins was fluorescently labeled by incubation of the surface first with the blue fluorescent dye N-(7-dimethylamino-4-methylcoumarin-3-yl) maleimide (DACM) and then the red-emitting Cy5-streptavidin, in order to determine if they would selectively bind to the thiol and biotin patterns, respectively [60]. Part c of Fig. 4.2.3 shows the resultant fluorescent patterns of thiols (blue triangles) and biotins (red diamonds). The triangular amine pattern was made by heating the thermal AFM tip at 190 °C ± 20 °C with a normal load of 210 nN; the diamond amine pattern was made by heating at 210 °C ± 20 °C with a normal load of 210 nN at a linear writing speed of 200 $\mu$m s$^{-1}$. The two fluorophores were imaged separately on a monochrome camera using a DAPI filter set for the DACM and a Cy5 filter set for the Cy5-streptavidin. The third combined image represents the overlay of the two independently acquired images. Little crosstalk was observed between the two channels, demonstrating both the effective localization of the dyes onto the TCNL pattern and the specificity of their chemical crosslinking to the surface.

### 4.2.3 Protein Nano-arrays

TCNL is capable of extremely high resolution chemical patterning of surfaces due to the high temperature gradients in the vicinity of the heated tip [78]. Therefore, we investigated our ability to organize small amounts of proteins with high definition.

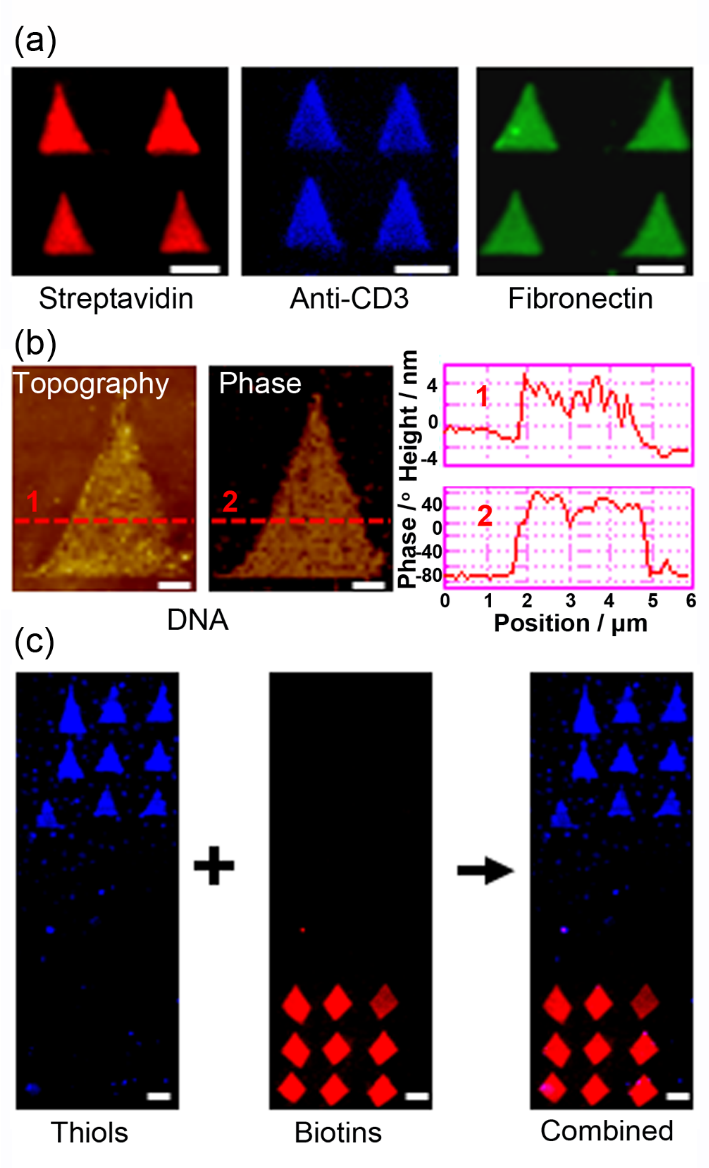
(a)
Streptavidin
Anti-CD3
Fibronectin
(b)
Topography
Phase
1
2
DNA
Height / nm
4
0
-4
Phase / °
40
0
-40
-80
0
1
2
3
4
5
6
Position / μm
(c)
Thiols
Biotins
Combined

**Figure 4.2.3:** Single and multi-component micro-patterns. (a) Epifluorescence images of micro triangle patterns of Cy5-streptavidin (red) (crosslinked to amine via NHS-biotin), biotinylated Alexa350-antiCD3 (blue) (crosslinked to NHS-biotinylated amine with streptavidin), and atto488 fibronectin (green) (crosslinked to amine with GA). (b) AFM topography and phase images of a triangular pattern of thiol-terminated DNA single strands crosslinked to amines through PMPI. (c) Epifluorescence images of DACM and Cy5-streptavidin orthogonal functionality patterns on the same surface. Blue DACM was crosslinked to amine-terminated triangles by means of SPDP-DTT thiolation, while red Cy5-streptavidin was crosslinked to amine-terminated diamonds by means of NHS-biotin [79]. Scale bars: (a) 5 $\mu$m, (b) 1 $\mu$m, (c) 10 $\mu$m. Copyright Wiley-VCH Verlag GmbH & Co. KGaA. Reproduced with permission.

Using a single touchdown approach at each feature, we produced an array of 500 nm features decorated with fluorescently-labeled fibronectin, as shown in Fig. 4.2.4. Each dot in the amine array pattern was made by approaching the heated AFM tip (220 °C ± 20 °C) to the polymer surface from a height of 0.8 $\mu$m at a speed of 120 $\mu$m s$^{-1}$. The heated tip was kept in contact with the surface at a normal load of 210 nN for 5 seconds and then withdrawn at a speed of 120 $\mu$m s$^{-1}$. The size of a single feature is inferred from AFM imaging of the protein pattern.

To investigate length scales below the resolution limit of optical microscopy, we thus employed topographical and phase AFM imaging in ambient conditions. Using again a single touchdown approach at each feature but with a shorter dwell time, TCNL was used to de-protect amines in even smaller areas. Three such features are shown in Fig. 4.2.5 as topographical and phase images. Each dot in the amine array pattern was made by approaching the heated AFM tip (200 °C ± 20 °C) to the polymer surface from a height of 0.8 $\mu$m at a speed of 120 $\mu$ms$^{-1}$. The heated tip was kept in contact with the surface at a normal load of ~100 nN for 0.5 seconds and then withdrawn at a speed of 120 $\mu$m s$^{-1}$. AFM phase images taken after fibronectin or GA staining (recorded at a linear raster scan speed of 36 $\mu$m s$^{-1}$in ambient conditions) provide information on the local viscoelasticity of the sample. A larger phase change is indicative of a softer surface, which is what we expect in the patterns decorated with proteins. The topography indicates a shallow indentation of approximately 10 nm. This depth can be made larger or smaller by varying the tip temperature, load and dwell time [78, 162]. The surface was then functionalized with fibronectin (part a of Fig. 4.2.5) or with streptavidin (part b of Fig. 4.2.5). The topographical data revealed that the TCNL holes were filled with proteins. The phase images are also consistent with the deposition of proteins in the holes. Fibronectin phase features as small as 40 nm and streptavidin as small as 60 nm have been measured. The former value compares well with previous measurements of single dry fibronectin

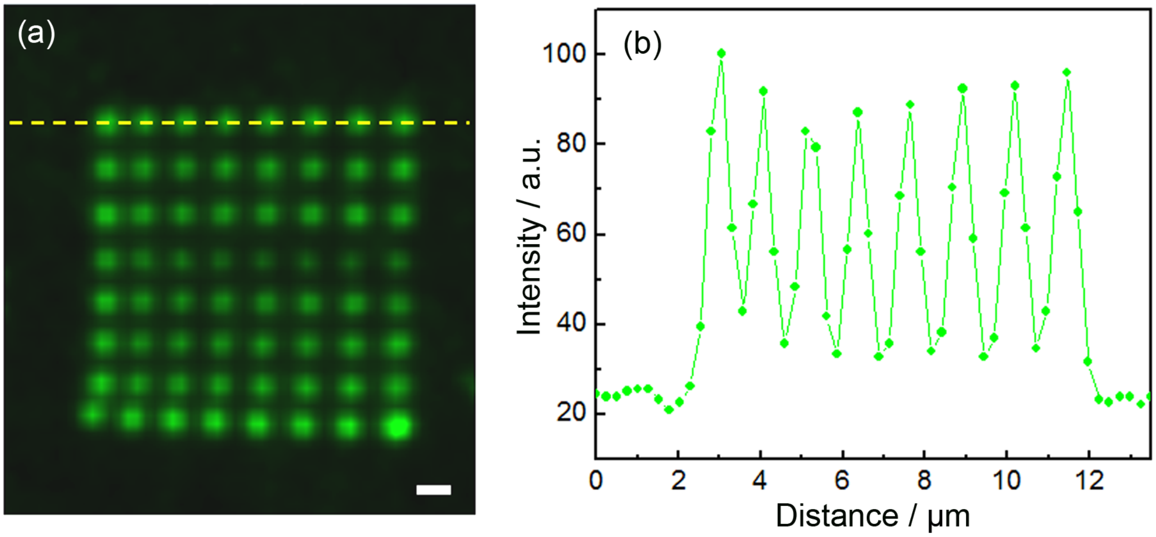

**Figure 4.2.4:** 500 nm fibronectin nanoarray. Epifluorescence image of a regular array of Atto488 fibronectin patches (a) and cross section profile (b). A linear interpolation (solid line) has been used to interpolate the fluorescence data points (dots) obtained by optical microscopy. Fibronectin was crosslinked to amine groups by means of GA. It should be mentioned that the radius of the features is comparable in size with the resolution of the optical image (~0.61 $\lambda$/NA, where $\lambda$ is the wavelength used and NA is the numerical aperture of the objective), so other techniques should be used to determine the distribution of proteins within each feature [79]. Scale bar: 1 $\mu$m. Copyright Wiley-VCH Verlag GmbH & Co. KGaA. Reproduced with permission.

molecules [163]. Comparing the topographical image of the active sites before and after fibronectin functionalization and considering the geometrical convolution with a spherical AFM tip (radius about 15 nm), we conclude that roughly 1-2 fibronectin molecules are exposed at the surface, whereas more fibronectins could fit inside the hole created during TCNL writing. We cannot give more detailed information on the exact numbers of proteins per spot because we do not know the conformation of the proteins inside the holes.

While here we have demonstrated the technique by using glass substrates, since the polymer can planarize a substrate, the technique could be applicable to any oxide film to which the polymer can be crosslinked. Furthermore, it is significant to note that the surfaces can be pre-patterned and stored for later bio/nano functionalization (at least weeks later). Thus, the multi-protein/nano-object patterning can

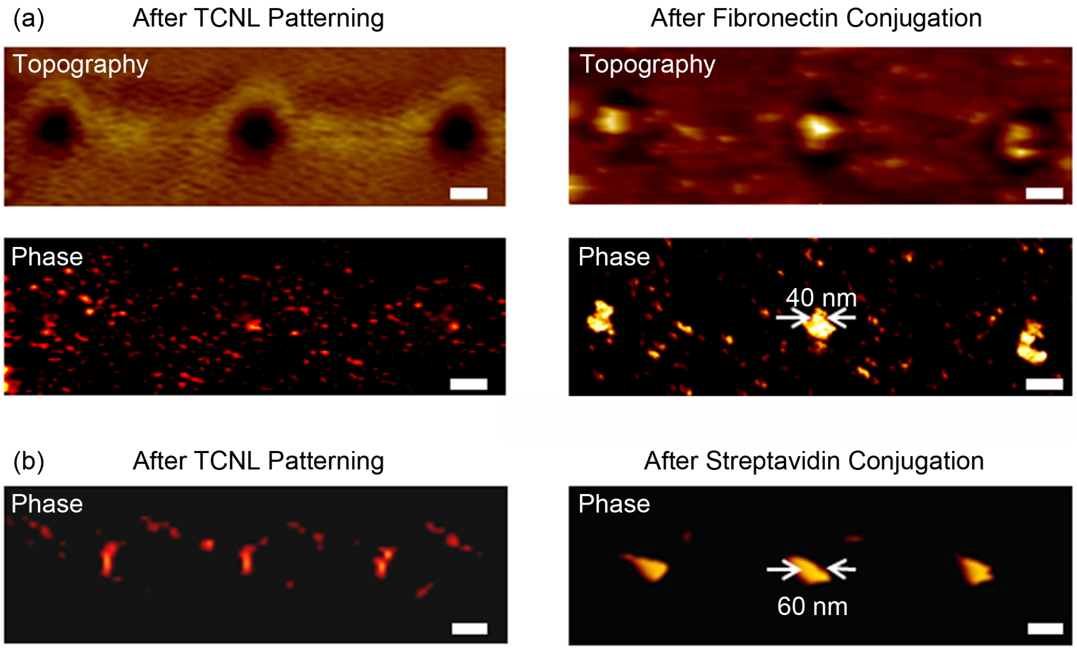
(a)
After TCNL Patterning
After Fibronectin Conjugation
Topography
Topography
Phase
Phase
40 nm
(b)
After TCNL Patterning
After Streptavidin Conjugation
Phase
Phase
60 nm

**Figure 4.2.5:** Fibronectin and streptavidin nanoarrays. AFM topography and phase images of a TCNL nanoarray before and after fibronectin (a) and streptavidin (b) attachment. The topography z-range in (a) is 20 nm [79]. Scale bars: 100 nm. Copyright Wiley-VCH Verlag GmbH & Co. KGaA. Reproduced with permission.

take place under native conditions in a second laboratory without the TCNL equipment or expertise in nanolithography. These features were deliberately built into our protocol to increase the accessibility of the technique to a variety of researchers not only interested in nanolithography, but in areas of biochemistry, nanoscience and nanobiotechnology more broadly. We foresee that the TCNL/CF/MR has a direct impact on the development of nano-devices, biosensors, and on many cell studies that require interaction with two or more proteins in tailor-made patterns.

## *4.3 Nanopatterning of Organic Semiconductors*

### 4.3.1 Motivation

Conjugated polymers have been recognized as promising candidates to replace conventional inorganic semiconductor materials in certain electronic and optoelectronic applications [81]. These polymers show many useful optoelectronic properties, such as electroluminescence [80], high charge carrier mobilities [164], and photovoltaic effect [165]. Nano-patterning and nano-fabrication of conjugated polymers on various length scales have attracted considerable interest for nanoelectronics, nanophotonics, and biosensing. Among the methods that have been reported to date for the patterning of conjugated polymers are electrodeposition [166], electrospinning [167], inkjet printing [168], nanoimprint lithography [169], dip-pen nanolithography through electrostatic interaction or electrochemical reaction [170, 171], scanning near-field optical lithography [53, 55], thermochemical Nanopatterning [128], and edge lithography [172].

### 4.3.2 Direct writing of conjugate polymer nanostructures

The direct writing of nanostructures of poly(p-phenylene vinylene) (PPV), a widely studied electroluminescent conjugated polymer, by nanoscale heating a sulfonium salt precursor, poly(p-xylene tetrahydrothiophenium chloride) is realized by locally heating in ambient conditions with a resistively heated AFM cantilever at 240 °C [173]. The precursor thin film is obtained by drop-casting precursor solution on a glass or silicon (111) substrate.

### 4.3.3 Raman and fluorescence characterizations

Fluorescence imaging is a convenient method to follow the thermal conversion of a precursor to PPV because of its broad emissive photoluminescence spectrum in the green color region. PPV nanostructures were imaged using fluorescence microscopy with an inverted Nikon TE2000 equipped with a high-sensitivity CCD camera (CoolSNAP HQ2, Roper Scientific). Images were obtained using a Plan Apo 60X water immersion objective (Nikon, NA 1.2). A Nikon filter cube set was used to image fluorescent PPV nanostructures in the green region (#96320, FITC/GFP HyQ filter set, excitation 460-500 nm, dichroic mirror DM505, and emission 510-560 nm). All the Raman data of the present work were obtained from a confocal Raman microscope

(Jobin Yvon HR800) using a laser excitation wavelength of 785 nm with the same acquisition time.

Figure 4.3.1 shows fluorescence and AFM topography images of the PPV lines made by TCNL. These nanostructures were made at a writing speed of 20 $\mu$m s$^{-1}$, with a normal load of 30 nN, and cantilever temperature ranging between 240 °C and 360 °C. The nanostructures started to show a visible fluorescent contrast at 240 °C. The contrast became clearer as the heating temperature was raised to 360 °C. The corresponding AFM topography image reveals TCNL capability of fabricating PPV nanostructures with a high spatial resolution of 70 nm.

Raman spectroscopy measurements provided more definitive evidence of the thermal conversion and highlighted the quality of the TCNL prepared nanostructures. We produced 20 $\mu$m × 20 $\mu$m TCNL patterns at 240 °C, 280 °C, and 320 °C, with a normal load of 30 nN and a speed of 20 $\mu$m s$^{-1}$. Raman measurements revealed that the quality of the PPV patterns formed by TCNL in ambient conditions is comparable to the quality of a PPV sample prepared by a standard thermal annealing of a precursor polymer in vacuum conditions, here referred to PPV$_{reference}$ [174]. As shown in Fig. 4.3.2,Raman spectra were obtained from four representative samples: an untreated precursor film, a precursor film bulk heated with a hot plate under ambient conditions at 280 °C for about an hour, a TCNL pattern, and a PPV$_{reference}$ film. The four samples were obtained from the same precursor polymer batch and had a thickness of 1.4 m. The PPV$_{reference}$ film was prepared by annealing the precursor film for five hours at 280 °C in a vacuum of ∼200 mTorr. The most distinctive characteristics of the Raman spectra after the complete conversion of the precursor film into PPV is the large intensity enhancement, which we attribute to a density increase in the polymer film due to a volume contraction. The Raman spectrum of the TCNL pattern clearly shows the same enhancement in intensity throughout the spectrum. In the case of an ambient bulk heated precursor polymer, we observe a

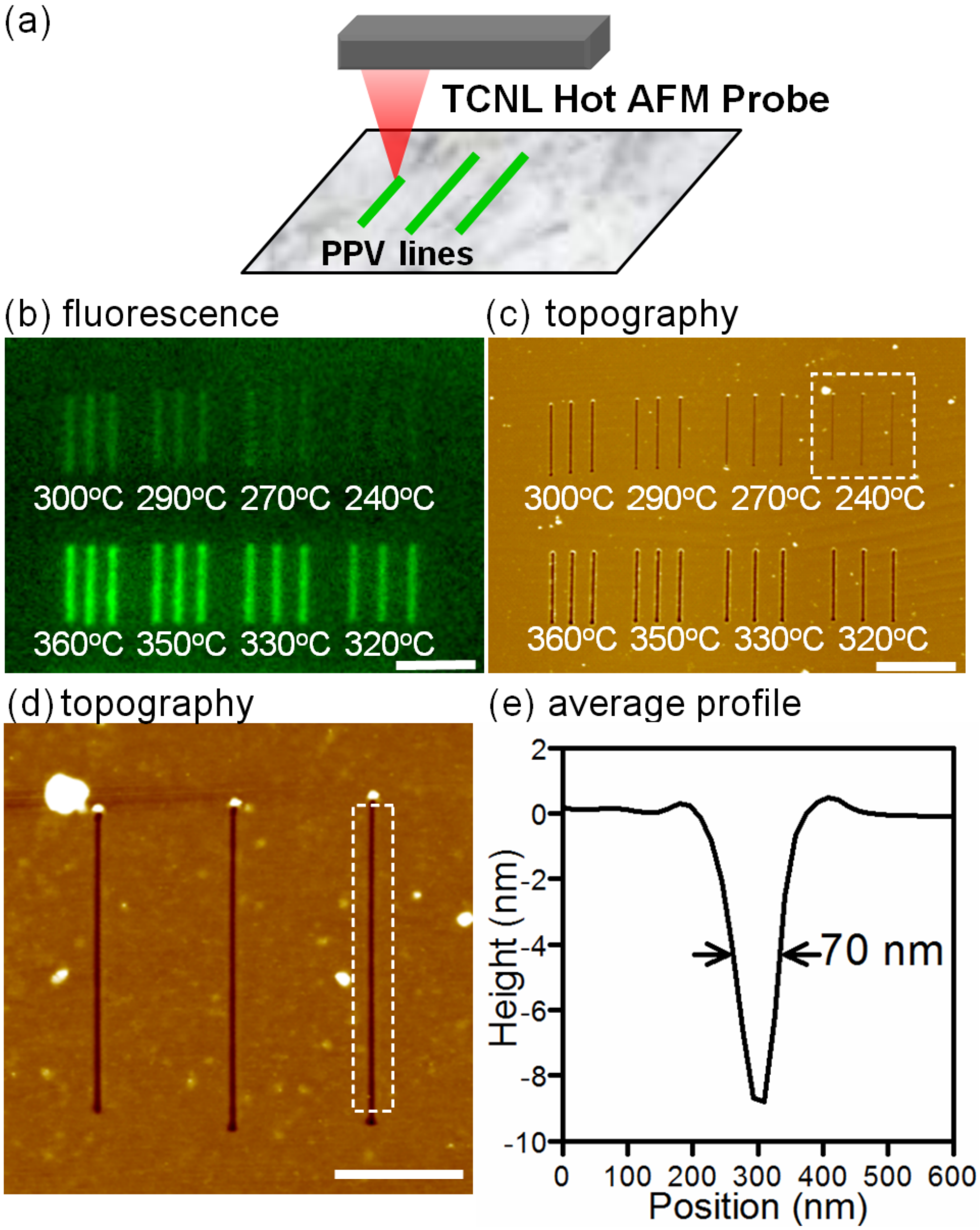

**Figure 4.3.1:** TCNL nanolithography of PPV nanostructures. (a) Scheme of TCNL nanolithography of PPV nanostructures. (b) Fluorescence and (c) AFM topography images of PPV nanostructures made by TCNL at a range of temperatures, 240 °C-360 °C. A zoom-in view of PPV lines made at 240 °C as outlined in (c) is shown in (d). (e) The average profile of the PPV trench outlined in (d) shows that the width (FWHM) of the line is as narrow as 70 nm. The thickness of this precursor film is 100 nm. Scale bars: (b) and (c): 5 $\mu$m, (d): 2 $\mu$m. Reprinted with permission from [173]. Copyright 2009, American Institute of Physics.

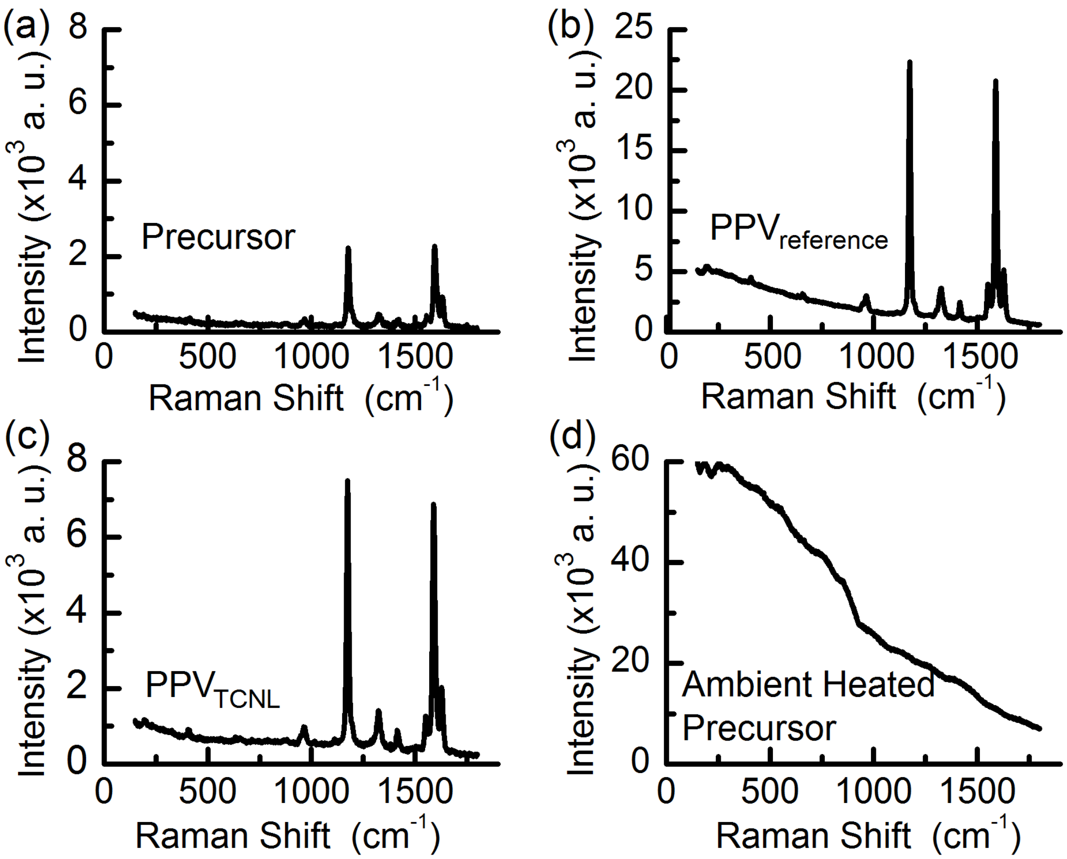

**Figure 4.3.2:** Raman spectra of (a) untreated precursor, (b) PPV reference, (c) TCNL PPV pattern, and (d) precursor annealed in ambient condition. Reprinted with permission from [173]. Copyright 2009, American Institute of Physics.

large continuum background very likely generated by oxidation and the disappearance of the PPV Raman peaks.

Another signature of the precursor-PPV conversion is the shift in frequency of the Raman peaks associated with the C-C vibrations to lower frequencies. With respect to the PPV$_{reference}$, the two Raman peaks of the untreated precursor polymer at around 1178 cm$^{-1}$ and 1594 cm$^{-1}$ are found to shift by 3 cm$^{-1}$ and 6 cm$^{-1}$, respectively, after the conversion as depicted in Fig. 3(a). The Raman peak positions of the TCNL patterns written at three different tip temperatures are in between those of the precursor polymer and those of the PPV$_{reference}$ polymer. As the tip temperature used to perform TCNL increases, the Raman intensity of the written patterns increases and the peak positions shift to those of the PPV$_{reference}$ film.

In order to obtain more quantitative information on the quality and degree of thermochemical conversion, we modeled the TCNL modified film as composed of $\alpha\%$ of precursor polymer and $(100-\alpha)\%$ of PPV$_{reference}$. The Raman spectrum of the composite system may thus be a linear superposition of the spectra of the two constituents, namely precursor and PPV$_{reference}$ (reported in Fig. 4.3.2), as estimated by the following relationship:

$$I_{PPV_{TCNL}}^{Model} = \frac{\alpha}{100}\left(I_{precursor} - I_{substrate}\right) + \left(1 - \frac{\alpha}{100}\right)\left(I_{PPVreference} - I_{substrate}\right). \tag{4.3.1}$$

Figure 4.3.3 illustrates the major differences between the Raman spectra obtained from the TCNL pattern produced at 300 °C ($I_{PPV_{TCNL}}^{Experimental}$) and $I_{PPV_{TCNL}}^{Model}$ derived from Equation (4.3.1). The free fitting parameter $\alpha$ was found by fitting $I_{PPV_{TCNL}}^{Model}$ to $I_{PPV_{TCNL}}^{Experimental}$ in the range 1500 cm$^{-1}$- 1800 cm$^{-1}$. This spectral region is far off the background signal caused by oxidation. With the blending ratio of 27% PPV$_{reference}$ and 73% precursor, the peak frequencies and intensity of $I_{PPV_{TCNL}}^{Model}$ are found to be perfectly overlapping in both intensity and peak-positions with $I_{PPV_{TCNL}}^{Experimental}$ in the considered frequency range. However, the broad background signal persistent at the head side is very different in the two cases. We speculate that this persistent difference could arise from partial oxidation of the PPV$_{reference}$ sample. In comparison with PPV$_{reference}$, the TCNL samples show a smaller background intensity at low frequencies, which suggests that the TCNL method may produce higher quality PPV samples. We attribute this improvement to the TCNL-specific geometry in which the temperature is increased locally at the tip-surface "sealed" contact. By using the above found parameter $\alpha = 73\%$, we can estimate that out of the 1.4 $\mu$m thick precursor film, a precursor thickness of around 320 nm has been converted to the reference grade of PPV in a single application of TCNL at 320 °C. This thickness can be controlled by changing the tip temperature and contact time, which is an advantage of the TCNL process.

## *4.4 Nanoscale Tunable Reduction of Graphene Oxide*

### 4.4.1 Motivation

Graphene's high electronic mobility [175, 176, 177, 82], gating capability [178, 151, 179], and band gap tuning potential [175, 180, 181], have motivated large scale device patterning in epitaxial graphene [182], leading to transistors operating at GHz frequency [183]. Techniques to produce nanometer scale graphene structures include e-beam lithography [175, 178, 184], chemical exfoliation [185], local anodic oxidation lithography [186], and carbon nanotube unzipping [187]. Routine fabrication of graphene-based nanostructures over large areas is challenging in terms of reproducibility, resolution, robustness, edges control, substrate compatibility, and scalability. Recently, reduction of graphene oxide, an insulating material with a transport gap larger than 0.5-0.7 eV at room temperature, has been indicated as a promising route for translating the interesting fundamental properties of graphene into technologically viable devices [85, 188, 189], such as transparent electrodes [189], chemical sensors [190], and MEMS resonators [191]. In particular, transport measurements have shown that GO undergoes an insulator-semiconductor-semimetal transition as it is reduced back to graphene [85, 192].

Here, we show that TCNL is able to directly tune the reduction of GO, and thereby its conductivity, on the nanoscale [193]. The reduced GO nanostructures show an increase in conductivity up to four orders of magnitude as compared to pristine GO. The method is fast (several $\mu$m s$^{-1}$), applies both to conducting and insulating substrates, and is reproducible. GO has been converted to a conductor with a 100% yield in dozens of structures patterned on random locations in the GO film. Reduced GO patterns range from ribbons 12 nm in width (FWHM) up to 20 $\mu$m. No sign of tip wear or sample tearing was observed, indicating that the "carbon skeleton" is continuous across the GO/rGO junction.

### 4.4.2 Nanoscale reduction of graphene oxide with tunable conductivity

The key advantage of TCNL heated cantilever-tip is to localize a nanometer-scale hot spot with a resolution that cannot be achieved by other means. Herein, we demonstrate that TCNL can directly and locally reduce graphene oxide sheets and thereby tune their electronic properties. This thermochemical nanolithography is validated on large area GO films formed by on-chip oxidation of epitaxial graphene ($GO_{epi}$) grown on SiC. The TCNL written nanowires have dimensions as small as 12 nm.

To date, all the GO reduction strategies [85, 194] have led to materials with some residual oxygen and structural defects and so the material is referred to as reduced graphene oxide (rGO) instead of graphene. Chemical reduction has been particularly well studied, and it is known that exposure of GO to strong reducing agents like hydrazine results in an increased electrical conductivity by 3 to 4 orders of magnitude [195]. Recent studies have demonstrated that annealing at 450 °C or above is equivalent to chemical reduction via hydrazine monohydrate at 80 °C followed by heating at 200 °C [194]. Thermal reduction of GO occurs already at moderate temperature (100-250 °C), and enables tuning the gap in graphene oxide [85]. Extensive reduction requires temperatures exceeding 450 °C [194]. In the experiments presented in this report, the nanoscale thermal reduction of GO flakes and $GO_{epi}$ films is achieved by means of a heated atomic force microscopy (AFM) probe [110]. The TCNL reduction of GO is verified here by friction force microscopy (FFM), conductive AFM (CAFM), Raman spectroscopy, Kelvin probe force microscopy (KPFM), and UHV electronic transport measurements using a 4-probe STM. Technological development requires extended films of GO. Large area $GO_{epi}$ films ($> 15$ mm$^2$) are obtained by oxidizing multilayer epitaxial graphene (EG) grown on SiC [74]. We used two types of SiC substrates with different conductivities, 4H-SiC ($10^5$ $\Omega$ $cm^{-1}$) and 6H-SiC ($10^8$ $\Omega$ $cm^{-1}$). The oxidized films consist of multiple high-quality $GO_{epi}$ layers that completely cover the SiC surface. AFM pictures show no tearing in the $GO_{epi}$ films indicating that they maintain their structural integrity when exposed to the harsh oxidation conditions. The $GO_{epi}$ film thickness as measured by AFM by scratching away $GO_{epi}$ was ∼16 nm. This value is in good agreement with the expected thickness for this EG film of 20 layers fully oxidized, considering a thickness ∼0.7 nm per layer for GO [194].

### 4.4.3 CAFM and KPFM characterization

Figure 4.4.1 presents a zigzag rGO nanowire written with a single line scan at $T_{heater}$ ∼1060 °C on $GO_{epi}$. TCNL was performed in ambient conditions. The cantilever was heated while in contact with the GO surface at loading forces ranging between 120 nN - 230 nN. Part A of Fig. 4.4.1 is an image of the current measured between a conductive AFM tip and each point of the surface, showing the expected current enhancement in the $rGO_{epi}$ nanowires. During the CAFM imaging, a -2.5 V DC bias was applied to the sample and a conducting tip (SCM-PIC, Veeco) scanned over the sample in contact mode at a speed of 12 $\mu$m $s^{-1}$, with a normal loading force of 40 nN. The topographical image indicates that the reduction produces a shallow indentation of 10 $\mathring{A}$ whose origin has been previously discussed for the isolated GO sheets.

To carry out KPFM measurement, we used a conducting Pt/Ir coated n-type Si tip (Veeco) with spring constant of 3.0 N $m^{-1}$, resonance frequency of 78 kHz, and a quality factor of ˜ 150. A two-scan lift mode was used to collect the contact potential data. In the first scan, the tip was operated in tapping mode at the cantilever resonance frequency with a mechanical piezo-oscillator to collect the topographical signal. In the second scan, the tip was lifted 20 nm above the sample, and a 6 V peak-to-peak AC voltage was applied to the tip at the cantilever resonance frequency. A lock-in amplifier and a servo feedback unit was used to track the cantilever oscillation at the resonance frequency and record the contact potential [99]. The result in Fig. 4.4.2 shows that the TCNL reduced GO$_{epi}$ displays a contact potential difference of 168 ± 54 mV with respect to GO$_{epi}$. This value is very close to epitaxial graphene EG (290 ± 61 mV).

### 4.4.4 Microscopic four-probe electrical transport measurements

Electrical transport measurements were performed in an UHV Omicron Nanoprobe system ($2 \times 10^{-10}$ mbar) with four independently controlled STM tips and a high resolution SEM which allows nanoscale positioning of the tips. Electrochemically etched tungsten probes (tip diameter $<$ 50 nm [196]) were used for the electrical transport measurements. All current-voltage curves were measured using a Keithley 236 source-measure unit programmed with home built data acquisition software.

The sheet resistance of a sample can be obtained from $I/V$ measurements in a square four-point arrangement. As shown in Fig. 4.4.3, a linear current $I_{1,2}$ was passed between adjacent tips (T1 and T2) and the potential drop $V_{3,4}$ across the opposing tips (T3 and T4) was recorded as a function of $I_{1,2}$. The sheet resistance from the measurements of macroscopic sample surfaces (epitaxially grown graphite: EG; oxidized epitaxially grown graphite: GO$_{epi}$; and reduced GO$_{epi}$: rGO$_{epi}$) was derived from a 2D infinite sheet model, while the sheet resistance of the microscopic 20 $\mu$m × 20 $\mu$m TCNL reduced GO$_{epi}$ patterns (TCNL-rGO$_{epi}$) was derived using a Van der Pauw model. The details of the models are given below.

For measurements on macroscopic samples, the probes were placed in a square configuration with 100 $\mu$m separation between adjoining tips. Since the probes are far away from the edges of the sample which is mm in size, the sample can be regarded as infinitely large and the sheet resistance can be calculated analytically by solving the Poisson equation [197]. The sheet resistance of an infinite 2D sheet measured with square four-point arrangement is independent of the probe spacing and can be derived from the measurements using the equation:

$$R_{sheet} = \frac{\pi}{\ln\sqrt{2}}\frac{\triangle V_{3,4}}{I_{1,2}}. \tag{4.4.1}$$

In order to obtain the sheet resistance of a microscopic 20 $\mu$m × 20 $\mu$m TCNL reduced GO$_{epi}$ pattern (TCNL-rGO$_{epi}$), the STM tips were placed on the corners of the pattern. Since the surrounding GO$_{epi}$ is highly insulating, the electrical current generated from the source tips (T1 and T2) is confined within the pattern boundary. Therefore, we use van der Pauw method [198] to calculate the sheet resistance of the TCNL-rGO$_{epi}$ using the equation:

$$R_{sheet} = \frac{\pi}{\ln 2}\frac{\triangle V_{3,4}}{I_{1,2}}. \tag{4.4.2}$$

The square pattern of TCNL-rGO$_{epi}$ enclosed by dash lines in Fig. 4.4.6 was obtained by rastering a hot tip on the GO surface, with scanning the entire square only once (left to right is the fast scan direction, and top to bottom is the slow scan direction). Since we scanned 512 lines over and area of 20 $\mu$m, the spacing between adjacent scan lines along the slow scan direction is ˜40 nm. These sheet resistance results indicate the good control and reproducibility of TCNL in every scan-line to produce large micron size patterns.

As shown in Fig. 4.4.2, we found that the sheet resistance of the TCNL rGO$_{epi}$ patterns (20 $\mu$m × 20 $\mu$m squares) decreases with increasing the temperature used for the TCNL local reduction, up to four orders of magnitude lower than the resistance of the original GO$_{epi}$ [85]. The same significant increase of the in-plane conductivity is observed for extended films of rGO$_{epi}$ produced by overnight heating of GO$_{epi}$ in a furnace at 600 °C. Furthermore, we found that the sheet resistance and the shape of the $I/V$ characteristics can be varied by changing the temperature of the AFM probe (see Fig. 4.4.2), consistent with a change in the transport gap from 0.5 eV to vanishingly small. These results are consistent with KPFM measurements showing that the TCNL reduced GO$_{epi}$ displays a contact potential change of 168 ± 54 mV with respect to GO$_{epi}$. Due to the residual oxygen and structural disorder, we observe a large difference in conductivity between epitaxial graphene and rGO$_{epi}$ or TCNL-rGO$_{epi}$.

### 4.4.5 Microscopic two-probe electrical transport measurements

Having established that heated tips achieved reductions comparable to global heating treatments, we extended the analysis to an isolated TCNL-rGO$_{epi}$ nanoribbon (Fig. 4.4.7). The TCNL-rGO$_{epi}$ nanoribbon had a length, $L$, of 25 $\mu$m and a width, $w$, of 100 nm as measured by AFM. Current versus voltage data were acquired in the Omicron Nanoprobe system by placing the conductive tips on top of two micron-size squares of rGO$_{epi}$ fabricated in situ by an electron beam at each end of the nanoribbon. These pads ensured good electrical contact with the narrow ribbon. Two point transport measurements indicated a resistance larger than 2 G when the tips were positioned on an arbitrary position on the GO surface (very large barrier at the contact) and a drop in resistance from 120 MΩ (between the 2 squares with no nanoribbon) to 20 MΩ between the 2 squares connected by the nanoribbon). More importantly the transport behavior changes from insulating to ohmic (linear $I/V$ curves) in presence of the TCNL-rGO$_{epi}$ nanoribbon between the squares. By using the relationship $R_{sheet} = (R_{ribbon} \cdot w \cdot t_{ribbon})/(L \cdot t_{sheet})$, and assuming a 13 nm thick nanoribbon, we obtain a sheet resistance of 65 kΩ in very good agreement with the measurements reported in Fig. 4.4.2 for microscopic squares of TCNL-rGO$_{epi}$.

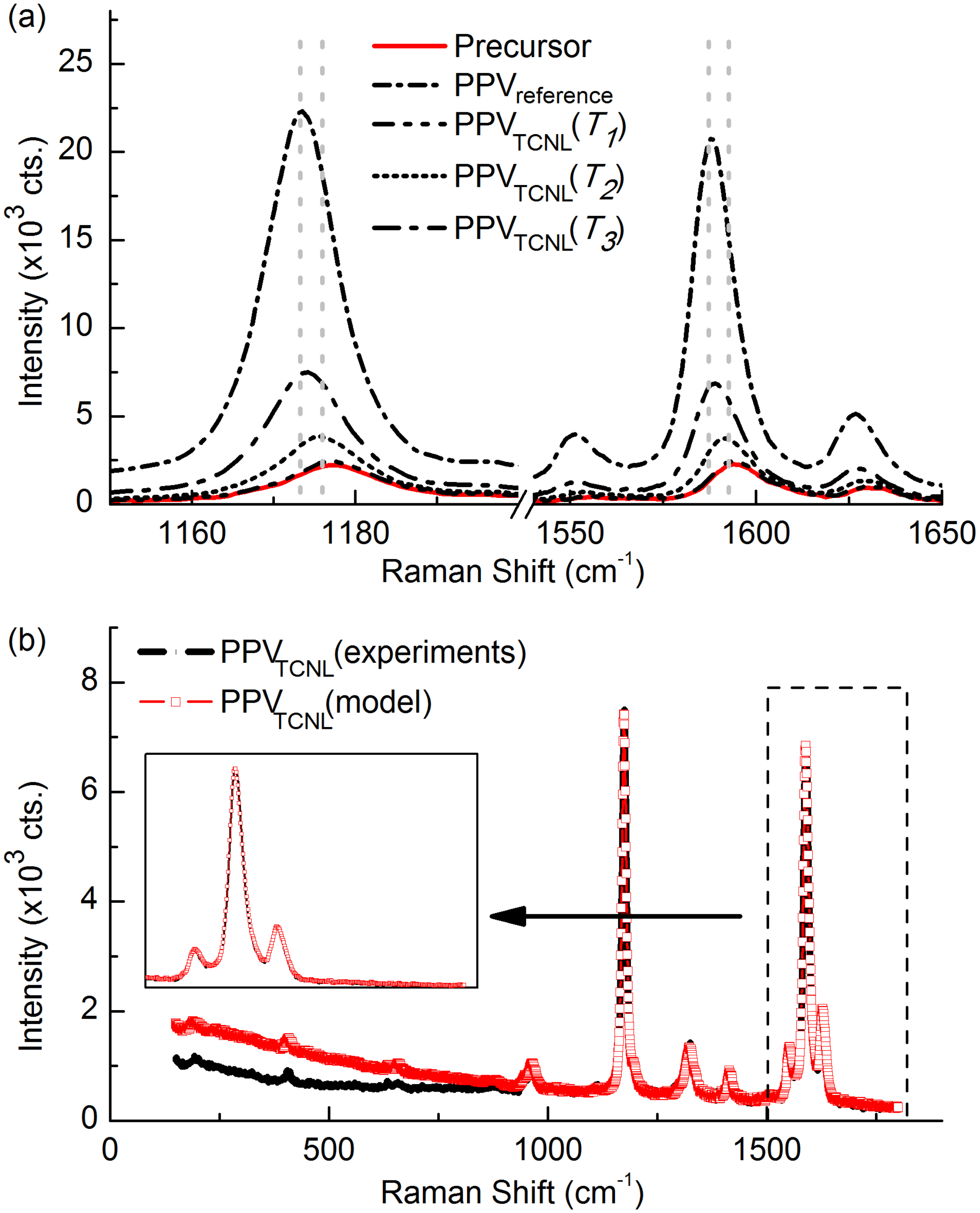

**Figure 4.3.3:** (a) Raman spectra as a function of the temperature used during TCNL, $T_1 = 240\,°C$, $T_2 = 280\,°C$, $T_3 = 320\,°C$, respectively. (b) Comparison between the Raman spectra obtained from the $PPV_{TCNL}$ pattern ($I^{Experimental}_{PPV_{TCNL}}$) and the combined Raman spectra obtained from Eq. 4.3.1 ($I^{Model}_{PPV_{TCNL}}$). Note that the continuum background is much lower in the TCNL sample than in the vacuum-annealed sample according to the model. Reprinted with permission from [173]. Copyright 2009, American Institute of Physics.

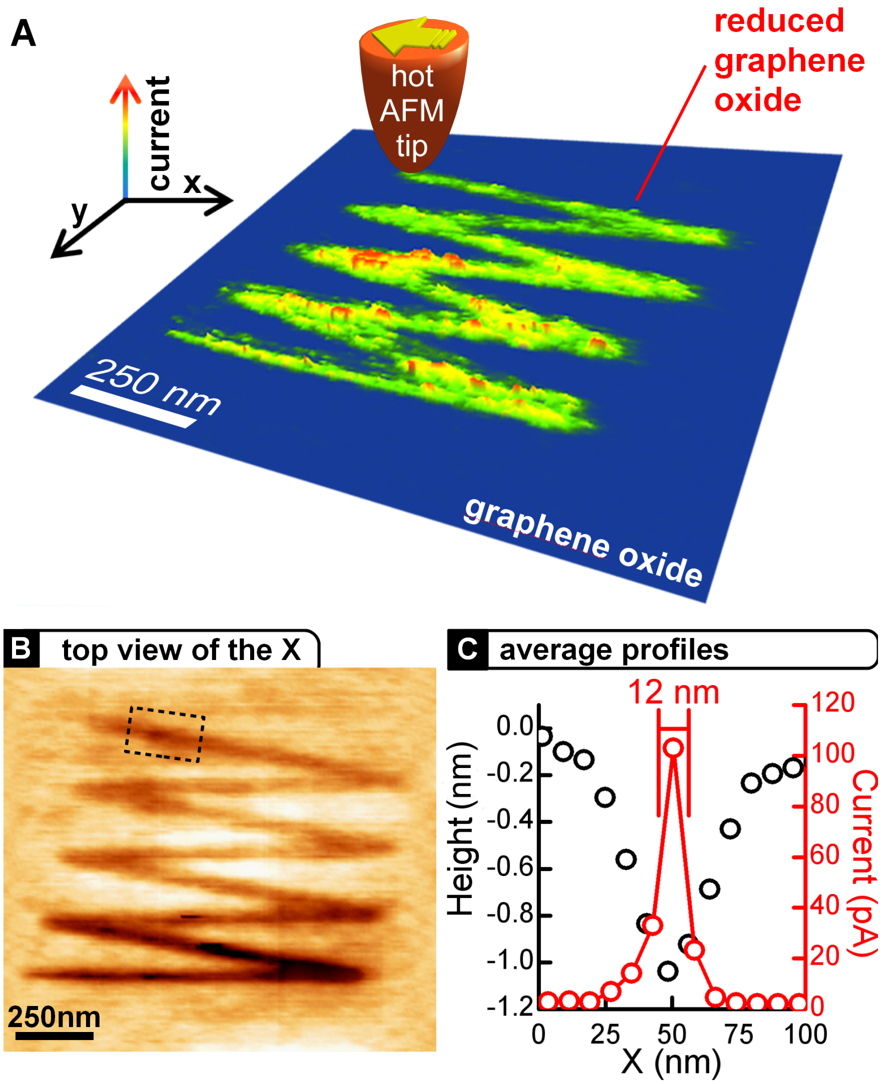

**Figure 4.4.1:** Local thermal reduction of a $GO_{epi}$ film: current and topographical images. (A) 3D CAFM current image (taken with a bias voltage of 2.5 V between tip and substrate) of a zigzag shaped nanowire formed after TCNL was performed on $GO_{epi}$ at $T_{heater}$ ~1060 °C with a linear speed of 0.2 $\mu$m $s^{-1}$ and a load of 120 nN. (B) Corresponding topography image taken simultaneously with (A). (C) Averaged profiles of current and height of the cross sections that are indicated as dashed lines in (A) and (B). From [193]. Reprinted with permission from AAAS.

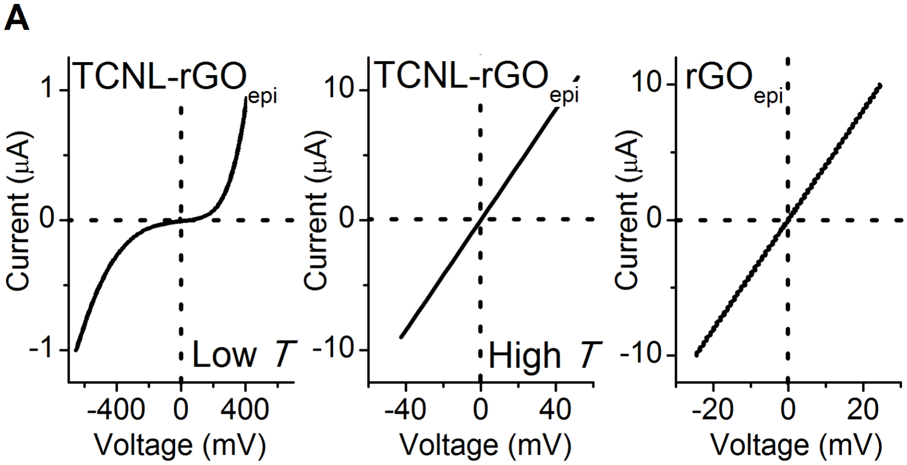

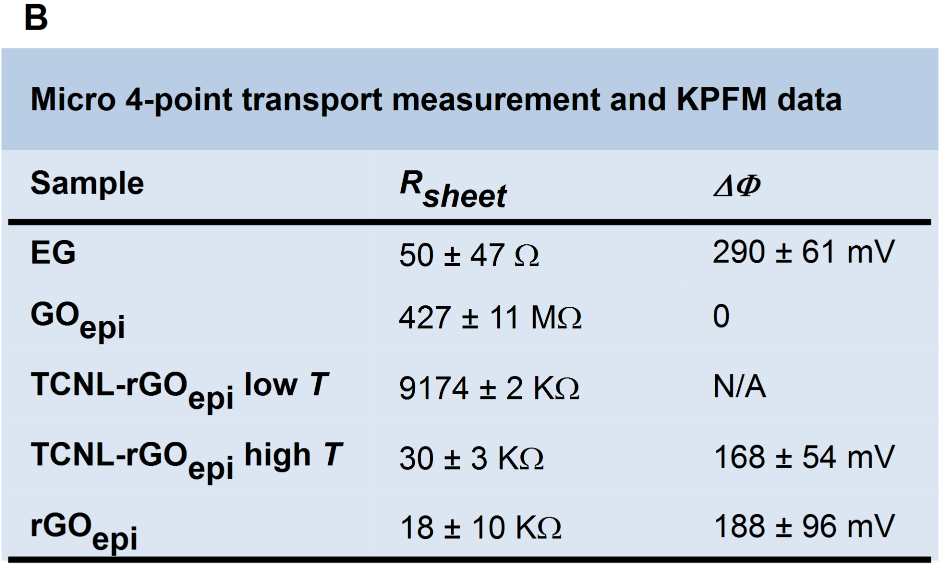

**Micro 4-point transport measurement and KPFM data**

| Sample | $R_{sheet}$ | $\Delta\Phi$ |
|---|---|---|
| **EG** | 50 ± 47 Ω | 290 ± 61 mV |
| **GO$_{epi}$** | 427 ± 11 MΩ | 0 |
| **TCNL-rGO$_{epi}$ low *T*** | 9174 ± 2 KΩ | N/A |
| **TCNL-rGO$_{epi}$ high *T*** | 30 ± 3 KΩ | 168 ± 54 mV |
| **rGO$_{epi}$** | 18 ± 10 KΩ | 188 ± 96 mV |

**Figure 4.4.2:** Micro 4-point transport and Kelvin probe force microscopy measurements. Current-voltage curves obtained by micro 4-point transport measurements of TCNL low-temperature reduced graphene oxide (Low $T$, $T_{heater}$ ~600 °C, TCNL high-temperature reduced graphene oxide (High $T$, $T_{heater}$ ~1200 °C), and vacuum reduced graphene oxide at 600 °C. The table presents the sheet resistance, $R_{sheet}$, measured by 4-point transport measurements, and the contact potential change ($\triangle\Phi$) between GO$_{epi}$ and each listed sample (EG, rGO$_{epi}$, and TCNL-rGO$_{epi}$, respectively). From [193]. Reprinted with permission from AAAS.

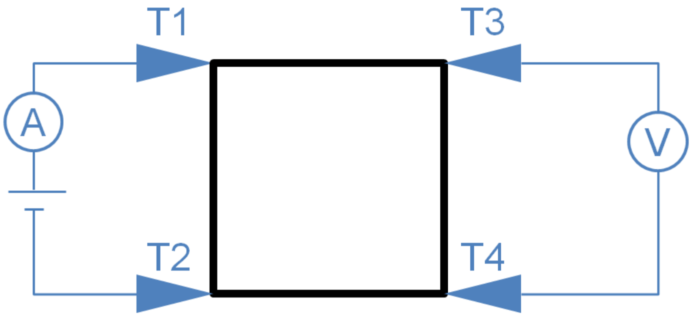

**Figure 4.4.3:** Schematic of microscopic 4-probe electrical transport measurement. From [193]. Reprinted with permission from AAAS.

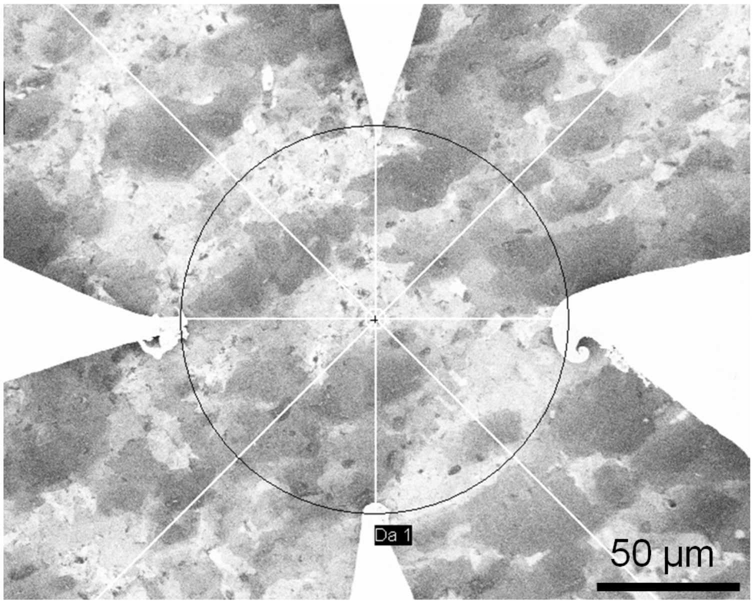

**Figure 4.4.4:** SEM micrograph of 4-point transport measurement of a $GO_{epi}$ film. From [193]. Reprinted with permission from AAAS.

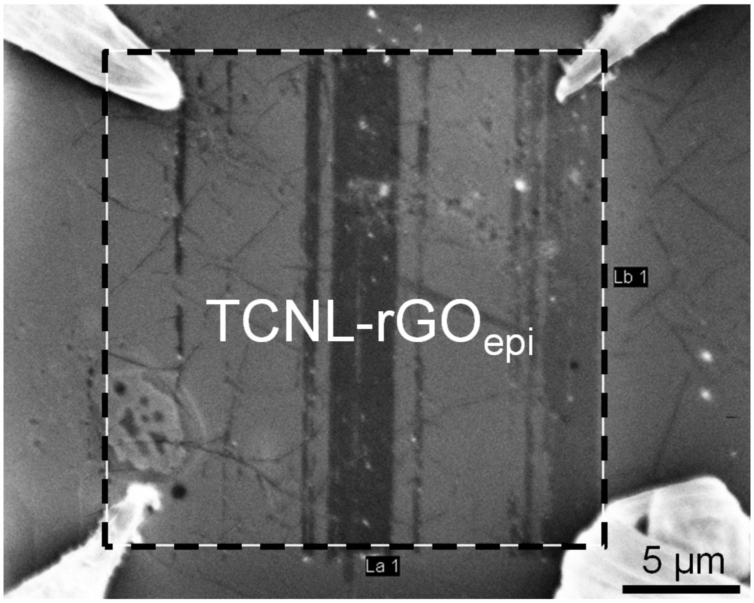
TCNL-rGO$_{epi}$
Lb 1
La 1
5 μm

**Figure 4.4.5:** SEM micrograph of 4-point transport measurement of a GO$_{epi}$ film. From [193]. Reprinted with permission from AAAS.

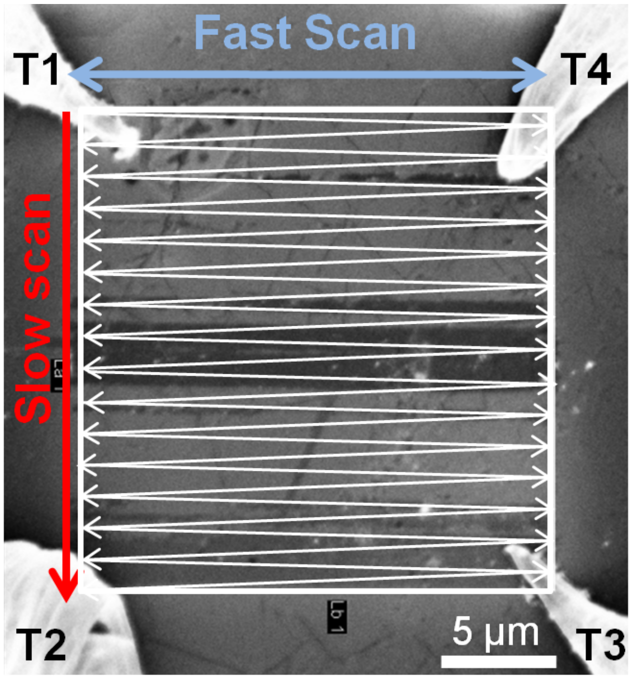
Fast Scan
T1
T4
Slow scan
T2
T3
5 μm

**Figure 4.4.6:** SEM micrograph of the micro 4-probe experiment with a sketch of the tip scan lines during the TCNL reducing. The four conductive probes (T1-T4) used for the resistance measurements are also shown. From [193]. Reprinted with permission from AAAS.

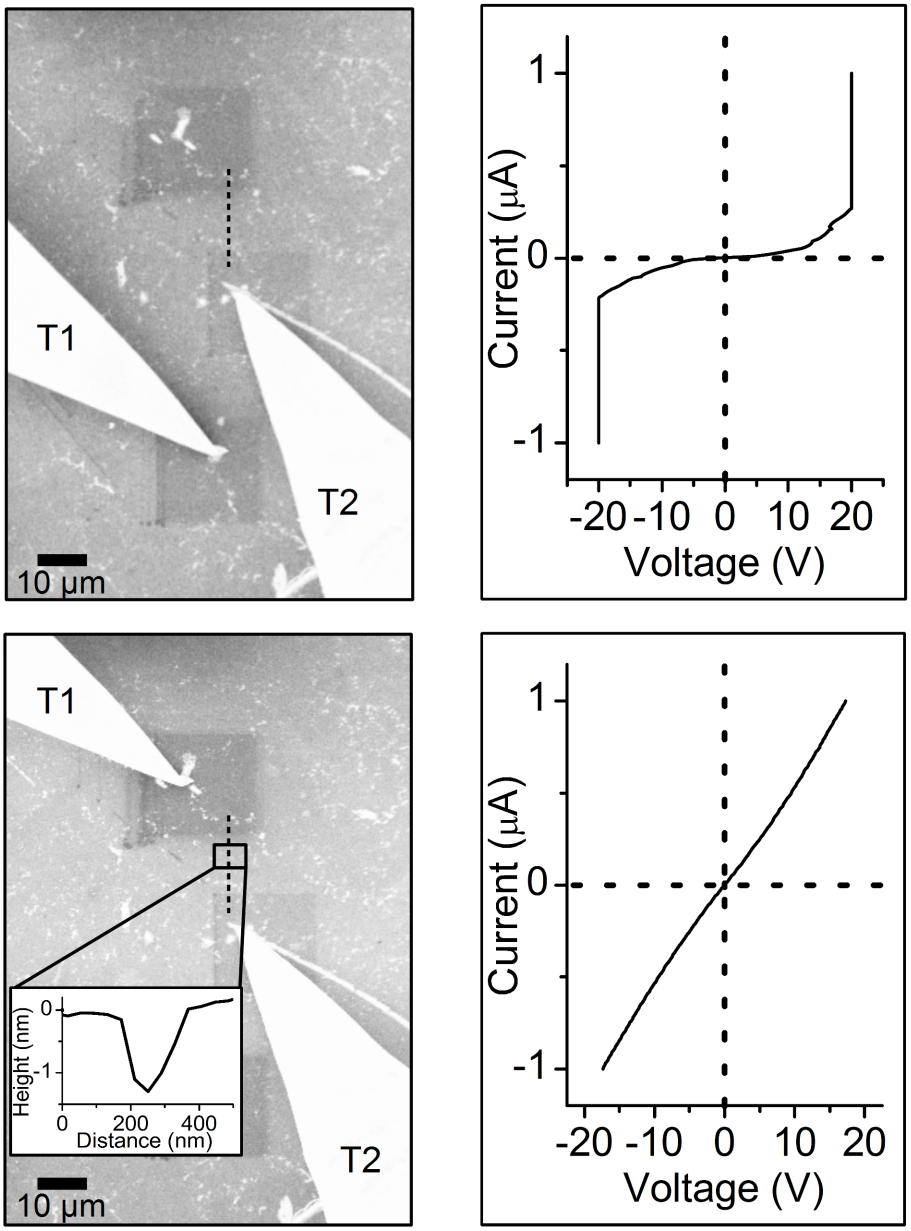

**Figure 4.4.7:** Micro 2-point electrical transport measurement. (Left) SEM images of the configuration used for 2-point transport measurements when the tips are positioned between 2 rGO$_{epi}$ squares without (top), and with (bottom) TCNL-rGO$_{epi}$ nanoribbon in between. The AFM cross section of the nanoribbon is shown as inset of the bottom SEM image. (Right) $I/V$ curves obtained measuring current between 2 rGO$_{epi}$ squares with no nanoribbon in between (top curve), and between 2 rGO$_{epi}$ squares with a nanoribbon in between (bottom curve). From [193]. Reprinted with permission from AAAS.

# CHAPTER V

# CONCLUSIONS AND PERSPECTIVES

In this thesis, we have presented the development of a novel AFM based nanolithography technique: thermochemical nanolithography (TCNL). A systematic study has been conducted to understand the fundamental writing aspects of the TCNL process. A linear relationship between the heater temperature and dissipated power has been established using Raman spectroscopy. The thermal circuit model has been employed to assess the heat flow from the heater to tip-surface contact, and to evaluate the heating efficiency of the heater. According to the thermal kinetics analysis, high temperatures are required to initiate the chemical reactions at tip-sample contact due to the rapid temperature ramping. Finite element analysis has been used to model the temperature profile in the vicinity of the tip-surface contact. A number of key factors that determine the TCNL spatial resolution have been identified, including heating temperature, writing speed, and normal loading force.

We have presented the results of TCNL nanofabrication on a variety of systems and thermochemical reactions. As shown in Section 4.1, the modification of the wettability of a ester polymer surface with write-read-overwrite capability can facilitate the design of complex nanopatterns that are highly desirable for nanofluidic devices. In Section 4.2, the TCNL/CF/MR approach has shown a promising potential on the development of biosensors, and on cell studies that require interactions with two or more proteins in tailor-made patterns. The nanopatterning of conjugated polymer as shown in Section 4.3 could facilitate the design and fabrications of future nanoelectronic and nanophotonic devices. At last, the tunable reduction of graphene oxide is desirable for making all-graphene nanoelectronic devices as shown in Section 4.4.

Several AFM based scanning probe microscopy methods have been implemented to characterize the TCNL nanostructures. These methods include friction force microscopy, tapping mode phase imaging, electric force microscopy, and conductive AFM. We have shown that they are useful for *in situ* characterization of nanostructures, which is particularly challenging for conventional macroscopic analytical tools such as Raman spectroscopy, infrared spectroscopy, and fluorescence microscopy.

We are optimistic that TCNL will have a direct impact on the development of nanodevices as well as fundamental studies of physical, chemical, and biological phenomena at nanoscale. Efforts are underway with the aim of expanding the applicability and improving the robustness of this technique. The throughput and addressable area will be significantly improved by implementation of parallel cantilever arrays as shown in Section 1.3.2, or by combination with supramolecular nanostamping replication technique [199]. The fabrication of ferroelectric nanostructures will promote the understanding of size effects in new physics domain and facilitate the design of novel data storage devices [200].

# REFERENCES

[1] J. V. Barth, G. Costantini, and K. Kern, "Engineering atomic and molecular nanostructures at surfaces," *Nature* **437**, 671 (2005).

[2] M. Bayer, P. Hawrylak, K. Hinzer, S. Fafard, M. Korkusinski, Z. R. Wasilewski, O. Stern, and A. Forchel, "Coupling and entangling of quantum states in quantum dot molecules," *Science* **291**, 451 (2001).

[3] R. H. Baughman, A. A. Zakhidov, and W. A. de Heer, "Carbon nanotubes - the route toward applications," *Science* **297**, 787 (2002).

[4] T. Ito and S. Okazaki, "Pushing the limits of lithography," *Nature* **406**, 1027 (2000).

[5] Y. N. Xia, J. A. Rogers, K. E. Paul, and G. M. Whitesides, "Unconventional methods for fabricating and patterning nanostructures," *Chemical Reviews* **99**, 1823 (1999).

[6] B. D. Gates, Q. B. Xu, M. Stewart, D. Ryan, C. G. Willson, and G. M. Whitesides, "New approaches to nanofabrication: Molding, printing, and other techniques," *Chemical Reviews* **105**, 1171 (2005).

[7] H. M. Saavedra, T. J. Mullen, P. P. Zhang, D. C. Dewey, S. A. Claridge, and P. S. Weiss, "Hybrid strategies in nanolithography," *Reports On Progress In Physics* **73**, 036501 (2010).

[8] R. F. Service, "Can chip devices keep shrinking?," *Science* **274**, 1834 (1996).

[9] G. M. Whitesides, "The 'right' size in nanobiotechnology," *Nature Biotechnology* **21**, 1161 (2003).

[10] S. A. Maier, M. L. Brongersma, P. G. Kik, S. Meltzer, A. A. G. Requicha, and H. A. Atwater, "Plasmonics - a route to nanoscale optical devices," *Advanced Materials* **13**, 1501 (2001).

[11] M. D. Levenson, N. S. Viswanathan, and R. A. Simpson, "Improving resolution in photolithography with a phase-shifting mask," *IEEE Transactions on Electron Devices* **29**, 1828 (1982).

[12] D. R. Medeiros, A. Aviram, C. R. Guarnieri, W. S. Huang, R. Kwong, C. K. Magg, A. P. Mahorowala, W. M. Moreau, K. E. Petrillo, and M. Angelopoulos, "Recent progress in electron-beam a resists for advanced mask-making," *IBM Journal of Research and Development* **45**, 639 (2001).

[13] R. L. Kubena, "Resolution limits of focused-ion-beam resist patterning," *Materials Research Society Symposium Proceeding* **279**, 567 (1992).

[14] E. W. Edwards, M. F. Montague, H. H. Solak, C. J. Hawker, and P. F. Nealey, "Precise control over molecular dimensions of block-copolymer domains using the interfacial energy of chemically nanopatterned substrates," *Advanced Materials* **16**, 1315 (2004).

[15] N. A. Melosh, A. Boukai, F. Diana, B. Gerardot, A. Badolato, P. M. Petroff, and J. R. Heath, "Ultrahigh-density nanowire lattices and circuits," *Science* **300**, 112 (2003).

[16] D. M. Eigler and E. K. Schweizer, "Positioning single atoms with a scanning tunneling microscope," *Nature* **344**, 524 (1990).

[17] S. H. Zaidi and S. R. J. Brueck, "Multiple-exposure Interferometric Lithography," *Journal of Vacuum Science & Technology B* **11**, 658 (1993).

[18] Y. N. Xia, E. Kim, X. M. Zhao, J. A. Rogers, M. Prentiss, and G. M. Whitesides, "Complex optical surfaces formed by replica molding against elastomeric masters," *Science* **273**, 347 (1996).

[19] A. Kumar and G. M. Whitesides, "Features of gold having micrometer to centimeter dimensions can be formed through a combination of stamping with an elastomeric stamp and an alkanethiol ink followed by chemical etching," *Applied Physics Letters* **63**, 2002 (1993).

[20] E. Kim, Y. N. Xia, and G. M. Whitesides, "Polymer microstructures formed by molding in capillaries," *Nature* **376**, 581 (1995).

[21] X. M. Zhao, Y. N. Xia, and G. M. Whitesides, "Fabrication of three-dimensional micro-structures: Microtransfer molding," *Advanced Materials* **8**, 837 (1996).

[22] S. Y. Chou, P. R. Krauss, and P. J. Renstrom, "Imprint of sub-25 nm vias and trenches in polymers," *Applied Physics Letters* **67**, 3114 (1995).

[23] E. Kim, Y. N. Xia, X. M. Zhao, and G. M. Whitesides, "Solvent-assisted microcontact molding: A convenient method for fabricating three-dimensional structures on surfaces of polymers," *Advanced Materials* **9**, 651 (1997).

[24] M. Geissler, H. Wolf, R. Stutz, E. Delamarche, U. W. Grummt, B. Michel, and A. Bietsch, "Fabrication of metal nanowires using microcontact printing," *Langmuir* **19**, 6301 (2003).

[25] G. Krausch and R. Magerle, "Nanostructured thin films via self-assembly of block copolymers," *Advanced Materials* **14**, 1579 (2002).

[26] D. Shu, W. D. Moll, Z. X. Deng, C. D. Mao, and P. X. Guo, "Bottom-up assembly of RNA arrays and superstructures as potential parts in nanotechnology," *Nano Letters* **4**, 1717 (2004).

[27] G. Decher, “Fuzzy nanoassemblies: Toward layered polymeric multicomposites,” *Science* **277**, 1232 (1997).

[28] M. P. Zach, K. H. Ng, and R. M. Penner, “Molybdenum nanowires by electrodeposition,” *Science* **290**, 2120 (2000).

[29] J. Aizenberg, A. J. Black, and G. M. Whitesides, “Controlling local disorder in self-assembled monolayers by patterning the topography of their metallic supports,” *Nature* **394**, 868 (1998).

[30] J. C. Love, K. E. Paul, and G. M. Whitesides, “Fabrication of nanometer-scale features by controlled isotropic wet chemical etching,” *Advanced Materials* **13**, 604 (2001).

[31] J. A. Rogers, K. E. Paul, R. J. Jackman, and G. M. Whitesides, “Using an elastomeric phase mask for sub-100 nm photolithography in the optical near field,” *Applied Physics Letters* **70**, 2658 (1997).

[32] L. Pfeiffer, K. W. West, H. L. Stormer, J. P. Eisenstein, K. W. Baldwin, D. Gershoni, and J. Spector, “Formation of a high-quality 2-dimensional electron-gas on cleaved GaAs,” *Applied Physics Letters* **56**, 1697 (1990).

[33] Q. B. Xu, B. D. Gates, and G. M. Whitesides, “Fabrication of metal structures with nanometer-scale lateral dimensions by sectioning using a microtome,” *Journal of the American Chemical Society* **126**, 1332 (2004).

[34] B. D. Gates, Q. B. Xu, V. R. Thalladi, T. B. Cao, T. Knickerbocker, and G. M. Whitesides, “Shear patterning of microdominos: a new class of procedures for making micro- and nanostructures,” *Angewandte Chemie-international Edition* **43**, 2780 (2004).

[35] G. Binnig, H. Rohrer, C. Gerber, and E. Weibel, “Tunneling through a controllable vacuum gap,” *Applied Physics Letters* **40**, 178 (1982).

[36] G. Binnig, C. F. Quate, and C. Gerber, “Atomic force microscope,” *Physical Review Letters* **56**, 930 (1986).

[37] R. M. Nyffenegger and R. M. Penner, “Nanometer-scale surface modification using the scanning probe microscope: Progress since 1991,” *Chemical Reviews* **97**, 1195 (1997).

[38] R. D. Piner, J. Zhu, F. Xu, S. H. Hong, and C. A. Mirkin, “Dip-pen nanolithography,” *Science* **283**, 661 (1999).

[39] J. A. Dagata, J. Schneir, H. H. Harary, C. J. Evans, M. T. Postek, and J. Bennett, “Modification of hydrogen-passivated silicon by a scanning tunneling Microscope Operating In Air,” *Applied Physics Letters* **56**, 2001 (1990).

[40] P. Vettiger, G. Cross, M. Despont, U. Drechsler, U. Durig, B. Gotsmann, W. Haberle, M. A. Lantz, H. E. Rothuizen, R. Stutz, and G. K. Binnig, "The "millipede" - Nanotechnology entering data storage," *IEEE Transactions on Nanotechnology* **1**, 39 (2002).

[41] R. Neffati, A. Alexeev, S. Saunin, J. C. M. Brokken-Zijp, D. Wouters, S. Schmatloch, U. S. Schubert, and J. Loos, "Automated scanning probe microscopy as a new tool for combinatorial polymer research: Conductive carbon black/poly(dimethylsiloxane) composites," *Macromolecular Rapid Communications* **24**, 113 (2003).

[42] Y. Hu, A. Das, M. H. Hecht, and G. Scoles, "Nanografting de novo proteins onto gold surfaces," *Langmuir* **21**, 9103 (2005).

[43] S. Xu and G. Y. Liu, "Nanometer-scale fabrication by simultaneous nanoshaving and molecular self-assembly," *Langmuir* **13**, 127 (1997).

[44] B. Klehn and U. Kunze, "Nanolithography with an atomic force microscope by means of vector-scan controlled dynamic plowing," *Journal of Applied Physics* **85**, 3897 (1999).

[45] R. W. Carpick and M. Salmeron, "Scratching the surface: Fundamental investigations of tribology with atomic force microscopy," *Chemical Reviews* **97**, 1163 (1997).

[46] J. C. Rosa, M. Wendel, H. Lorenz, J. P. Kotthaus, M. Thomas, and H. Kroemer, "Direct patterning of surface quantum wells with an atomic force microscope," *Applied Physics Letters* **73**, 2684 (1998).

[47] J. C. Garno, Y. Y. Yang, N. A. Amro, S. Cruchon-Dupeyrat, S. W. Chen, and G. Y. Liu, "Precise positioning of nanoparticles on surfaces using scanning probe lithography," *Nano Letters* **3**, 389 (2003).

[48] J. F. Liu, S. Cruchon-Dupeyrat, J. C. Garno, J. Frommer, and G. Y. Liu, "Three-dimensional nanostructure construction via nanografting: Positive and negative pattern transfer," *Nano Letters* **2**, 937 (2002).

[49] H. Sugimura and N. Nakagiri, "Chemical approach to nanofabrication - modifications of silicon surfaces patterned by scanning probe anodization," *Japanese Journal of Applied Physics Part 1-regular Papers Short Notes & Review Papers* **34**, 3406 (1995).

[50] S. C. Minne, P. Flueckiger, H. T. Soh, and C. F. Quate, "Atomic-force microscope lithography using amorphous-silicon as a resist and advances in parallel operation," *Journal of Vacuum Science & Technology B* **13**, 1380 (1995).

[51] C. R. K. Marrian, F. K. Perkins, S. L. Brandow, T. S. Koloski, E. A. Dobisz, and J. M. Calvert, "Low-voltage electron-beam lithography in self-assembled

ultrathin films with the scanning tunneling microscope," *Applied Physics Letters* **64**, 390 (1994).

[52] M. Rolandi, C. F. Quate, and H. J. Dai, "A new scanning probe lithography scheme with a novel metal resist," *Advanced Materials* **14**, 191 (2002).

[53] E. Betzig and J. K. Trautman, "Near-field optics- microscopy, spectroscopy, and surface modification beyond the diffraction limit," *Science* **257**, 189 (1992).

[54] E. Betzig, J. K. Trautman, R. Wlofe, E. M. Gyorgy, P. L. Finn, M. H. Kryder, and C. H. Chang, "Near-field Magnetooptics and High-density Data-storage," *Applied Physics Letters* **61**, 142 (1992).

[55] R. Riehn, A. Charas, J. Morgado, and F. Cacialli, "Near-field optical lithography of a conjugated polymer," *Applied Physics Letters* **82**, 526 (2003).

[56] S. Q. Sun and G. J. Leggett, "Generation of nanostructures by scanning near-field photolithography of self-assembled monolayers and wet chemical etching," *Nano Letters* **2**, 1223 (2002).

[57] D. S. Ginger, H. Zhang, and C. A. Mirkin, "The evolution of dip-pen nanolithography," *Angewandte Chemie-International Edition* **43**, 30 (2004).

[58] S. H. Hong, J. Zhu, and C. A. Mirkin, "Multiple ink nanolithography: Toward a multiple-pen nano-plotter," *Science* **286**, 523 (1999).

[59] A. Noy, A. E. Miller, J. E. Klare, B. L. Weeks, B. W. Woods, and J. J. DeYoreo, "Fabrication of luminescent nanostructures and polymer nanowires using dip-pen nanolithography," *Nano Letters* **2**, 109 (2002).

[60] L. M. Demers, D. S. Ginger, S. J. Park, Z. Li, S. W. Chung, and C. A. Mirkin, "Direct patterning of modified oligonucleotides on metals and insulators by dip-pen nanolithography," *Science* **296**, 1836 (2002).

[61] L. A. Porter, H. C. Choi, J. M. Schmeltzer, A. E. Ribbe, L. C. C. Elliott, and J. M. Buriak, "Electroless nanoparticle film deposition compatible with photolithography, microcontact printing, and dip-pen nanolithography patterning technologies," *Nano Letters* **2**, 1369 (2002).

[62] D. A. Weinberger, S. G. Hong, C. A. Mirkin, B. W. Wessels, and T. B. Higgins, "Combinatorial generation and analysis of nanometer- and micrometer-scale silicon features via "dip-pen" nanolithography and wet chemical etching," *Advanced Materials* **12**, 1600 (2000).

[63] M. Zhang, D. Bullen, S. W. Chung, S. Hong, K. S. Ryu, Z. F. Fan, C. A. Mirkin, and C. Liu, "A MEMS nanoplotter with high-density parallel dip-pen manolithography probe arrays," *Nanotechnology* **13**, 212 (2002).

[64] X. F. Wang and C. Liu, "Multifunctional probe array for nano patterning and imaging," *Nano Letters* **5**, 1867 (2005).

[65] J. Zou, D. Bullen, X. F. Wang, C. Liu, and C. A. Mirkin, "Conductivity-based contact sensing for probe arrays in dip-pen nanolithography," *Applied Physics Letters* **83**, 581 (2003).

[66] T. Thorsen, S. J. Maerkl, and S. R. Quake, "Microfluidic large-scale integration," *Science* **298**, 580 (2002).

[67] A. Majumdar, "Scanning thermal microscopy," *Annual Review of Materials Science* **29**, 505 (1999).

[68] A. Hammiche, H. M. Pollock, M. Song, and D. J. Hourston, "Sub-surface imaging by scanning thermal microscopy," *Measurement Science & Technology* **7**, 142 (1996).

[69] M. H. Li and Y. B. Gianchandani, "Microcalorimetry applications of a surface micromachined bolometer-type thermal probe," *Journal of Vacuum Science & Technology B* **18**, 3600 (2000).

[70] H. J. Mamin, B. D. Terris, L. S. Fan, S. Hoen, R. C. Barrett, and D. Rugar, "High-density data storage using proximal probe techniques," *IBM Journal of Research and Development* **39**, 681 (1995).

[71] J. J. M. Ruigrok, R. Coehoorn, S. R. Cumpson, and H. W. Kesteren, "Disk recording beyond 100 Gb/in.(2): Hybrid recording?," *Journal of Applied Physics* **87**, 5398 (2000).

[72] H. J. Mamin and D. Rugar, "Thermomechanical Writing With An Atomic Force Microscope Tip," *Applied Physics Letters* **61**, 1003 (1992).

[73] M. Lutwyche, C. Andreoli, G. Binnig, J. Brugger, U. Drechsler, W. Haberle, H. Rohrer, H. Rothuizen, P. Vettiger, G. Yaralioglu, and C. Quate, "5X5 2D AFM cantilever arrays a first step towards a Terabit storage device," *Sensors and Actuators A-physical* **73**, 89 (1999).

[74] M. Despont, U. Drechsler, R. Yu, H. B. Pogge, and P. Vettiger, "Wafer-scale microdevice transfer/interconnect: Its application in an AFM-based data-storage system," *Journal of Microelectromechanical Systems* **13**, 895 (2004).

[75] A. Pantazi, A. Sebastian, T. A. Antonakopoulos, P. Baechtold, A. R. Bonaccio, J. Bonan, G. Cherubini, M. Despont, R. A. DiPietro, U. Drechsler, U. Duerig, B. Gotsmann, W. Haeberle, C. Hagleitner, J. L. Hedrick, D. Jubin, A. Knoll, M. A. Lantz, J. Pentaralkis, H. Pozidis, R. C. Pratt, H. Rothuizen, R. Stutz, M. Varsamou, D. Wiesmann, and E. Eleftheriou, "Probe-based ultrahigh-density storage technology," *IBM Journal of Research and Development* **52**, 493 (2008).

[76] M. A. Lantz, B. Gotsmann, U. T. Durig, P. Vettiger, Y. Nakayama, T. Shimizu, and H. Tokumoto, “Carbon nanotube tips for thermomechanical data storage,” *Applied Physics Letters* **83**, 1266 (2003).

[77] B. Gotsmann and U. Durig, “Thermally activated nanowear modes of a polymer surface induced by a heated tip,” *Langmuir* **20**, 1495 (2004).

[78] R. Szoszkiewicz, T. Okada, S. C. Jones, T. D. Li, W. P. King, S. R. Marder, and E. Riedo, “High-speed, sub-15 nm feature size thermochemical nanolithography,” *Nano Letters* **7**, 1064 (2007).

[79] D. Wang, V. K. Kodali, W. D. Underwood, J. E. Jarvholm, T. Okada, S. C. Jones, M. Rumi, Z. Dai, W. P. King, S. R. Marder, J. E. Curtis, and E. Riedo, “Thermochemical nanolithography of multifunctional nanotemplates for assembling nano-objects,” *Advanced Functional Materials* **19**, 1 (2009).

[80] J. H. Burroughes, D. D. C. Bradley, A. R. Brown, R. N. Marks, K. Mackay, R. H. Friend, P. L. Burns, and A. B. Holmes, “Light-emitting-diodes based on conjugated polymers,” *Nature* **347**, 539 (1990).

[81] D. D. C. Bradley, “Precursor-route poly(p-phenylenevinylene) -polymer characterization and control of electronic-properties,” *Journal of Physics D-Applied Physics* **20**, 1389 (1987).

[82] C. Berger, Z. M. Song, X. B. Li, X. S. Wu, N. Brown, C. Naud, D. Mayou, T. B. Li, J. Hass, A. N. Marchenkov, E. H. Conrad, P. N. First, and W. A. de Heer, “Electronic confinement and coherence in patterned epitaxial graphene,” *Science* **312**, 1191 (2006).

[83] J. Hass, F. Varchon, J. E. Millan-Otoya, M. Sprinkle, N. Sharma, W. A. De Heer, C. Berger, P. N. First, L. Magaud, and E. H. Conrad, “Why multilayer graphene on 4H-SiC$<000(\bar{1})>$ behaves like a single sheet of graphene,” *Physical Review Letters* **100**, 125504 (2008).

[84] W. S. Hummers and R. E. Offeman, “Preparation of Graphitic Oxide,” *Journal of the American Chemical Society* **80**, 1339 (1958).

[85] X. S. Wu, M. Sprinkle, X. B. Li, F. Ming, C. Berger, and W. A. de Heer, “Epitaxial-graphene/graphene-oxide junction: An essential step towards epitaxial graphene electronics,” *Physical Review Letters* **101**, 026801 (2008).

[86] D. Rugar and P. Hansmar, “Atomic force microscopy,” *Physics Today* **43**, 23 (1990).

[87] J. N. Israelachvili, *Intermolecular and Surface Forces* (Academic Press, New York, 1992).

[88] M. A. Poggi, A. W. McFarland, J. S. Colton, and L. A. Bottomley, "A method for calculating the spring constant of atomic force microscopy cantilevers with a nonrectangular cross section," *Analytical Chemistry* **77**, 1192 (2005).

[89] R. Garcia and R. Perez, "Dynamic atomic force microscopy methods," *Surface Science Reports* **47**, 197 (2002).

[90] E. Riedo, I. Pallaci, C. Boragno, and H. Brune, "The 2/3 power law dependence of capillary force on normal load in nanoscopic friction," *Journal of Physical Chemistry B* **108**, 5324 (2004).

[91] K. L. Johnson, *Contact Mechanics* (Cambridge University Press, Cambridge, 1987).

[92] E. Meyer, H. J. Hug, and R. Bennewitz, *Scanning Probe Microscopy: The Lab on A Tip* (Springer, New York, 2003).

[93] R. Szoszkiewicz and E. Riedo, "Nucleation time of nanoscale water bridges," *Physical Review Letters* **95**, 135502 (2005).

[94] D. Wang, R. Szoszkiewicz, M. Lucas, E. Riedo, T. Okada, S. C. Jones, S. R. Marder, J. Lee, and W. P. King, "Local wettability modification by thermochemical nanolithography with write-read-overwrite capability," *Applied Physics Letters* **91**, 243104 (2007).

[95] H. G. Hansma, K. J. Kim, D. E. Laney, R. A. Garcia, M. Argaman, M. J. Allen, and S. M. Parsons, "Properties of biomolecules measured from atomic force microscope images: A review," *Journal of Structural Biology* **119**, 99 (1997).

[96] M. Rammacher, R. W. Tilmann, and H. E. Gaub, "Imaging viscoelasticity by force modulation with the atomic force microscope," *Biophysical Journal* **64**, 735 (1993).

[97] S. N. Magonov, V. Elings, and M. H. Whangbo, "Phase imaging and stiffness in tapping-mode atomic force microscopy," *Surface Science* **375**, L385 (1997).

[98] W. Frammelsberger, G. Benstetter, J. Kiely, and R. Stamp, "Thickness determination of thin and ultra-thin $SiO_2$ films by C-AFM IV-spectroscopy," *Applied Surface Science* **252**, 2375 (2006).

[99] V. Palermo, M. Palma, and P. Samori, "Electronic characterization of organic thin films by Kelvin probe force microscopy," *Advanced Materials* **18**, 145 (2006).

[100] M. Nonnenmacher, M. P. Oboyle, and H. K. Wickramasinghe, "Kelvin probe force microscopy," *Applied Physics Letters* **58**, 2921 (1991).

[101] W. Frammelsberger, G. Benstetter, R. Stamp, J. Kiely, and T. Schweinboeck, "Simplified tunnelling current calculation for MOS structures with ultra-thin oxides for conductive atomic force microscopy investigations," *Materials Science and Engineering B-solid State Materials For Advanced Technology* **116**, 168 (2005).

[102] Lenzling.M and E. H. Snow, "Fowler-Nordheim tunneling into thermally grown $SiO_2$," *Journal of Applied Physics* **40**, 278 (1969).

[103] R. J. Good, "Contact-angle, wetting, and adhesion - a critical-review," *Journal of Adhesion Science and Technology* **6**, 1269 (1992).

[104] R. J. Good, "Surface free-energy of solids and liquids - thermodynamics, molecular forces, and structure," *Journal of Colloid and Interface Science* **59**, 398 (1977).

[105] N. B. Colthup, L. H. Daly, and S. E. Wiberley, *Introduction to Infrared and Raman Spectroscopy* (Academic Press, New York, 1990).

[106] J. R. Ferraro, *Introductory Raman Spectroscopy* (Academic Press, New York, 2002).

[107] B. Herman and J. J. Lemasters, *Optical Microscopy: Emerging Methods and Applications* (Academic Press, New York, 1993).

[108] F. W. D. Rost, *Fluorescence Microscopy* (Cambridge University Press, Cambridge, 1992).

[109] J. B. Pawley, *Handbook of Biological Confocal Microscopy* (Springer, New York, 2006).

[110] J. Lee, T. Beechem, T. L. Wright, B. A. Nelson, S. Graham, and W. P. King, "Electrical, thermal, and mechanical characterization of silicon microcantilever heaters," *Journal of Microelectromechanical Systems* **15**, 1644 (2006).

[111] J. P. Cleveland, S. Manne, D. Bocek, and P. K. Hansma, "A nondestructive method for determining the spring constant of cantilevers for scanning force microscopy," *Review of Scientific Instruments* **64**, 403 (1993).

[112] J. L. Hutter and J. Bechhoefer, "Calibration of atomic-force microscope tips," *Review of Scientific Instruments* **64**, 1868 (1993).

[113] J. E. Sader, J. W. M. Chon, and P. Mulvaney, "Calibration of rectangular atomic force microscope cantilevers," *Review of Scientific Instruments* **70**, 3967 (1999).

[114] M. L. B. Palacio and B. Bhushan, "Normal and lateral force calibration techniques for AFM cantilevers," *Critical Reviews in Solid State and Materials Sciences* **35**, 73 (2010).

[115] C. T. Gibson, G. S. Watson, and S. Myhra, "Determination of the spring constants of probes for force microscopy/spectroscopy," *Nanotechnology* **7**, 259 (1996).

[116] C. T. Gibson, B. L. Weeks, J. R. I. Lee, C. Abell, and T. Rayment, "A nondestructive technique for determining the spring constant of atomic force microscope cantilevers," *Review of Scientific Instruments* **72**, 2340 (2001).

[117] B. W. Chui, M. Asheghi, Y. S. Ju, K. E. Goodson, T. W. Kenny, and H. J. Mamin, "Intrinsic-carrier thermal runaway in silicon microcantilevers," *Microscale Thermophysical Engineering* **3**, 217 (1999).

[118] B. A. Nelson and W. P. King, "Modeling and simulation of the interface temperature between a heated silicon tip and a substrate," *Nanoscale and Microscale Thermophysical Engineering* **12**, 98 (2008).

[119] M. R. Abel, T. L. Wright, W. P. King, and S. Graham, "Thermal metrology of silicon microstructures using Raman spectroscopy," *IEEE Transactions on Components and Packaging Technologies* **30**, 200 (2007).

[120] B. Bhushan and H. Fuchs, *Applied Scanning Probe Methods IV: Industrial Applications* (Springer, Berlin, 2006).

[121] G. Chen, "Phonon heat conduction in nanostructures," *International Journal of Thermal Sciences* **39**, 471 (2000).

[122] C. Hu, M. Kiene, and P. S. Ho, "Thermal conductivity and interfacial thermal resistance of polymeric low k films," *Applied Physics Letters* **79**, 4121 (2001).

[123] M. M. Yovanovich, J. R. Culham, and P. Teertstra, "Analytical modeling of spreading resistance in flux tubes, half spaces, and compound disks," *Ieee Transactions on Components Packaging and Manufacturing Technology Part A* **21**, 168 (1998).

[124] D. R. Lide, *CRC Handbook of Chemistry and Physics* (CRC Press, New York, 2002).

[125] A. J. Bullen, K. E. O'Hara, D. G. Cahill, O. Monteiro, and A. von Keudell, "Thermal conductivity of amorphous carbon thin films," *Journal of Applied Physics* **88**, 6317 (2000).

[126] M. Levinshtein, S. Rumyantsev, and M. Shur, *Properties of Advanced SemiconductorMaterials GaN, AlN, SiC, BN, SiC, SiGe* (John Wiley & Sons, New York, 2001).

[127] J. Zsako, "Kinetic analysis of thermogravimetric data," *Journal of Physical Chemistry* **72**, 2406 (1968).

[128] O. Fenwick, L. Bozec, D. Credgington, A. Hammiche, G. M. Lazzerini, Y. R. Silberberg, and F. Cacialli, "Thermochemical nanopatterning of organic semiconductors," *Nature Nanotechnology* **4**, 664 (2009).

[129] R. Garcia, R. V. Martinez, and J. Martinez, "Nano-chemistry and scanning probe nanolithographies," *Chemical Society Reviews* **35**, 29 (2006).

[130] X. N. Xie, H. J. Chung, C. H. Sow, and A. T. S. Wee, "Nanoscale materials patterning and engineering by atomic force microscopy nanolithography," *Materials Science & Engineering R-Reports* **54**, 1 (2006).

[131] W. Fudickar, A. Fery, and T. Linker, "Reversible light and air-driven lithography by singlet oxygen," *Journal of the American Chemical Society* **127**, 9386 (2005).

[132] I. Turyan, U. O. Krasovec, B. Orel, T. Saraidorov, R. Reisfeld, and D. Mandler, "Writing-reading-erasing on tungsten oxide films using the scanning electrochemical microscope," *Advanced Materials* **12**, 330 (2000).

[133] K. Seo and E. Borguet, "Nanolithographic write, read, and erase via reversible nanotemplated nanostructure electrodeposition on alkanethiol-modified Au(111) in an aqueous solution," *Langmuir* **22**, 1388 (2006).

[134] M. A. Lantz, B. Gotsmann, U. T. Durig, P. Vettiger, Y. Nakayama, T. Shimizu, and H. Tokumoto, "Carbon nanotube tips for thermomechanical data storage," *Applied Physics Letters* **83**, 1266 (2003).

[135] W. Gokel, *Dean's Handbook of Organic Chemistry* (McGraw-Hill, New York, 2004).

[136] R. S. Kane, S. Takayama, E. Ostuni, D. E. Ingber, and G. M. Whitesides, "Patterning proteins and cells using soft lithography," *Biomaterials* **20**, 2363 (1999).

[137] R. Szoszkiewicz and E. Riedo, "Nanoscopic friction as a probe of local phase transitions," *Applied Physics Letters* **87**, 033105 (2005).

[138] R. V. Martinez, N. S. Losilla, J. Martinez, Y. Huttel, and R. Garcia, "Patterning polymeric structures with 2 nm resolution at 3 nm half pitch in ambient conditions," *Nano Letters* **7**, 1846 (2007).

[139] E. Menard, M. A. Meitl, Y. G. Sun, J. U. Park, D. J. L. Shir, Y. S. Nam, S. Jeon, and J. A. Rogers, "Micro- and nanopatterning techniques for organic electronic and optoelectronic systems," *Chemical Reviews* **107**, 1117 (2007).

[140] K. L. Christman, V. D. Enriquez-Rios, and H. D. Maynard, "Nanopatterning proteins and peptides," *Soft Matter* **2**, 928 (2006).

[141] K. Salaita, Y. H. Wang, and C. A. Mirkin, “Applications of dip-pen nanolithography,” *Nature Nanotechnology* **2**, 145 (2007).

[142] Z. H. Nie and E. Kumacheva, “Patterning surfaces with functional polymers,” *Nature Materials* **7**, 277 (2008).

[143] F. W. Huo, Z. J. Zheng, G. F. Zheng, L. R. Giam, H. Zhang, and C. A. Mirkin, “Polymer pen lithography,” *Science* **321**, 1658 (2008).

[144] I. Bita, J. K. W. Yang, Y. S. Jung, C. A. Ross, E. L. Thomas, and K. K. Berggren, “Graphoepitaxy of self-assembled block copolymers on two-dimensional periodic patterned templates,” *Science* **321**, 939 (2008).

[145] J. F. Mooney, A. J. Hunt, J. R. McIntosh, C. A. Liberko, D. M. Walba, and C. T. Rogers, “Patterning of functional antibodies and other proteins by photolithography of silane monolayers,” *Proceedings of the National Academy of Sciences of the United States of America* **93**, 12287 (1996).

[146] F. A. Denis, A. Pallandre, B. Nysten, A. M. Jonas, and C. C. Dupont-Gillain, “Alignment and assembly of adsorbed collagen molecules induced by anisotropic chemical nanopatterns,” *Small* **1**, 984 (2005).

[147] H. W. Li, B. V. O. Muir, G. Fichet, and W. T. S. Huck, “Nanocontact printing: A route to sub-50-nm-scale chemical and biological patterning,” *Langmuir* **19**, 1963 (2003).

[148] J. P. Spatz, “Nano- and micropatterning by organic - Inorganic templating of hierarchical self-assembled structures,” *Angewandte Chemie-International Edition* **41**, 3359 (2002).

[149] K. B. Lee, S. J. Park, C. A. Mirkin, J. C. Smith, and M. Mrksich, “Protein nanoarrays generated by dip-pen nanolithography,” *Science* **295**, 1702 (2002).

[150] K. Wadu-Mesthrige, S. Xu, N. A. Amro, and G. Y. Liu, “Fabrication and imaging of nanometer-sized protein patterns,” *Langmuir* **15**, 8580 (1999).

[151] Y. B. Zhang, Y. W. Tan, H. L. Stormer, and P. Kim, “Experimental observation of the quantum Hall effect and Berry’s phase in graphene,” *Nature* **438**, 201 (2005).

[152] A. Bruckbauer, D. J. Zhou, L. M. Ying, Y. E. Korchev, C. Abell, and D. Klenerman, “Multicomponent submicron features of biomolecules created by voltage controlled deposition from a nanopipet,” *Journal of the American Chemical Society* **125**, 9834 (2003).

[153] Y. Kobayashi, M. Sakai, A. Ueda, K. Maruyama, T. Saiki, and K. Suzuki, “Writing and reading methodology for biochips with sub-100-nm chemical patterns based on near-field scanning optical microscopy,” *Analytical Sciences* **24**, 571 (2008).

[154] M. Z. Liu, N. A. Amro, C. S. Chow, and G. Y. Liu, "Production of nanostructures of DNA on surfaces," *Nano Letters* **2**, 863 (2002).

[155] X. Z. Zhou, Y. H. Chen, B. Li, G. Lu, F. Y. C. Boey, J. Ma, and H. Zhang, "Controlled growth of peptide nanoarrays on Si/SiOx substrates," *Small* **4**, 1324 (2008).

[156] H. Zhang, K. B. Lee, Z. Li, and C. A. Mirkin, "Biofunctionalized nanoarrays of inorganic structures prepared by dip-pen nanolithography," *Nanotechnology* **14**, 1113 (2003).

[157] S. W. Lee, B. K. Oh, R. G. Sanedrin, K. Salaita, T. Fujigaya, and C. A. Mirkin, "Biologically active protein nanoarrays generated using parallel dip-pen nanolithography," *Advanced Materials* **18**, 1133 (2006).

[158] A. Tinazli, J. Piehler, M. Beuttler, R. Guckenberger, and R. Tampe, "Native protein nanolithography that can write, read and erase," *Nature Nanotechnology* **2**, 220 (2007).

[159] M. Arnold, E. A. Cavalcanti-Adam, R. Glass, J. Blummel, W. Eck, M. Kantlehner, H. Kessler, and J. P. Spatz, "Activation of integrin function by nanopatterned adhesive interfaces," *Chemphyschem* **5**, 383 (2004).

[160] G. T. Hermanson, *Bioconjugate Techniques*, 1st ed. (Academic Press, London, 1996).

[161] J. U. Park, J. H. Lee, U. Paik, Y. Lu, and J. A. Rogers, "Nanoscale Patterns of Oligonucleotides Formed by Electrohydrodynamic Jet Printing with Applications in Biosensing and Nanomaterials Assembly," *Nano Letters* **8**, 4210 (2008).

[162] W. P. King and K. E. Goodson, "Thermomechanical formation of nanoscale polymer indents with a heated silicon tip," *Journal of Heat Transfer-Transactions of the Asme* **129**, 1600 (2007).

[163] K. Vallieres, P. Chevallier, C. Sarra-Bournett, S. Turgeon, and G. Laroche, "AFM Imaging of immobilized fibronectin: Does the surface conjugation scheme affect the protein orientation/conformation?," *Langmuir* **23**, 9745 (2007).

[164] H. Sirringhaus, T. Kawase, R. H. Friend, T. Shimoda, M. Inbasekaran, W. Wu, and E. P. Woo, "High-resolution inkjet printing of all-polymer transistor circuits," *Science* **290**, 2123 (2000).

[165] M. Granstrom, K. Petritsch, A. C. Arias, A. Lux, M. R. Andersson, and R. H. Friend, "Laminated fabrication of polymeric photovoltaic diodes," *Nature* **395**, 257 (1998).

[166] M. H. Yun, N. V. Myung, R. P. Vasquez, C. S. Lee, E. Menke, and R. M. Penner, "Electrochemically grown wires for individually addressable sensor arrays," *Nano Letters* **4**, 419 (2004).

[167] J. Kameoka, D. Czaplewski, H. Q. Liu, and H. G. Craighead, "Polymeric nanowire architecture," *Journal of Materials Chemistry* **14**, 1503 (2004).

[168] E. Tekin, E. Holder, D. Kozodaev, and U. S. Schubert, "Controlled pattern formation of poly [2-methoxy-5(2 '-ethylhexyloxyl)-1,4-phenylenevinylene] (MEH-PPV) by ink-jet printing," *Advanced Functional Materials* **17**, 277 (2007).

[169] B. Dong, N. Lu, M. Zelsmann, N. Kehagias, H. Fuchs, C. M. S. Torres, and L. F. Chi, "Fabrication of high-density large-area conducting-polymer nanostructures," *Advanced Functional Materials* **16**, 1937 (2006).

[170] J. H. Lim and C. A. Mirkin, "Electrostatically driven dip-pen nanolithography of conducting polymers," *Advanced Materials* **14**, 1474 (2002).

[171] B. W. Maynor, S. F. Filocamo, M. W. Grinstaff, and J. Liu, "Direct-writing of polymer nanostructures: Poly(thiophene) nanowires on semiconducting and insulating surfaces," *Journal of the American Chemical Society* **124**, 522 (2002).

[172] D. J. Lipomi, R. C. Chiechi, M. D. Dickey, and G. M. Whitesides, "Fabrication of conjugated polymer nanowires by edge lithography," *Nano Letters* **8**, 2100 (2008).

[173] D. Wang, S. Kim, W. D. Underwood, A. J. Giordano, C. L. Henderson, Z. T. Dai, W. P. King, S. R. Marder, and E. Riedo, "Direct writing and characterization of poly(p-phenylene vinylene) nanostructures," *Applied Physics Letters* **95**, 233108 (2009).

[174] M. Granstrom, "Micro and nanoscale patterning of luminescent conjugated polymer films," *Synthetic Metals* **102**, 1042 (1999).

[175] M. Y. Han, B. Ozyilmaz, Y. B. Zhang, and P. Kim, "Energy band-gap engineering of graphene nanoribbons," *Physical Review Letters* **98**, 206805 (2007).

[176] M. Orlita, C. Faugeras, P. Plochocka, P. Neugebauer, G. Martinez, D. K. Maude, A. L. Barra, M. Sprinkle, C. Berger, W. A. de Heer, and M. Potemski, "Approaching the Dirac point in high-mobility multilayer epitaxial graphene," *Physical Review Letters* **101**, 267601 (2008).

[177] X. Du, I. Skachko, A. Barker, and E. Y. Andrei, "Approaching ballistic transport in suspended graphene," *Nature Nanotechnology* **3**, 491 (2008).

[178] C. Berger, Z. M. Song, T. B. Li, X. B. Li, A. Y. Ogbazghi, R. Feng, Z. T. Dai, A. N. Marchenkov, E. H. Conrad, P. N. First, and W. A. de Heer, "Ultrathin epitaxial graphite: 2D electron gas properties and a route toward graphene-based nanoelectronics," *Journal of Physical Chemistry B* **108**, 19912 (2004).

[179] K. S. Novoselov, A. K. Geim, S. V. Morozov, D. Jiang, Y. Zhang, S. V. Dubonos, I. V. Grigorieva, and A. A. Firsov, "Electric field effect in atomically thin carbon films," *Science* **306**, 666 (2004).

[180] X. L. Li, X. R. Wang, L. Zhang, S. W. Lee, and H. J. Dai, “Chemically derived, ultrasmooth graphene nanoribbon semiconductors,” *Science* **319**, 1229 (2008).

[181] K. Nakada, M. Fujita, G. Dresselhaus, and M. S. Dresselhaus, “Edge state in graphene ribbons: Nanometer size effect and edge shape dependence,” *Physical Review B* **54**, 17954 (1996).

[182] J. Kedzierski, P. L. Hsu, P. Healey, P. W. Wyatt, C. L. Keast, M. Sprinkle, C. Berger, and W. A. de Heer, “Epitaxial graphene transistors on SIC substrates,” *IEEE Transactions on Electron Devices* **55**, 2078 (2008).

[183] J. S. Moon, D. Curtis, M. Hu, D. Wong, C. McGuire, P. M. Campbell, G. Jernigan, J. L. Tedesco, B. VanMil, R. Myers-Ward, J. Eddy, C., and D. K. Gaskill, “Epitaxial-graphene RF field-effect transistors on Si-face 6H-SiC substrates,” *IEEE Electron Device Letters* **30**, 650 (2009).

[184] L. A. Ponomarenko, F. Schedin, M. I. Katsnelson, R. Yang, E. W. Hill, K. S. Novoselov, and A. K. Geim, “Chaotic dirac billiard in graphene quantum dots,” *Science* **320**, 356 (2008).

[185] D. Li and R. B. Kaner, “Materials science - Graphene-based materials,” *Science* **320**, 1170 (2008).

[186] L. S. Weng, L. Y. Zhang, Y. P. Chen, and L. P. Rokhinson, “Atomic force microscope local oxidation nanolithography of graphene,” *Applied Physics Letters* **93**, 093107 (2008).

[187] L. Y. Jiao, L. Zhang, X. R. Wang, G. Diankov, and H. J. Dai, “Narrow graphene nanoribbons from carbon nanotubes,” *Nature* **458**, 877 (2009).

[188] D. A. Dikin, S. Stankovich, E. J. Zimney, R. D. Piner, G. H. B. Dommett, G. Evmenenko, S. T. Nguyen, and R. S. Ruoff, “Preparation and characterization of graphene oxide paper,” *Nature* **448**, 457 (2007).

[189] G. Eda, G. Fanchini, and M. Chhowalla, “Large-area ultrathin films of reduced graphene oxide as a transparent and flexible electronic material,” *Nature Nanotechnology* **3**, 270 (2008).

[190] J. T. Robinson, F. K. Perkins, E. S. Snow, Z. Q. Wei, and P. E. Sheehan, “Reduced graphene oxide molecular sensors,” *Nano Letters* **8**, 3137 (2008).

[191] J. T. Robinson, M. Zalalutdinov, J. W. Baldwin, E. S. Snow, Z. Q. Wei, P. Sheehan, and B. H. Houston, “Wafer-scale reduced graphene oxide films for nanomechanical devices,” *Nano Letters* **8**, 3441 (2008).

[192] G. Eda, C. Mattevi, H. Yamaguchi, H. Kim, and M. Chhowalla, “Insulator to semimetal transition in graphene oxide,” *Journal of Physical Chemistry C* **113**, 15768 (2009).

[193] Z. Wei, D. Wang, S. Kim, S.-Y. Kim, Y. Hu, M. K. Yakes, A. R. Laracuente, Z. T. Dai, S. R. Marder, C. Berger, W. P. King, W. A. deHeer, P. E. Sheehan, and E. Riedo, "Nanoscale tunable reduction of graphene oxide for graphene electronics," *Science* , accepted (2010).

[194] C. Mattevi, G. Eda, S. Agnoli, S. Miller, K. A. Mkhoyan, O. Celik, D. Mostrogiovanni, G. Granozzi, E. Garfunkel, and M. Chhowalla, "Evolution of electrical, chemical, and structural properties of transparent and conducting chemically derived graphene thin films," *Advanced Functional Materials* **19**, 2577 (2009).

[195] C. Gomez-Navarro, R. T. Weitz, A. M. Bittner, M. Scolari, A. Mews, M. Burghard, and K. Kern, "Electronic transport properties of individual chemically reduced graphene oxide sheets," *Nano Letters* **7**, 3499 (2007).

[196] J. E. McKendry, C. S. Allen, K. Critchley, M. L. Gorzny, A. S. Walton, and S. D. Evans, "Magnetic field enhanced nano-tip fabrication for four-probe STM studies," *Nanotechnology* **19**, 085201 (2008).

[197] T. Kanagawa, R. Hobara, I. Matsuda, T. Tanikawa, A. Natori, and S. Hasegawa, "Anisotropy in conductance of a quasi-one-dimensional metallic surface state measured by a square micro-four-point probe method," *Physical Review Letters* **91**, 036805 (2003).

[198] L. J. van der Pauw, "A method of measuring specific resistivity and Hall effect of discs of arbitrary shape," *Philips Research Reports* **13**, 1 (1958).

[199] O. Akbulut, J. M. Jung, R. D. Bennett, Y. Hu, H. T. Jung, R. E. Cohen, A. M. Mayes, and F. Stellacci, "Application of supramolecular nanostarnping to the replication of DNA nanoarrays," *Nano Letters* **7**, 3493 (2007).

[200] V. Garcia, S. Fusil, K. Bouzehouane, S. Enouz-Vedrenne, N. D. Mathur, A. Barthelemy, and M. Bibes, "Giant tunnel electroresistance for non-destructive readout of ferroelectric states," *Nature* **460**, 81 (2009).

# VITA

Debin Wang was born in Beijing, China in 1981. He earned his B.S. degree in Physics and B.S. degree in Economics from Peking University in 2003. He moved to Atlanta for his graduate study at Georgia Institute of Technology, School of Physics in 2005. He then joined Prof. Elisa Riedo's group and started his thesis research on the development of thermochemical nanolithography nanofabrication of functional nanostructures, and research on atomic force microscopy characterization techniques. During the period of his graduate research, he received several fellowship and scholarship awards, including Georgia Tech Center for Organic Photonics and Electronics Graduate Student Fellowship in 2009, Georgia Tech Amelio Fellowship for Excellence in Graduate Research in 2010, and Chinese Government Scholarship for Outstanding Self-Financed Students Abroad in 2010.

# LIST OF PUBLICATIONS

This thesis is partly based on the following publications:

1. Z. Wei$^\dagger$, D. Wang$^\dagger$, S. Kim, S.-Y. Kim, Y. Hu, M. K. Yakes, A. R. Laracuente, Z. Dai, S. R. Marder, C. Berger, W. P. King, W. A. de Heer, P. E. Sheehan, E. Riedo, *"Nanoscale Tunable Reduction of Graphene Oxide for Graphene Electronics"*, Science **328**, 1373 (2010). ($^\dagger$Shared first authorship.)

2. D. Wang, S. Kim, W. D. Underwood, W. P. King, C. L. Henderson, S. R. Marder, E. Riedo, *"Direct Writing and Characterization of Poly(p-phenylene vinylene) Nanostructures"*, Appl. Phys. Lett. **95**, 233108 (2009).

3. D. Wang, V. Kodali, W. D. Underwood, J. Jarvholm, T. Okada, S. C. Jones, M. Rumi, Z. Dai, W. P. King, S. R. Marder, J. E. Curtis, E. Riedo, *"Thermochemical Nanolithography of Multifunctional Nanotemplates for Assembling Nano-Object"*, Adv. Funct. Mater. **19**, 3696 (2009). (Selected as journal cover.)

4. D. Wang, T. Okada, R. Szoszkiewicz, S. C. Jones, M. Lucas, J. Lee, W. P. King, S. R. Marder and E. Riedo, *"Local Wettability Modification by Thermochemical Nanolithography with Write-Read-Overwrite Capability"*, Appl. Phys. Lett. **91**, 243104 (2007). (Selected by Virtual Journal of Nanoscale Science & Technology **16**, 26 (2007).)